University of Puerto Rico
Río Piedras Campus
College of Natural Sciences
Department of Chemistry

Elucidation of the Composition of Photosystem I Light-Harvesting Complex I from the Green Microalga *Botryococcus braunii* and its Cytotoxic Evaluation in Breast Cancer Cells

By
Freisa M. Joaquín-Ovalle

April 28th 2022

Accepted by the Faculty of the Doctoral Program in Chemistry of the University of Puerto Rico in partial fulfillment of the requirements for the degree of

Doctor of Philosophy

_____

Dr. Kai H. Griebenow
Professor of the Department of Chemistry
Thesis Advisor

_____

Dr. Liz M. Díaz-Vázquez
Professor and Chairman of the Department of Chemistry
Thesis Committee Member

_____

Dr. Néstor M. Carballeira
Professor and Dean of the College of Natural Sciences
Thesis Committee Member

_____

Dr. Jorge L. Colón
Professor of the Department of Chemistry
Thesis Committee Member

_____

Dr. Arthur D. Tinoco
Associate Professor and Coordinator of the Department of Chemistry
Thesis Committee Member

Dedication

I dedicate this dissertation to the memory of my grandmother Virginia, who always believed in me and prayed for me. To my loving parents and sweetheart for their unconditional love and continuous support. And lastly, to my exceptional mentors, students, family, and friends for their hard work, words of advice, and encouragement.

Table of Contents

Chapter 2 – Materials and Methods

Chapter 3 – Purification and Characterization of Photosystem I Light-Harvesting Complex I (PSI-LHCI) from the Green Microalga Botryococcus braunii

Chapter 4 – *Botryococcus braunii* Photosystem I Light-Harvesting Complex I (PSI-LHCI) induces ROS-dependent decrease in cell viability by necrosis and autophagy pathways

List of Figures

List of Tables

List of Abbreviations

·OH	hydroxyl radical
$^1O_2$	singlet oxygen
2D	two-dimensional
AA	arachidonic acid
AA	ascorbic acid
ADP	adenosine diphosphate
ANOVA	two-way analysis of variance
APS	ammonium persulfate
APX	ascorbate peroxidase
ATG	autophagy-related genes
ATP	adenosine triphosphate
atp1	ATP synthase subunit alpha
atpA	ATP synthase subunit alpha, chloroplastic
atpB	ATP synthase subunit beta, chloroplastic
B. braunii	*Botryococcus braunii*
BECN1	Beclin 1 gene
BN	blue native
BSA	bovine serum
CAT	catalase
CD	circular dichroism
CDDP	cisplatin
Ce6	Chlorin e6
Chl	chlorophyll
CLSM	confocal laser scanning microscopy
CO_2	carbon dioxide
Cu^+	copper ion
Cyt b_6f	cytochrome b_6f complex
Cyt c	cytochrome c
DAPI	4’,6-diamidino-2-phenylindole
DCMU/Diuron	3-(3,4-Dichlorophenyl)-1,1-dimethylurea
DDM	*n*-dodecyl-β-D-maltoside
DHA	docosahexaenoic acid
DMA	N,N-dimethylacrylamide
DMEM	Dulbecco’s Modified Eagle’s Medium
DMF	N,N-Dimethylformamide
DMSO	dimethyl sulfoxide
DNA	deoxyribonucleic acid

DOE	U.S. Department of Energy
DPA	docosapentaenoic acid
$\Delta\pi H$	proton gradient
DTT	dithiothreitol
$\Delta\Psi$	electrical potential
$\Delta\Psi M$	mitochondrial membrane potential
EDTA	ethylenediaminetetraacetic acid
E_m	redox potential
EPA	eicosapentaenoic acid
ER	estrogen receptor
ETC	electron transport chain
FAME	fatty acid methyl esters
FBS	fetal bovine serum
Fd	ferredoxin
FDA	U.S. Food and Drug Administration
Fe^{2+}	non-heme iron
FeS	iron-sulfur centers
F_M	maximum fluorescence intensity
FM 4-64	*N*-(3-Triethylammoniumpropyl)-4-(6-(4-(Diethylamino) Phenyl) Hexa-trienyl) Pyridinium Dibromide
FNR	ferredoxin NADP reductase
F_O	initial value of the fluorescence
FPLC	fast protein liquid chromatography
G	spherical globules
GPM	green plasma membrane
GPX	glutathione peroxidase
GSH	reduced glutathione
h	hours
H^+	proton
H_2O_2	hydrogen peroxide
HBSS	Hanks' balanced salt solution
HCO_3^-	bicarbonate ion
HEPES	4-(2-Hydroxyethyl)piperazine-1-ethanesulfonic acid
HER2	human epidermal growth factor receptor 2
HOCl	hypochlorous acid
IC_{50}	half maximal inhibitory concentration
IHC	immunohistochemistry
J,I	intermediate inflection points
K	Potassium

L-15	Leibovitz's Medium with L-Glutamine
LAMP-2A	lysosomal-associated membrane protein 2A
LC3	microtubule-associated light chain 3
LED	light-emitting diode
LHC	light-harvesting complex
MEM	Minimum Essential Medium
min	min
Mn_4O_5Ca	manganese-oxygen-calcium cluster
MTS	(3-(4,5-dimethylthiazol-2-yl)-5-(3-carboxymethoxyphenyl)-2-(4-sulfophenyl)-2H-tetrazolium)
MW	molecular weight
N/N_2	Nitrogen
NADPH	reduced nicotinamide adenine dinucleotide phosphate
NaOH	sodium hydroxide
$NO^{\cdot}$	nitric oxide
NPQ	non-photochemical quenching
O	origin
O_2	oxygen
$O_2^{\bullet-}$	superoxide anion
OEC	oxygen-evolving complex
OJIP	chlorophyll fluorescence induction
$ONOO^-$	peroxynitrite
P	Phosphorus
P	peak
PAR	photosynthetically active radiation
PBS	phosphate buffered saline
PC	plastocyanin
PD-L1	programmed cell death ligand 1
Pen/Strep	penicillin/streptomycin
PES	phenazine ethosulfate
petA	cytochrome f
Phe_{D1}	primary electron acceptor D1-pheophytin molecule
P_i	inorganic phosphate
PI	propidium iodide
pmf	proton motive force
PMSF	phenylmethylsulfonyl fluoride
PQ	plastoquinone
PQH_2	plastoquinol
PR	progesterone receptor

psaA	photosystem I P700 chlorophyll a apoprotein A1
psaB	photosystem I P700 chlorophyll a apoprotein A2
psaC	photosystem I iron-sulfur center subunit VII
PsbA	D1 protein
PsbB	CP47 protein
PsbC	CP43 protein
PsbD	D2 protein
PSI	photosystem I
PSI-LHCI	photosystem I light-harvesting complex I
PSII	photosystem II
PTM	post-translational modifications
PUFAs	polyunsaturated fatty acids
Q_A	one-electron acceptor quinone
Q_B	two-electron acceptor quinone
q_E	energy-dependent
q_I	photoinhibition
q_T	state transitions
RC	reaction centers
Rf	migration distance of the dye front
RNO	*p*-nitrosodimethylaniline
RO·	alkoxyl
ROO·	peroxyl
ROS	reactive oxygen species
RT	room temperature
SC	supercomplexes
SDS-PAGE	sodium dodecyl sulphate-polyacrylamide gel electrophoresis
SEM	scanning electron microscopy
SOD	superoxide dismutase
ST	stroma thylakoids
STM	stroma thylakoid membranes
TAG	triacylglycerol
TEMED	N,N,N',N'-Tetramethylethylenediamine
TMP	transmembrane particles
TNBC	triple-negative breast cancer
TP	thylakoid plexus
TRX	thioredoxins
UTEX	University of Texas at Austin
UV/Vis	ultraviolet-visible
Y_z	D1-Tyrosine161

Acknowledgments

There are many people whom I would like to thank for their contribution to this thesis. I would first like to thank my advisor, Dr. Kai Griebenow, for his patience and continuous support throughout this research. His guidance steered me in the right direction, built my self-confidence, and helped me develop a thicker skin; for this, I will be forever grateful. Besides my advisor, I would like to thank my committee members: Dr. Arthur Tinoco, Dr. Néstor Carballeira, Dr. Liz Díaz, and Dr. Jorge Colón, for their valuable feedback and encouragement but also as a constant source of inspiration.

I am grateful to the collaborators for contributing their knowledge and expertise, particularly to Dr. Yasuhiro Kashino, who allowed me to visit his lab at The University of Hyogo in Japan to obtain valuable data for my research. Special gratitude goes out to all the professors, Ph.D. colleagues, Covacha girls, and former and current laboratory members (Irivette, Josell, Louis, Vanessa, and Zally) for their assistance, training, and friendship. I will always cherish the memories and laughs shared with the Dra's girls, exciting conference trips, and sleepless nights while writing and working together. Dr. Yamixa Delgado, for her support, guidance, valuable comments, suggestions, and corrections, greatly benefitting the completion of this dissertation. Also, for providing a life-changing work placement opportunity. To Denisse, Dina, Sara, and Yermary, thank you for always saying the right thing at the right time. This journey would not have been the same without you.

I am also grateful to the financial support from the Alfred P. Sloan Foundation, PR NASA Space Grant, Research Center for Excellence in Renewable Energy, Research Initiative for Scientific Enhancement (RISE) with grant number 5R25GM061151-17, and SMDP for providing the funding for this work and aid in time of need.

I wish to thank my excellent undergraduate students Sofía, Xiomara, Grace, Katerina, Andraous, and Nicole, for the assistance provided during this research. And finally, to all my friends, sweetheart, and family, particularly my parents, for their moral and emotional support throughout this journey and my life in general. Thank you all for your encouragement, kindness, and friendship.

Abstract

Natural products have contributed to the development of protein formulations currently used as biotherapeutic agents. The topic of this thesis investigates the green microalga *Botryococcus braunii* (*B. braunii*) Photosystem I light-harvesting antenna complex I (PSI-LHCI) and its delivery to one of the most aggressive types of breast cancer with fewer treatment options, triple-negative breast cancer cells (TNBC), exhibiting notable anticancer activity. The PSI-LHCI multiprotein supercomplex plays a significant role in the highly efficient photosynthetic conversion of light energy to chemical energy while generating reactive oxygen species (ROS). Intracellular ROS-regulating anticancer therapeutic strategies emphasize ROS's ability to trigger programmed cell death by selectively killing cancer cells after inducing oxidative stress and exceeding cytotoxic thresholds. In Chapter 3, PSI-LHCI isolation, purification and characterization will be introduced, followed by Chapter 4, an investigation of the role and cell death mechanism determined after the delivery of *B. braunii* PSI-LHCI to TNBC MDA-MB-231 cells. A discontinuous sucrose density gradient by ultracentrifugation produced PSI-LHCI complex, and *in vitro* experiments were conducted by incubating MDA-MB-231 cells under serum starvation conditions with PSI-LHCI. In the absence of an LED light source, we conclude that *B. braunii* PSI-LHCI naturally generates intracellular ROS, significantly reducing cell viability compared to typical positive controls while inducing necrosis by autophagy cell death mechanism.

Introduction

1.1 Algal Products: Current Research and Biomedical Applications

From the dawn of history to the present day, algae has been regarded as an essential contributor to life, producing most of the oxygen we breathe [1,2]. Their capability of generating novel products for the food, agriculture, cosmetics, pharmaceutical, materials, and the biofuel industry makes them capable of transforming the world [2]. As of August 3, 2021, the U.S. Department of Energy (DOE) appointed approximately $34 million in funding for bioenergy technologies research and development [3].

The definition of algae encompasses a large and varied group of photosynthetic eukaryotic aquatic organisms whose diversity is embodied by three representative groups: Rhodophyta (red algae), Phaeophyta (brown algae), and Chlorophyta (green algae), ranging from large-sized and multicellular macroalgae to microscopic and single-celled microalgae [4]. In recent decades, algal culturing and biotechnological applications have gained widespread awareness owed to the generation of market-value algal-based products. Microalgal species' chemical composition comprises lipids, proteins, carbohydrates, and other compounds such as pigments, and vitamins, regarded as high-value bioactive compounds [5].

Under adequate conditions, microalgae double their biomass in 24 hours with 3.5 hours log phase, and this biomass as a source of energy is an excellent alternative to fossil fuels [6]. Considering microalgae high storage of lipids, from Table 1.1, it can be seen that their product yield rate in the form of oils, reduced requirement of land use, and increased biodiesel productivity results in microalgae

Table 1.1 Comparison of microalgae (low, medium, and high oil content) with other energy crops [7].

Crop	***Oil Content (% Dry Weight)***	***Oil Yield (L/ha Year)***	***Land Use (m^2 Year/kg Biodiesel)***	***Biodiesel Productivity (kg Biodiesel/ha Year)***
Corn	44	172	66	152
Hemp	33	363	31	321
Soybean	18	636	18	562
Jatropha	28	741	15	656
Camelina	42	915	12	809
Canola	41	974	12	862
Sunflower	40	1070	11	946
Castor	48	1307	9	1156
Palm oil	36	5366	2	4747
Microalgae[a]	30	58,700	0.2	51,927
Microalgae[b]	50	97,800	0.1	86,515
Microalgae[c]	70	136,900	0.1	121,104

[a] Low oil content. [b] Medium oil content. [c] High oil content.

owning to a superior per unit of surface values than any other variety of energy crops [2,7]. The optimization of the culture conditions and control of the parameters regulating growth, such as light intensity, temperature, inorganic carbon in the form of bicarbonate salts or enriched air, macronutrients like nitrogen (N), phosphorus (P), and potassium (K), and culture mixing deliver the maximum photosynthesis rate, thus increasing the lipid content of dried microalgal biomass up to 80% [5,8].

At first, biodiesel production was the main application of microalgal lipids, whose fraction is predominantly composed of nonpolar lipids, including free fatty acids (saturated, unsaturated, and polyunsaturated), carotenoids (e.g., β-carotene), and acylglycerols (mono-, di-, triacylglycerol or TAG). The latter, accumulated in oil bodies, is easily convertible to biodiesel through its transesterification with methanol to fatty acid methyl esters (FAME) [9]. Polar lipids such as glycerophospholipids and galactolipids, with long carbon chains and high degrees of unsaturation, are thereby not convertible to biodiesel through conventional methods and very challenging to process [10,11]. Membrane lipids are known to produce up to 40% polyunsaturated fatty acids or PUFAs (e.g., eicosapentaenoic acid [EPA], arachidonic acid [AA], docosapentaenoic acid [DPA], and docosahexaenoic acid [DHA]), regarded as commercial-scale high-value products used in the food, pharmaceutical, and cosmetic industry, in particular, the omega-3 and omega-6 fatty acids which act as potent antioxidants with promising therapeutic effects towards inflammatory diseases [2,8,12].

Microalgal proteins perform a structural function as an intrinsic component of lipidic membranes and light-harvesting complexes and a metabolic role as

enzymes involved in photosynthesis [13]. Numerous microalgal species produce high amounts of proteins with great nutritional value, similar to traditional animal and vegetable sources, e.g., meat, egg, milk, soy [11]. Microalgae also produce high quantities of essential amino acids mammals cannot synthesize, used in the food industry as nutritional supplements for human consumption, e.g., *Chlorella* pills and *Spirulina* flakes [4,14].

Carbohydrates from microalgae featuring mono-, oligo-, and polysaccharides render metabolic and structural roles and can be found covalently attached to proteins (glycoproteins) and lipids (glycolipids) [11]. Microalgal cells are comprised of carbohydrates such as glycogen, starch, agar, cellulose, and hemicellulose, which can be used as hygroscopic substances, antioxidants, and renewable feedstock [5,11]. Carbohydrates from various microalgal species, for instance, *Anabaena*, *Chlamydomonas*, *Chlorella*, *Porphyrydium*, *Scenedesmus*, *Spirogyra*, and *Spirulina*, are thus converted through high-temperature acid hydrolysis pretreatment, saccharification by glycosidic bonds breakage, and fermentation, to one of the most common types of biofuel, bioethanol [4,15].

Various microalgal species also produce marketable bioactive products such as chlorophyll (Chl), carotenoids, β-carotene, and xanthophylls like astaxanthin, phycobiliproteins, vitamins, and other antioxidants. Among the different types of photosynthetic pigments produced by microalgae, chlorophyll *a*, one specific form of chlorophyll, and its metabolites such as pheophorbide *b* and pheophytin b, have strong antioxidant properties, which by definition prevent oxidative damage to cells and tissues by scavenging free radicals [4,16]. As an

essential bioactive compound, chlorophyll is regularly used in the food industry as a natural coloring agent and in the pharmaceutical industry due to its antimutagenic activity in the form of the soluble derivative chlorophyllin [17]. Chlorophyll's similar chemical structure to hemoglobin is hypothesized to promote fast carbon dioxide (CO_2) and oxygen (O_2) interchange, contributing to the fundamental properties of wound healing by tissue growth stimulation while preventing bacteria advancement, thus used to treat ulcers and oral sepsis [16].

Carotenoids are recognized in the pharmaceutical and food industry for their antioxidant and anti-inflammatory properties, particularly the nutritional supplement and coloring agent β-carotene, obtained from *Dunaliella salina*. Astaxanthin, a xanthophyll derived under environmental stress conditions from *Haematococcus pluvialis*, has been incorporated into fish and crustaceans' diet to give them their characteristic pink hue, and perhaps its most crucial biomedical application, anti-inflammatory effects; more pronounced than that of the standard anti-inflammatory drug, prednisolone [5,11,18]. Free radical scavengers like the water-soluble proteins, phycobiliproteins, are used in fluorescence microscopy as labeling agents, known to suppress inflammation and ease disease-related symptoms due to their antioxidant activity [11,18].

Microalgal vitamins, for instance, pro-vitamin A (β-carotene), vitamin B12 (cobalamin), vitamin C (ascorbic acid), vitamin D, and vitamin E (tocopherol and tocotrienols), hold nutritional value owing to their potent antioxidant activity, antiproliferative, and anticarcinogenic properties [19]. Microalgae are rich in sterols, namely phytosterols, e.g., campesterol, sitosterol, and stigmasterol, which

are recommended for their cholesterol-reducing properties in several cardiovascular diseases, alongside their antioxidant, anti-inflammatory, and anticancer effects [4,19]. Phytochemicals from microalgae have numerous valuable medicinal components and properties that urge the scale-up of microalgal biomass production as a promising antioxidant, anti-cholesteroligenic, anti-inflammatory, antimutagenic, antiproliferative, and anticancer source.

1.2 Green Microalga of Interest: *Botryococcus braunii*

Due to the unsustainable use of fossil fuels' finite and nonrenewable resources, an increase in oil prices compels most microalgal biotechnological studies and cultivation techniques. They aim to enhance microalgal lipid production and optimize biofuel resources for energy, particularly biodiesel generation. The widespread application and increasing demand for microalgal-based bioproducts can contribute to meeting and solving most of the global sustainability needs. *Botryococcus braunii* (*B. braunii*) is an excellent model of a microorganism that can produce in the resting phase of growth up to 86% of its dry weight as hydrocarbon oils, potentially used as alternative renewable fuels (Table 1.2) [20–22]. Thus, this green photosynthetic microalga is highly studied due to its hydrocarbon accumulation, secretion, and synthesis ability [23].

Table 1.2 Oil content of several microalgal species [22].

Microalga	***Oil Content (% Dry Weight)***
B. braunii	25-75
Chlorella sp.	28-32
Crypthecodinium cohnii	20
Cylindrotheca sp.	16-37
Dunaliella primolecta	23
Isochrysis sp.	25-33
Monallanthus salina	>20
Nannochloris sp.	20-35
Nannochloropsis sp.	31-68
Neochloris oleoabundans	35-54
Nitzchia sp.	45-47
Phaeodactylum tricornutum	20-30
Schizochytrium sp.	50-77
Tetraselmis sueica	15-23

Although the hydrocarbon productivities of several *B. braunii* strains have already been assessed; the machinery that drives light energy conversion to chemical energy via photosynthesis, also known as the photosynthetic apparatus, remains unresolved. A study on *B. braunii* light-harvesting complexes (LHCs) concluded that the pigment composition is comparable to LHCII in plants; this is the only literature available on the subject [24]. This species remains underutilized other than the biofuel industry, overlooking their full research potential. Therefore, in this research, the focus was placed on obtaining multiprotein complexes from the biomass of *B. braunii*, the green microalga of interest, for their potential biomedical applications.

B. braunii is a photosynthetic unicellular microalga, a member of the Chlorophyceae class of freshwater green microalgae that produces a substantial amount of hydrocarbons as algal biomass, which can be potentially exploited for various commercial purposes [23,25]. This green colonial microalga is highly studied and examined due to its hydrocarbon content production, including tetracosane, octacosane, palmitic, and oleic acid. It is widely located in fresh and brackish or slightly salty water, reservoirs, and ponds at tropical, moderate, and arctic latitudes [26]. Aside from chlorophyll *a* and *b*, this microalga also contains lutein and β-carotene as its major carotenoids constituents, which are biological pigments naturally occurring inside chloroplasts that absorb and transfer light energy and provide photooxidative protection against reactive oxygen species [26,27].

B. braunii is classified into three different chemical races: A, B, and L, defined by the liquid hydrocarbons the microalgae synthesize [28]. Race A produces mainly a series of C_{23}-C_{33} odd-numbered *n*-alkadienes, mono-, tri-, tetra-, and pentaenes derived from fatty acids [29]. This race turns a pale yellow from a green colony color in the stationary growth phase and has a distinctive feature among other races, long-chain alkenyl phenols, whose function is essential for protecting against biochemical oxidative degradation [30]. Race B produces large quantities of the triterpene botryococcene of C_{30}-C_{37} with a C_nH_{2n-10} general formula and small amounts of C_{31}-C_{34} polymethylated squalenes [28,31]. The A and B races contain long aliphatic chains crosslinked by ether bridges as a distinguishable characteristic of the nature of the biopolymers present in the microalgal cell wall. Race L and B are of an orange-red or orange-brown colony color due to carotenoid accumulation in both races' stationary phase [30]. The L race yields a single C_{40} lycopadiene, a tetraterpene [32]. Out of all races, the hydrocarbons from *B. braunii* race A has the most chemical variability content, from 0.4% to 61.0% of their dry cell weight [28].

Under the microscope, *B. braunii* UTEX 2441 race A colonies, obtained from the culture collection of the University of Texas at Austin (UTEX), exhibit a botryoid-type morphology of individual pyriform-shaped cells bound by a lipid-containing matrix (Figure 1.1) [28].

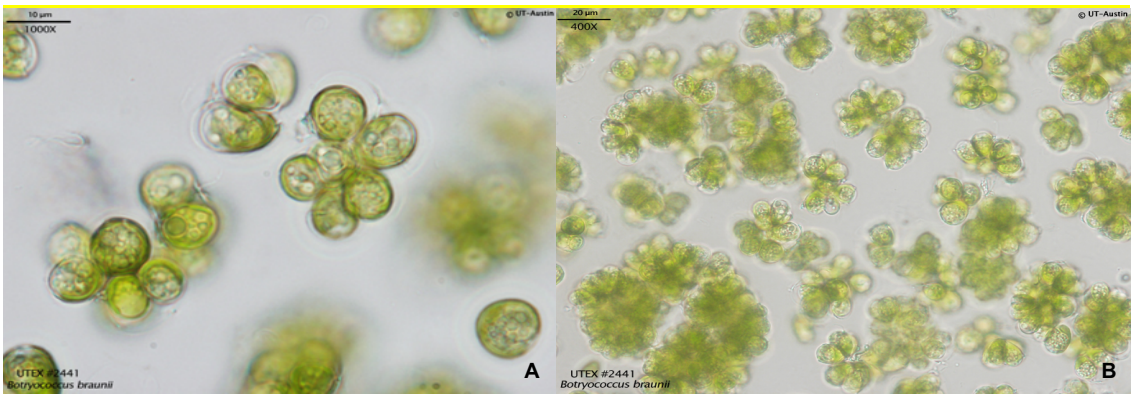

Figure 1.1 Microscopic examination of *B. braunii* UTEX 2441 cells by UTEX, licensed under CC by 4.0. Bars indicate 10 µm (A) and 20 µm (B) [33].

The microalgal cells' basal surface is enclosed by a matrix comprised of outer walls formed from successive cellular divisions, with the bulk of *B. braunii* hydrocarbons stored in these outer walls [28]. Lipid accumulation can be achieved via nitrogen deprivation, which serves as an excellent experimental tool for monitoring metabolic activities during lipid accumulation in microalgae [34]. Nitrogen deprivation is considered an environmental stress factor that causes microalgae a shift in lipid storage, which provides a significant number of neutral lipids, multibranched and, or polyunsaturated in nature [35]. A vast proportion of the total lipid content in *B. braunii* is composed of neutral lipids, with its highest production rate occurring in the stationary growth phase and the maximum yield arising when the microalga turns from color green to brown in the growth phase [36]. Recent studies suggest a different approach to nitrogen depletion, where excess CO_2 is supplied under intense continuous light, therefore, inducing lipid accumulation [37].

To perform photosynthesis with adequate biomass growth, microalgae need a good carbon source and light exposure since light intensity, and light spectrum are considered critical factors in the phototrophic growth of microalgae [36]. Excess light also holds a harmful purpose, damaging the microalgae's photosynthetic apparatus, thus inducing the organism to adopt photoprotective mechanisms such as fluorescence emission and heat dissipation [38]. In order to study *B. braunii* protein complexes, culture conditions parameters such as temperature, CO_2 supply, nutrients, light intensity, and culture mixing must be controlled. This project commenced a study that resolves the photosynthetic apparatus components of the phototrophic organism *B. braunii* towards generating high-value biomedical products.

1.3 Insight into the Importance and Role of Photosynthesis

The photosynthesis timeline started ~2.4 billion years ago by an endosymbiosis process of a primordial eukaryote engulfing the ancestor organism we know today as a cyanobacterium; subsequently, ancient cyanobacteria experienced a stage of accelerated evolution of anoxygenic photosystems to develop modern-day oxygenic photosynthesis [39–41]. The conversion of harnessed light energy to chemical energy to produce molecular O_2, and to synthesize reduced nicotinamide adenine dinucleotide phosphate (NADPH) and adenosine triphosphate (ATP), whose energy is used in the Calvin cycle to fix CO_2, is crucial to support nearly all forms of life on Earth [39]. In organisms such as plants, cyanobacteria, and green algae, oxygenic photosynthesis occurs in the thylakoid membranes and consists of two distinct and highly organized membrane-

bound photosynthetic reaction centers (RC), namely photosystem I (PSI) and photosystem II (PSII), each with its light-harvesting antenna protein-bound pigment complexes (LHCI and LHCII) associated with it, working in series in the Z-scheme [42–44]. The Z-scheme depicts the electron transport pathway of photosynthesis from water to oxidized $NADP^+$ on a redox potential (E_m) vertical energy scale from left to right, with the most reducing (negative E_m) components at the top and the most oxidizing (positive E_m) components at the bottom. Comparable with an uphill/downhill reaction, the diagram illustrates the distinctive redox potential in the ground versus the excited energy state of the particular pigments, P680/P680* in PSII and P700/P700* in PSI (Figure 1.2) [45].

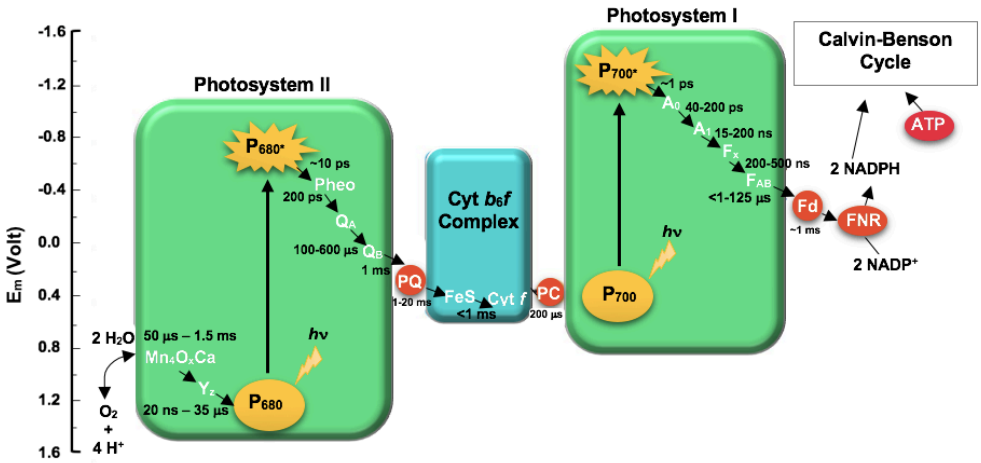

Figure 1.2 The electron transport representation of the oxygenic photosynthesis process and the Z-scheme. This diagram was modified from Govindjee et al [46].

In detail, the oxygenic photosynthesis process involves four major macromolecular membrane-associated complexes directly related to the

photosynthetic process: PSII and PSI, connected via the cytochrome b_6f (Cyt b_6f) complex and the enzyme ATP synthase. Photosynthesis initiates with the dual gathering of light energy as photon absorption by a large number of tightly coupled and integral proteins, LHCs, and other antenna pigment complexes associated with both photosystems that play a role in light capture by transferring excitation energy to the photosynthetic RC, dissipating excess energy as heat and emitted as fluorescence [47,48]. In the Z-scheme model of photosynthesis, charge separation occurs within the D1 protein of the PSII core complex, where the primary electron donor of PSII (P680) absorbs a photon, exciting an electron from a low energy state to a higher energy state (P680*) [49]. This electron, initially extracted from water molecules by the tetranuclear manganese-oxygen-calcium cluster (Mn_4O_5Ca) of the oxygen-evolving complex (OEC) through D1-Tyrosine161 (Y_z), is then transferred by the primary electron acceptor D1-pheophytin molecule (Phe_{D1}) to the first electron acceptor of PSII, Q_A, a one-electron acceptor quinone that is firmly bound to the D2 protein, and then to the two-electron acceptor quinone, Q_B, bound to the D1 protein [48]. A bicarbonate ion (HCO_3^-), the mobile ligand of the non-heme iron (Fe^{2+}) located in between Q_A and Q_B, proffer a role in photosynthesis and particularly PSII activity by stimulating water splitting with the acceptance of protons produced by the water-splitting process, responsible for the protonation of reduced Q_B that becomes plastoquinol (PQH_2). Under stress conditions, HCO_3^- concentration directly affects PSII O_2 activity and perturbs electron transfer through the electron acceptors quinone Q_A and Q_B whose Fe structure stabilization and Mn_4O_5Ca cluster mediates [50,51].

Subsequently, a chain of mobile electron carrier molecules through the thylakoid membrane, namely a plastoquinone (PQ) pool, exchanges with PQH_2. The reduction of PQ to PQH_2 reduces Cyt b_6f by translocating and pumping protons via the Q-cycle, thus connecting PSII to Cyt b_6f, prompting the interaction of Cyt b_6f with PSI through the copper-containing protein, plastocyanin (PC). In PSI, P700, a special Chl *a* pair is the primary electron donor, whereas P700* is the excited electronic state of P700. The primary electron acceptor of PSI is A_0, a special Chl *a* molecule; other molecules on the acceptor side include A_1 (vitamin K1); F_x, F_A, and F_B, three iron-sulfur centers (FeS), and a mobile water-soluble ferredoxin (Fd) that upon reduction transfers an electron to either $NADP^+$ which is reduced to NADPH through ferredoxin NADP reductase (FNR), Cyt b_6f, or alternative electron acceptors such as O_2 [48,49]. The ATP produced from adenosine diphosphate (ADP) and inorganic phosphate (P_i) catalyzed by ATP synthase employs the proton motive force (pmf), built-up electrical potential ($\Delta\Psi$), and proton gradient (ΔpH) across the thylakoid membrane by the proton flow originated from water splitting at the OEC, cyclic reduction-oxidation of PQ/PQH_2, Cyt b_6f complex Q-cycle, and PSI cyclic electron transport [48]. The NADPH and ATP obtained are used in the Calvin-Benson cycle to fix atmospheric CO_2 and produce carbohydrates [52]. Hence, the overall photosynthesis equation is written as:

$$2H_2O + CO_2 \rightarrow [CH_2O] + O_2 + H_2O \qquad (1)$$

The photosynthesis process is controlled by various mechanisms that either alter light-harvesting efficiency or stabilize the absorption of PSI and PSII, involving

varied light intensities and spectral properties—predominantly by non-photochemical quenching (NPQ) mechanisms affecting the rate constant of excitation of PSI and particularly PSII, thus decreasing the fluorescence yield [39]. Changes in quenching correlate to (1) photoinhibition, q_I, or photoinactivation leading to oxidative damage and loss of PSII RC; (2) state transitions, q_T, significant in algae at low light levels due to a change in antenna pigment size and the reversible movement of LHCII between PSII and PSI RC; and (3) energy-dependent, q_E, associated with light-induced H^+ transport into the thylakoid lumen resulting in the development of low pH from electron transport, hence regulating the rate of excitation of PSII RC [53,54].

In oxygen-evolving photosynthesis, the photons in the photosynthetically active radiation (PAR) most efficiently used are in the wavelength range of 400-700 nm. In nature, PSI is considered the most efficient light-capturing and energy conversion photosynthetic apparatus [55]. Algal engineering strategies such as antenna pigment size optimization attenuates NPQ losses, allowing more extensive light transmission into lower layers of cultured cells in bioreactors, maximizing photosynthetic efficiency [38,56]. Nevertheless, excess light damages the photosynthetic apparatus, and algae have evolved photoprotective mechanisms to offset this drawback [38]. Fluorescence studies, particularly Chl *a* fluorescence transients following the regular chlorophyll fluorescence induction (OJIP) pattern, provide insight into photochemical efficiency and the photosynthetic organisms' ability to tolerate environmental inhibitors and stressors, plus to which extent such stress has damaged the photosynthetic apparatus [57].

The polyphasic Chl *a* fluorescence induction curves or fluorescence transients arise from dark-adapted photosynthetic samples after illumination, which include a fast phase affected by the functional and structural changes in the photosynthetic apparatus that occurs under 1 s and is labeled OJIP, where O stands for origin or minimum (F_O) and initial value of the fluorescence, J and I are intermediate inflection points, and where P is peak or F_M corresponding to maximum fluorescence intensity [48].

1.4 The Photosynthetic Apparatus: Photosystems and Light Harvesting Complexes

The eukaryotic oxygenic photosynthesis process occurs in the endosymbiotic cell organelles, the chloroplasts, comprised of characteristic photosynthetic pigments with organized thylakoid membranes ultrastructure [58,59]. Highly compartmentalized, the chloroplast encompasses outer and inner envelope membrane, inter-envelope membrane, cylindrical closely stacked discs named grana, interconnecting unstacked stroma lamellae, thylakoid lumen, and intergranal thylakoids [60,61]. The photosynthetic apparatus flexible molecular machinery is highly susceptible yet can acclimate to environmental factors. It contains iron, copper, manganese, and iron-sulfur center cofactors, which perform the light-dependent reactions in the three main multi-protein-pigment membrane complexes: PSI, PSII, each with its reaction center supercomplex and LHCs, and Cyt b_6f [47,53,58,62,63]. The thylakoid membranes are arranged analogous to land plants, containing the photosynthetic electron transport chain's (ETC) primary complexes: PSII and LHCII located in the appressed grana enriched regions forming super- and mega complexes, Cyt b_6f proportionately allocated amidst

grana and stromal regions, and PSI and its corresponding LHCI found in the stroma lamellae and grana end membranes [60,61,63].

Multi-protein-pigment complexes recovery strategies require a higher degree of purity concerning the sample's complexity. The general microalgal biomass processing requires harvesting by coagulation/flocculation to concentrate the biomass, thickening, and dewatering by flotation, filtration, and centrifugation, followed by convective drying to obtain a concentrated thick microalgal slurry. Microalgal cells undergo mechanical (e.g., homogenizer, bead-mill, ultrasonication) or non-mechanical (physical, chemical, enzymatic) cell wall disruption methods. Soluble proteins are isolated from cell debris at low temperatures and typically at high-speed centrifugation conditions, protein fractionation by dispersibility, density, or size, using sucrose gradient centrifugation, and protein purification by chromatographic methods [64].

The highly conserved PSII pigment-protein supramolecular complex, a light-driven-plastoquinone-oxidoreductase homodimer, is organized in a core complex and a light-harvesting antenna system. The PSII RC comprises four Chl *a* molecules, two pheophytins *a,* $Pheo_{D1}$ and $Pheo_{D2}$, two PQ, Q_A and Q_B bounded by non-heme iron, two redox-active tyrosine, Y_Z and Y_D, and OEC [65]. The core complex contains two essential subunits, D1 (PsbA), whose a major target of photodamage, and D2 (PsbD), including P680 RC and all ETC cofactors, the inner antenna and Chl *a* coordinating CP47 (PsbB) and CP43 (PsbC) proteins, and various low molecular subunits [65–67]. PSII with a total molecular weight of 350 kDa as a monomer, 700 kDa as a homodimer, and 1,100 kDa as a supercomplex

comprises independent monomers, each with 17 transmembrane subunits, three peripheral membrane subunits, multiple cofactors, for a total of approximately 40 permanently attached or temporarily associated proteins [65,68–70].

In eukaryotic green algae, PSI, whose role is to catalyze light-driven electron transport from PC to Fd, is isolated as a monomer or a supercomplex of a monomer with a molecular mass between 230-600 kDa; as a trimer in the native membrane, it exists with a mass of 1068 kDa for the entire complex [52,55]. As a monomer, PSI is highly conserved among plants and green algae and presents an absorption maximum of around 680 nm. It contains an apparent 65 kDa PsaA/PsaB heterodimer core complex coordinating about 100 Chls and 20 β-carotene light-capturing molecules, 14 subunits (PsaA-PsaL and PsaN-PsaO), and up to 9 LHCI outer antenna proteins and small core subunits from 10-20 kDa, which guarantee photoprotection [55,63,71]. The characterization of PSI RC from plant chloroplasts was first published in 1975, following a purification protocol comprising an initial detergent treatment, sucrose density gradient centrifugation, and an absorption spectrum characterization [72]. Subsequently, several higher plants and algae PSI and LHCI purification research articles revealed their general red-shift characteristics (Stokes' shift) of 2-5 nm and 77K emission bands at 680 nm and 730 nm [73,74].

Within green algae, PSI/PSII ratio generally remains at a level of 1:1, whereas in cyanobacteria, elevated ratios of 2:1 and 5:1 are observed [75]. In land plants and green algae, Chl *a* is located in the core complex of PSI and PSII, and Chl *b* is almost exclusively found in the pigment antenna system of LHCs [76].

These particular types of chlorophyll exist side-by-side at Chl *a*/*b* ratio of 3:1, with variations in ratio used as an indicator of stress or photosynthetic apparatus damage, expressed as controlled changes in antenna complex size [77,78]. The LHC proteins involving the two photosystems perform different roles, such as excessive light energy dissipation and optimizing light energy utilization, with core, peripheral, and accessory antennas [45]. The six highly homologous major LHCII proteins associated with PSII are encoded by the heterogeneous trimer *Lhcb1-3*, whereas the monomeric and tightly associated minor LHC proteins consist of CP29 (*Lhcb4*), CP26(*Lhcb5*), and CP24(*Lhcb6*) [79]. Moreover, PSI is associated with LHCs dimers with a higher Chl a/b ratio [24].

Both photosystems have been characterized in several organisms and have been found to dissociate into various high molecular mass complexes, with sub-complexes appearing loosely associated with the core, providing valuable information regarding their composition. The two photosystems' supramolecular organization and associated light-harvesting antennas entail a PSII dimer and two LHCII trimers to form the $C_2S_2M_2$ and C_2S_2 supercomplexes [63,80]. The interaction between monomeric PSI and LHCI in green algae suggests a more extensive antenna size comprising a 22-30 kDa Chl a, b, and carotenoid binding apoprotein, divergent from land plants and equivalent with Lhca1-4 genes encoding the LHCI of PSI [24,55,79].

An upsurge in light intensity leads to an increase in energy absorption by the photosynthetic apparatus; consequently, the toxic byproducts of aerobic metabolism, reactive oxygen species (ROS), are generated [62]. Photosystems in

eukaryotic photosynthetic organisms have developed an array of photoprotective mechanisms to counteract the harmful effects of oxidative stress and excessive light energy. Photodamage against PSII due to the strong oxidizing reaction of water splitting and the photoprotective mechanisms to repair and recover has been extensively considered, e.g., NPQ, photoinhibition of PSII as means of ETC and PSI photoprotection. In contrast, PSI appears to be effectively protected from the irreversibility of damage by repair strategies and LHCI [81]. Typically, the thylakoid membrane contains a ROS-producing enzyme named plastid terminal oxidase, and the strong reductant function of PSI under stress conditions reduces all $NADP^+$ and transfers electrons to O_2 to naturally generate ROS [81].

1.5 Reactive Oxygen Species Production in Algae

Reactive oxygen species are considered highly reactive and cytotoxic, leading at high concentrations to irreversible oxidative damage to proteins, deoxyribonucleic acid (DNA), lipid membranes, and to both photosystems, PSI and PSII [82]. Emerging as undesirable byproducts of aerobic metabolic processes such as respiration and photosynthesis, ROS determining roles are shaped by production and scavenging mechanisms to maintain a delicate balance (homeostasis), though dissipating under stress conditions [82,83]. Extreme temperature, change in salinity, high irradiance, nutrient deprivation, pH variation, and oxidative stress are examples of abiotic stress conditions that induce ROS's excessive production in algae [84].

The prooxidants or oxygen-containing main species of ROS primarily comprise free radicals such as superoxide anion ($O_2^{\bullet-}$), the hydroxyl radical (·OH),

peroxyl (ROO·), alkoxyl (RO·), and nitric oxide (NO·). In contrast, the non-radicals involve hydrogen peroxide (H_2O_2), singlet oxygen ($^1O_2$), and hypochlorous acid (HOCl) [11].

The most common ROS produced are ·OH formed on PSII electron donor and acceptor sides, also $^1O_2$, mainly occurring at PSII, but also present in PSI as it has been related to photoinhibition, and H_2O_2 and $O_2^{\bullet-}$, predominantly appearing on PSI's acceptor side, mentioned in order of chemical activity [53,85–87]. Initially believed to be the only generator of ROS, PSI is the main generation site of ROS, owing to the culmination of electron transfer reactions in the stromal thylakoid membranes [85]. The hydroxyl radical, produced by the Fenton reaction among H_2O_2 and $O_2^{\bullet-}$ and catalyzed by transition elements such as copper ion (Cu^+), Fe^{2+} and Fe^{3+}, is considered highly reactive and the most toxic ROS identified, rapidly attacking by lipid peroxidation cellular membrane components, mainly lipids and proteins leading to oxidative damage [82]. Singlet oxygen, a peculiar kind of ROS, highly damaging to both PSI and PSII, and the entire photosynthetic apparatus is a product of the reaction of energy transfer of a triplet excited state of a Chl molecule in the antenna complex or reaction center with molecular O_2, thus producing $^1O_2$ in the process and damaging proteins, pigments, lipids, and nucleic acids, leading to cellular death [82,88]. The membrane-permeable hydrogen peroxide, produced under normal and stressful conditions, is a relatively reactive ROS generated from the dismutation of $O_2^{\bullet-}$ by superoxide dismutase (SOD). Oxidative damage and programmed cell death occur as a consequence of H_2O_2 longer $t_{1/2}$ of 1 ms, higher cellular concentrations, and conversion into more

reactive species [82]. The superoxide anion radical is moderately reactive, and the first ROS to be generated, known to yield more reactive and toxic ROS family members, and arising at PSI non-cyclic ETC, but also mitochondrial ETC complexes I and III [82,89].

Among ROS's multifunctional roles in algae, perhaps the most important is performing as signal transduction molecules mediating many cellular processes, particularly from chloroplasts to the nucleus [81]. ROS acts as secondary messengers at low levels, transmitting stress signals to cells, enabling them to counter and acclimate to different stressors; H_2O_2 best fulfills the role of a second messenger, regulating processes such as cell division, differentiation, and growth, among others [90]. Further roles include *de novo* protein synthesis inhibition of the D1 protein, used in the repair mechanism of photodamaged PSII, and the photooxidative stress defense genes upregulation by $^1O_2$, which operate as vital cell signaling molecules that mediate photoacclimation strategies. In addition, ROS regulates apoptosis type-I programmed cell death and the starvation-induced autophagy-mediated mechanism by superoxide anion radicals [82,89,91,92].

At basal and stressful environmental conditions, ROS production sites are localized in the electron transport chain components of the chloroplast thylakoids of both photosystems, PSI and PSII. The mitochondria is a significant producer of $O_2^{\bullet-}$ in dark and stress conditions involved in ROS-induced cell death in plants, the peroxisomes constitute an important site of intracellular H_2O_2, the endoplasmic reticulum similarly produces H_2O_2, the plasma membrane by NADPH oxidases, cell wall, and even the Calvin-Benson cycle are considered important production

sites of $O_2^{\bullet-}$ and H_2O_2 [83,93,94]. At high levels of ROS, oxidative stress regulation occurs in chloroplast thylakoid membranes through a defense mechanism fundamental for photosynthesis of a series of major ROS-scavenging enzymes, such as ascorbate peroxidase (APX), catalase (CAT), glutathione peroxidase (GPX), superoxide dismutase (SOD), and thioredoxins (TRXs), but also by non-enzymatic antioxidants like ascorbic acid (AA), carotenoids, flavonoids, proline, reduced glutathione (GSH), and tocopherol [82,95]. As scavenging systems, superoxide removal with SOD metalloenzyme follows a dismutation into O_2 and H_2O_2 ($2O_2^{\bullet-} + 2H^+ \rightarrow O_2 + H_2O_2$). The hydroxyl radical is efficiently scavenged by proline, a powerful antioxidant; hydrogen peroxide is removed through the ubiquitous and tetrameric heme-containing enzyme CAT by its dismutation to H_2O and O_2 ($2H_2O_2 \rightarrow 2H_2O + O_2$), additionally by peroxidases and flavonoids, and singlet oxygen is scavenged by carotenoids, consequently generating heat as a byproduct, and the lipophilic antioxidant α-tocopherol which serves as a free radical trap [82,96,97].

The imbalance between ROS generation and antioxidant defense induces oxidative stress during stress conditions and leads to many pathologies [98]. Algae counter such harmful effects at the molecular, membrane, cellular, morphological, and physiological levels [98,99].

1.6 The Role of Oxidative Stress in the Pathogenesis of Various Human Diseases

Toxic ROS levels, leading to oxidative stress, elicit stress responses of supporting cell survival, or stimulation of DNA damage, premature chromatin

condensation, mitochondrial cytochrome c release, caspase-like enzymatic activities activation, photosynthetic activity reduction, cytoplasmic vacuolization due to the accumulation of autophagic vacuoles, depleted ATP levels, and membrane disturbances, beginning mechanisms that range from necrotic processes to genetically regulating cell death [84,100,101]. These cell death processes can include (1) the enzymatically regulated route of cell destruction due to changes in the gene expression of dying cells that ultimately exhibit a distinct morphology devoid of apoptotic body formation, unobserved in plants, called programmed cell death, (2) the arguably metazoan exclusive process of apoptosis with morphological characteristics of apoptotic bodies during or subsequently to programmed cell death, and (3) autophagy, a type II of cell death where proteins and other cell organelles are guided, enclosed by a double membrane vesicle called the autophagosome, and degraded by hydrolytic enzymes called acidic hydrolases, after fusion with lysosomes and vacuoles [84,89,90,102]. Accordingly, oxidative stress evokes the individual or simultaneous release of ROS, either chemically distinct or originating within various intracellular compartments by a different mechanism, and associated with their biological activities and in some cases like $^1O_2$ inducing a specific set of stress responses [83].

Consequently, out of all the different cell death processes, autophagy, a key defense mechanism utilized to degrade oxidized molecules, recycle or eliminate ROS-producing cellular organelles, is highly conserved among different photosynthetic organisms such as plants and algae, contributing a strong tie between autophagy and ROS in photosynthetic eukaryotes [90]. There are three

primary types of autophagy comprising: chaperone proteins (e.g., Hsc-70) mediated, which selectively translocate soluble proteins that contain a KFERQ pentapeptide motif across the lysosomal membrane for lysosomal-associated membrane protein 2A (LAMP-2A) receptor recognition, and succeeding unfolding and degradation, in microautophagy, cytosolic constituents are transported to the lysosome by a direct lysosomal membrane invagination or distortion process, and macroautophagy, capable of engulfing and delivering bulky cytoplasmic cargo to the lysosome via single membrane autophagic bodies in plants, or by the fusion of the autophagosome and lysosome which forms the autolysosome in mammals [103,104]. The double function of pro-survival, for instance, under nutrient stress conditions to safeguard the supply of crucial proteins and nutrients, and cell death autophagy-induced strategies, arise in cells, following various stimuli that require strict regulation [105,106]. Since autophagy is implicated in numerous human diseases and physiology, its research could contribute to developing therapeutic strategies for autophagy control by ROS-related diseases [89].

Some human pathologies are oxidative stress-mediated diseases attributed to unfavorable, toxic, and excessive ROS production and accumulation [107]. Oxidative damage, lipid membrane peroxidation, swelling and lysis of mitochondria, mutagenesis, and oxidative post-translational modifications of proteins (PTMs), have been associated with numerous degenerative disorders such as Alzheimer's, Parkinson's, atherosclerosis, rheumatoid arthritis, progeria, and cancer [11].

Cancer, the second leading cause of death in the United States, is a group of diseases genetically associated with autophagy dysfunction; moreover, it contains over 40 autophagy-related genes (ATG) and proteins regulating all autophagy phases: induction, nucleation, elongation, and maturation, with various roles, paradoxically, cell proliferation and tumor growth, and the generally recognized notion of tumor suppression inducing cancer cell death, as confirmed by potent autophagy-inducing anticancer therapeutic drugs such as tamoxifen and rapamycin, functioning as signaling regulators genetically-linked to oncogenic signaling [105,108–110]. Regarding the tumor suppression features of autophagy, previous studies confirm the tumor suppressor properties of ATG genes like Beclin 1 (BECN1), monoallelically deleted in 40-75% of ovarian, prostate, and human breast cancers; which in animal models and cancer cell lines, deleting BECN1 induces cell proliferation and a decrease in autophagy, suggesting a key role of autophagy in the progress of breast tissue tumors [105]. However, knockdown of the autophagic marker, the ATG genes, BECN1, and microtubule-associated light chain 3 (LC3), reveal anti-metastatic features, such as anti-proliferation, hindered colony formation, migration, and invasion, triggering apoptosis in the triple-negative breast cancer (TNBC) MDA-MB-231 cell lines [111]. Nevertheless, ROS regulation inhibits tumor generation through autophagy pathways, making autophagy a critical process that prevents tumor generation. In contrast, dysfunctional autophagy can give rise to carcinogenesis [105,106]. Research in this area comprising MDA-MB-231 cells indicates that cell cycle arrest inhibitors, nutrient starvation, or cellular stressors such as ROS H_2O_2 can induce autophagy

and mitochondrial dysfunction, driving cancer cells into senescence and thus inhibiting tumor growth [112]. Natural ROS generator anticancer drugs such as 1,3,8-trihydroxy-6-methylanthraquinone or emodin have proven to induce cancer cell death in a ROS-dependent manner via cell cycle arrest; co-treatment with chemotherapeutic drugs like cisplatin (CDDP) enhances cytotoxicity and cancer cells' sensitivity while overcoming chemoresistance [113,114]. It is also important to highlight that cell cycle regulation by arrest at a checkpoint can lead to apoptosis; thus, ROS-generating agents from natural sources can be used in cancer therapy [115].

Still, breast cancer is the most frequently diagnosed cancer in women, except for skin cancer, and the second leading cause of death of women in the United States [116]. Breast cancer has been conventionally categorized based on standardized immunohistochemistry (IHC) tests and markers such as estrogen receptor (ER), progesterone receptors (PR), and human epidermal growth factor receptor 2 (HER2) into four main subtypes: Luminal A (ER-positive, PR-positive, HER2-negative), Luminal B (ER-positive, PR-positive, HER2-negative/positive), HER2 overexpressed (ER-negative, PR-negative, HER2-positive), and TNBC or basal-like (ER-negative, PR-negative, HER2-negative) [117].

In comparison to other subtypes of breast cancer, TNBC, which add up to ~15-20% of all breast cancers, is characterized by the absence of expression of the three main IHC biomarkers, ER, PR, and HER2, and is correlated with younger African and Hispanic women diagnosis, aggressive nature, a highly metastatic and recurrence rate, and poor prognosis [118–120]. TNBC is unresponsive to

standard hormone therapy and HER2-targeted therapy; however, chemotherapeutic drugs remain the usual alternative due to sensitivity but fail in terms of chemoresistance and recurrence [121]. Although there have been noteworthy improvements in finding and developing effective treatments for TNBC, recent studies approved by the U.S. Food and Drug Administration (FDA) in inoperable and advanced metastatic tumors, expressing elevated levels of programmed cell death ligand 1 (PD-L1) were tested with atezolizumab (monoclonal antibody targeting PD-L1) and the nanoparticle-bound paclitaxel (nab-paclitaxel) or commonly known by their trade name drug Abraxane®, obtained unsuccessful results in treating the disease and prolonging survival. Current treatments with the anti-programmed death receptor 1 drug, pembrolizumab, combined with nab-paclitaxel, paclitaxel, or gemcitabine/carboplatin chemotherapeutic drugs revealed statistically significant results. However, further studies are required to identify and develop effective therapeutic strategies to improve the patient's survival [122]. Therapeutic protein delivery to cancerous cells is challenging due to high molecular weight proteins, surface charge, solubility and stability issues, circulation time, rapid removal, immunogenicity, non-specific cytotoxicity, and endosomal entrapment; nonetheless, protein drugs potency, specificity, tumor inhibition, and their capacity to induce cancer cell death by apoptotic and necrotic mechanisms through specific signaling pathways and lower half-maximal inhibitory concentration (IC_{50}) values, as well as a wide range of applications hold great potential in cancer treatment [123–125].

This research ultimately focused on assessing the ROS producing green microalga *B. braunii* photosynthetic apparatus component, PSI, and its antenna LHCI, potential treatment benefits in the life-threatening disease of TNBC. This thesis project may further our knowledge for developing novel drugs from natural sources for breast cancer disease and the mechanism of cell death elicited by ROS-enriched photosynthetic microorganisms.

1.7 Specific Aims

The following specific aims were developed to evaluate a ROS-containing photosynthetic complex's applicability as a potential therapeutic protein for cancer treatment:

Specific Aim 1. Isolate and characterize photosystem I (PSI) light-harvesting complex I (LHCI) of the photosynthetic apparatus of *B. braunii*

B. braunii cells were harvested and broken via mechanical cell disruption grinding method for optimum rupture of the rigid cell wall and intracellular protein extraction. The ultracentrifugation technique enabled cell debris separation and pellet thylakoid membranes, further solubilized with detergents. Freshly prepared solubilized thylakoids underwent electron microscopy to provide morphological information and experienced various isolation and purification methods for identifying the multiprotein complex, starting with a discontinuous sucrose density gradient centrifugation, followed by a strong anion-exchange column. The Chl

concentration was determined spectrophotometrically after extraction in 90% methanol according to Lichtenthaler and Buschmann equations and Meeks and Castenholz extinction coefficient [126,127]. The PSI complex's room temperature absorption and fluorescence emission spectra were measured using an ultraviolet-visible (UV/Vis) spectrophotometer and a fluorescence spectrophotometer, obtaining the characteristics peaks for PSI-RC and PSI-LHCI. Low-temperature (77K) fluorescence emission measurements were recorded with an excitation at 436 nm and served to distinguish the association between photosystem complexes and light-harvesting systems by each of their characteristic emissions [128]. The photosystems and light-harvesting complexes' protein composition were characterized via sodium dodecyl sulfate-polyacrylamide gel electrophoresis (SDS-PAGE) analysis. Blue native (BN) PAGE and two-dimensional (2D) PAGE allowed the separation and characterization of the PSI-LHCI supercomplex. With the results obtained from this study, we provided the fundamental knowledge of this microalga's photosynthetic apparatus missing from the literature.

Specific Aim 2. To determine the mechanism of cell death following the intracellular delivery of PSI-LHCI into TNBC cells for cell-based therapeutics

Oxidative stress by an overwhelming generation of ROS can trigger cell damage and death. We hypothesized that the ROS-containing PSI-LHCI isolated from the green microalga *B. braunii*, prepared following the Specific Aim 1 experimental procedure, could induce cell death and be therapeutically interesting.

At first, we investigated the photoprotective effect of Chl *a* against oxidative stress. Next, we conducted *in vitro* cell viability studies and investigated cell death mechanisms in breast cancer cell lines; a concentration-dependent reduction in cell viability was observed after incubation using various concentrations of PSI-LHCI. Fluorescence confocal microscopy studies assessed internalization, and Z-series were performed to visualize PSI-LHCI's cytoplasmic intracellular localization. Live-cell imaging allowed total ROS production and superoxide detection. We determined that PSI-LHCI under serum starvation conditions induced autophagy, and studies with propidium iodide only exhibited a red concentrated cell nucleus suggesting necrotic cell staining. In contrast, Annexin V did not show any typical early apoptosis markers. Consequently, our results confirm that TNBC MDA-MB-231 cells undergo autophagy concomitant with necrotic-like cell death after treatment with PSI-LHCI for 24 h due to the overwhelming ROS levels.

Materials and Methods

2.1 Experimental procedures – Chapter 3

2.1.1 Materials

Strain: *Botryococcus braunii* UTEX 2441 strain race A was obtained from The Culture Collection of the University of Texas at Austin. Medium: modified Chu 13 medium components: KNO_3, K_2HPO_4, $MgSO_4 \cdot 7H_2O$, $CaCl_2 \cdot 2H_2O$, Ferric citrate, citric acid, $CoCl_2$, H_3BO_3, $MnCl_2 \cdot 4H_2O$, $ZnSO_4 \cdot 7H_2O$, $CuSO_4 \cdot 5H_2O$, Na_2MoO_4, H_2SO_4 were obtained from Sigma-Aldrich (St. Louis, MO) [129]. Breaking buffer: 4-(2-Hydroxyethyl)piperazine-1-ethanesulfonic acid (HEPES), $MgCl_2$, $CaCl_2$, glycerol were purchased from Sigma-Aldrich (St. Louis, MO). Protease inhibitors: phenylmethylsulfonyl fluoride (PMSF), ethylenediaminetetraacetic acid (EDTA), Benzamidine, and SIGMAFAST™ protease inhibitor tablets were obtained from Sigma-Aldrich (St. Louis, MO). Detergent: *n*-dodecyl-β-D-maltoside (DDM) was purchased from Sigma-Aldrich (St. Louis, MO). Solvents: methanol, acetone, acetic acid, and ethanol (≥99.5%) were purchased from Sigma-Aldrich (St. Louis, MO). Gradients: Percoll and sucrose were obtained from Sigma-Aldrich (St. Louis, MO). Mechanical disruption: the Beadbeater and glass beads, 0.5 mm in diameter, are from BioSpec Products (Bartlesville, OK). Protein concentration: the Pierce™ BCA protein assay kit was acquired from Thermo Fisher Scientific (Waltham, MA), and the chromatographically purified albumin from bovine serum (BSA) was purchased from Sigma-Aldrich (St. Louis, MO). Gel electrophoresis: 4-15% Mini-PROTEAN®

TGX™ precast protein gels, 2X Laemmli sample buffer, dithiothreitol (DTT), 2-mercaptoethanol, SDS, ammonium persulfate (APS), *N,N,N',N'*-Tetramethylethylenediamine (TEMED), 30% Acrylamide/Bis solution (29:1), Tris base, 10x Tris/Glycine/SDS, Precision Plus Protein™ Kaleidoscope™ prestained protein standard, and Coomassie Brilliant Blue G-250 were purchased from Bio-rad (Hercules, CA). For BN-PAGE, and 2D-PAGE; NativePAGE™ 4-16% Bis-Tris protein gels, NativePAGE™ 4X sample buffer and 5% G-250 sample additive, 20X running buffer and 20X cathode buffer additive, Native Mark™ unstained protein standard, 4-12% Bis-Tris 2D-well protein gels, NuPAGE® 4X LDS sample buffer, 10X sample reducing agent, and MES SDS buffer kit were from Invitrogen (Waltham, MA), N,N-dimethylacrylamide (DMA) and ProteoSilver™ silver staining kit were acquired from Sigma-Aldrich (St. Louis, MO).

2.1.2 Culture Strain and Growth Conditions

The unicellular microalga, *Botryococcus braunii* UTEX 2441 Race A (hereafter referred to as *B. braunii*), was obtained from The Culture Collection of the University of Texas at Austin. Cells were grown at 23 °C in sterilized modified Chu 13 medium (mg/L): KNO_3 (400), K_2HPO_4 (80), $MgSO_4 \cdot 7H_2O$ (200), $CaCl_2 \cdot 2H_2O$ (107), Ferric citrate (20), citric acid (100), $CoCl_2$ (0.02), H_3BO_3 (5.72), $MnCl_2 \cdot 4H_2O$ (3.62), $ZnSO_4 \cdot 7H_2O$ (0.44), $CuSO_4 \cdot 5H_2O$ (0.16), Na_2MoO_4 (0.084), 1 drop of 0.072N H_2SO_4 in a UTEX 2L glass photobioreactor system, which provided gas exchange and mixing by air bubbling. Cultures were under 50 μmol $m^{-2}s^{-1}$ photons of white light illumination (Phillips) with a 16:8 h light-dark cycle. *B. braunii*

cells from 50 ml suspension were harvested at their logarithmic growth phase by centrifugation at 3,000 × g at 4 ˚C for 10 min and washed twice in breaking buffer A [50 mM HEPES (pH 7.2), 5 mM $MgCl_2$, 5 mM $CaCl_2$] with 20% glycerol (v/v).

2.1.3 Thylakoid Membrane Preparation

All preparations were performed in the dark or a dim light room at 4 ˚C. The collected cells were suspended in ice-cold breaking buffer A and supplemented with 1 mM EDTA and 1X protease inhibitor cocktail (Sigma-Aldrich). Cells were disrupted in a 15 ml chamber of a pre-chilled Mini Beadbeater homogenizer (BioSpec Products) filled halfway with ice-cold 0.5 mm glass beads for 25 cycles of 15 s beating and 2 min cooling on an ice-filled sealed chamber. Cell debris, intact cells, starch granules, and glass beads settled down as a pellet and were removed by centrifugation at 3,000 × g at 4 ˚C for 5 min. The resulting supernatant was collected and centrifuged at 32,600 rpm with a ThermoScientific AH-650 rotor at 4 ˚C for 30 min. The pellet of thylakoid membranes was suspended in the supplemented breaking buffer A containing 1% (w/v) *n*-dodecyl-β-D-maltoside (DDM). Briefly, a freshly prepared solution of 10% (w/v) DDM was added dropwise to the suspension until a 1% DDM concentration was reached. To solubilize the thylakoids, the extraction was performed in the dark, in a cold room, and under gentle stirring for 15 min. Subsequently, the solubilized thylakoids were centrifuged at 36,200 rpm with a Thermo Scientific AH-650 rotor at 4 ˚C for 20 min to obtain stroma membranes as a supernatant; the resulting pellet corresponded to the grana preparation and was discarded. The stromal thylakoid supernatant was

stored at -80 ˚C until further use. Thylakoid membrane morphology was inspected with the JEOL 6480 LV by scanning electron microscopy (SEM) at 10, 15, and 20 kV. Centrifugation of isolated chloroplast samples was performed in a 40/80% Percoll gradient; later samples were coated with gold for 10 s using a PELCO SC-7.

2.1.4 Purification of PSI from *Botryococcus braunii*

Stromal thylakoids were loaded onto a discontinuous sucrose density gradient in the range of 0.1 to 1.5 M in supplemented breaking buffer A with 1 mM EDTA, 1X protease inhibitor cocktail, 0.03% (w/v) DDM, and centrifuged at 37,500 rpm with a Thermo Scientific TH-641 rotor at 4 ˚C for 16.5 h. The lower green band obtained, corresponding to the PSI-enriched fraction, was collected using a syringe, concentrated with a centrifugal filter unit (10,000 NMWL, Millipore), and stored at -80 ˚C. Alternatively, a fast protein liquid chromatography (FPLC) system (ÄKTA purifier UPC 10, GE Healthcare) was used to purify the PSI reaction center (PSI- RC) with the HiTrap Capto Q (5 ml) prepacked strong anion exchanger with supplemented breaking buffer A and 0.03% DDM. These initial conditions were used to equilibrate, wash the column, and extract free pigments and loosely bound proteins. The elution buffer A comprised [50 mM HEPES (pH 7.2), 5 mM $MgCl_2$, 12 mM $CaCl_2$], 20% glycerol (v/v), 1X protease inhibitor, 1 mM EDTA, 0.03% (w/v) DDM, and 100 mM $MgSO_4$. The eluted fraction was pooled and concentrated with a centrifugal filter unit (10,000 NMWL, Millipore).

2.1.5 Absorption and Fluorescence Spectroscopy

Absorption spectra were measured at room temperature (RT) using a UV-2450 UV/Vis spectrophotometer (Shimadzu) using 1 cm (10 mm) path length quartz cuvettes. Scanning was performed on the visible region up to 800 nm. Thylakoids and FPLC purified PSI-RC fluorescence emission spectra at 293 K were recorded between 600 to 800 nm with a Cary Eclipse fluorescence spectrophotometer by exciting with a blue light wavelength of 436 nm. Also, FPLC purified PSI-RC fluorescence excitation spectra at 293 K were recorded from 400-650 nm with an emission wavelength of 679 nm. PSI-LHCI sucrose fraction and glycerol fractions low-temperature 77K fluorescence emission spectra were recorded from 630 to 800 nm and measured using a Fluoromax-4 spectrofluorometer (Horiba Scientific) equipped with a low-temperature holder at an excitation wavelength of 436 nm. Before 77K fluorescence measurements, each sample was cooled in liquid nitrogen in a cryostat. Pigment content was determined after extraction in 90% (v/v) methanol according to Meeks and Castenholz extinction coefficient, and Lichtenthaler and Buschmann equations [126]:

$$\text{Chl a } (\mu\text{g/ml}) = 16.82\, A_{665.2} - 9.28\, A_{652.4}$$

$$\text{Chl b } (\mu\text{g/ml}) = 36.92\, A_{652.4} - 16.54\, A_{665.2}$$

$$\text{Carotenoids } (\mu\text{g/ml}) = 1000\, A_{470} - 1.91 \text{ Chl a} - 95.15 \text{ Chl b}) / 225$$

Protein concentration was determined with the BCA protein assay kit (Pierce), using diluted BSA standards from a 2 mg/ml stock.

2.1.6 Circular Dichroism Spectroscopy

Circular Dichroism (CD) spectra were obtained using a JASCO J-1500 CD Spectrometer at a scanning speed of 50 nm/min, a bandwidth of 1 nm, and at 25 ˚C. Visible range measurements between 350 and 750 nm were recorded with a 10 mm quartz cuvette with previously desalted sucrose gradient purified PSI-LHCI and thylakoid membrane samples at 0.4 mg/ml Chl concentration. Final spectra were normalized to the maximum peak in the red region, averaged from three scans, and corrected by subtracting the breaking buffer A spectra acquired under the same conditions.

2.1.7 Protein Composition Analysis

The protein composition of *B. braunii* was analyzed using SDS-PAGE with a 10% (w/v) SDS polyacrylamide resolving gel and 5% SDS polyacrylamide stacking gel and run according to the manufacturer's protocol (Bio-Rad) with 1X Tris/Glycine/SDS buffer system on a Mini-Protean electrophoresis cell system (Bio-Rad). Beforehand, protein samples were solubilized in Laemmli sample buffer (2X) containing 50 µL of ß-mercaptoethanol and incubated at 95 ˚C for 5 min in a gradient thermal cycler (Eppendorf) immediately before electrophoresis. A prestained protein standard (Bio-Rad) was used as a molecular weight marker to follow the progress of proteins 5-10 mm into the resolving part of the gel. Identification of protein subunits submitted as gel plugs was performed by running

samples for 1 h on a Dionex LC system and Orbitrap mass spectrometer for LC-MS/MS (Proteomics Facility, TX). Blue Native PAGE (BN-PAGE) of *B. braunii* thylakoids and sucrose gradient purified PSI-LHCI sample (0.7 mg/ml Chl) was performed in a 4-16 % gradient Novex Bis-Tris gel, 5% G-250 sample additive, pre-chilled 1X running buffers and 1X NativePage sample buffer, at constant 150 V and for up to 120 min, as indicated in the manufacturer's recommended protocol (Invitrogen). Mass estimation was achieved using NativeMark unstained protein standard (Invitrogen) to generate a molecular weight (MW) standard curve of the log MW versus the migration distance of the protein through the gel divided by the migration distance of the dye front (R_f). Protein bands were detected with Coomassie Brilliant Blue G-250 and silver staining kit (Sigma-Aldrich). Two-dimensional (2D) native/ SDS-PAGE was accomplished in a gradient 4-12% NuPAGE Bis-Tris gel in 1X MES running buffer at constant 150 V for 1 h with the excised PSI-LHCI BN-PAGE gel lane obtained that underwent reduction, alkylation, and quenching as indicated in the manufacturer's protocol (Invitrogen). We used a prestained protein standard (Thermo Fisher Scientific) to estimate PSI components' apparent size.

2.2 Experimental procedures – Chapter 4

2.2.1 Materials

B. braunii (UTEX 2441) was purchased from The Culture Collection of the University of Texas at Austin. Chu 13 medium components, L-Glutathione reduced, Uric acid, L-Ascorbic acid, Imidazole, 3-(3,4-Dichlorophenyl)-1,1-dimethylurea (DCMU), D-α-Tocopherol polyethylene glycol succinate, Sodium hydroxide (NaOH), Dimethyl sulfoxide (DMSO), *N,N*-Dimethylformamide (DMF), formaldehyde solution (37%), Minimum Essential Medium (MEM), Dulbecco's Modified Eagle's Medium (DMEM), Leibovitz's Medium with L-Glutamine (L-15), phosphate buffered saline (PBS), penicillin/streptomycin (Pen/Strep) solution, L-Glutamine solution, and fetal bovine serum (FBS) were purchased from Sigma-Aldrich (St. Louis, MO). The CellMask™ green plasma membrane stain, NucBlue™ 4',6-diamidino-2-phenylindole (DAPI), Annexin Dead Cell Apoptosis Kit with Annexin V Alexa Fluor® 488 and propidium iodide (PI), and FM™ 4-64 (*N*-(3-Triethylammoniumpropyl)-4-(6-(4-(Diethylamino) Phenyl) Hexatrienyl) Pyridinium Dibromide) dye were purchased from Invitrogen (Waltham, MA). Hanks' balanced salt solution 1X (HBSS) and 0.25% Trypsin-EDTA solution was purchased from Gibco (Waltham, MA). The CellTiter 96® AQ_{ueous} non-radioactive cell proliferation assay was purchased from Promega Corporation (Madison, WI). HeLa, MDA-MB-231, MDA-MB-468, NIH-3T3 cells were purchased from the American Type

Culture Collection (Manassas, VA). The JC-1 mitochondrial membrane potential detection assay kit and NucView 405 Caspase-3 substrate were purchased from Biotium, Inc (Freemont, CA). Nuclear Green™ DCS1 was obtained from AAT Bioquest®, Inc. (Sunnyvale, CA). Staurosporine 99+% was obtained from Thermo Fisher Scientific (Waltham, MA). Docetaxel and the fluorometric intracellular ROS kit were purchased from Sigma-Aldrich (St. Louis, MO). The cellular ROS/Superoxide detection and autophagy assays were obtained from Abcam Inc. (Cambridge, MA). All analytical-grade chemicals were acquired from various suppliers and used without further purification.

2.2.2 Cell Culture Conditions

HeLa (ATCC® CCL-2™) cells from human epithelial cervix adenocarcinoma, MDA-MB-231 (ATCC® HTB-26™) cells from human epithelial breast adenocarcinoma, MDA-MB-468 (ATCC® HTB-132™) cells from human epithelial breast adenocarcinoma, and NIH-3T3 (ATCC® CRL-1658™) cells from mouse fibroblast were maintained according to the culture methods specified by the American Type Culture Collection. Briefly, MDA-MB-231 and MDA-MB-468 breast cancer cells were cultivated in 75 cm^2 flasks in L-15 Medium containing L-Glutamine, supplemented with a final concentration of 10% FBS, and 1% Pen/Strep in a humidified incubator with 0% CO_2 at 37 °C. NIH-3T3 cells were cultured in DMEM comprising L-Glutamine, supplemented with 10% FBS and 1% Pen/Strep in a humidified incubator with 95% air and 5% CO_2 at 37 °C. HeLa cells were grown in MEM containing L-Glutamine, 10% FBS, and 1% Pen/Strep in a

humidified incubator with 5% CO_2 and 95% air atmosphere at 37 °C. Before the cells reached confluency, they were seeded to 96-well plates or 4-well chambered coverglass plates for further analysis. Trypsin-EDTA 1X was used for cell splitting and passage. Cell cycle arrest for 18 h was performed by serum starvation with a decrease from 10% FBS to 1% FBS concentration in the cell culture media. Next, cells were incubated with different PSI-LHCI sample concentrations and negative and positive controls for 6, 12, and/or 24 h. All experiments were performed before the cells reached 20 passages.

2.2.3 Cell Viability Assay

HeLa, MDA-MB-231, MDA-MB-468, and NIH-3T3 cells were seeded in sterile 96-well cell culture plates in MEM, L-15 Medium or DMEM containing L-Glutamine, 10% FBS, and 1% Pen/Strep at a density of 10,000 cells per well and incubated for 24 h at 37 °C in 0% CO_2 or 5% CO_2 atmosphere according to each cell given specifications. After 24 h of incubation, cell arrest was achieved by reducing FBS concentration in the medium to 1% for 18 h. Cells were washed with 1X PBS and treated with different concentrations (6.25, 12.5, 25, 50 µg/ml) of PSI-LHCI for various incubation times (6, 12, 24 h). At the end of treatment, 20 µl of the assay solution containing (3-(4,5-dimethylthiazol-2-yl)-5-(3-carboxymethoxyphenyl)-2-(4-sulfophenyl)-2H-tetrazolium) (MTS) and the electron coupling reagent phenazine ethosulfate (PES) was added to each sample well, incubation for 1-4 h followed absorbance measurements recorded at 490 nm using a 96-well Tecan reader to determine the percentage of cell viability following the

general protocol provided by the manufacturer where the amount of soluble formazan produced by cellular reduction of the tetrazolium compound MTS is determined. Positive (2 μM Staurosporine and 20 nM Docetaxel) controls, buffer extraction medium, and untreated cells were used as a negative control. The IC_{50} value of PSI-LHCI for the concentrations (3.125, 6.25, 12.5, 25, and 50 μg/ml) in MDA-MB-231 cells was calculated from the MTS assay results. The cell viability percentiles obtained were analyzed through GraphPad Prism 6 software program by transforming the X values to logarithms of concentration, normalizing the Y values setting the lowest values in each data set to 0% and defining 100% by the largest value in each data set. At least three experimental replicate results were performed. For phototoxicity studies, cells were irradiated with a light-emitting diode (LED) lamp (λ_{max}=660 ± 10 nm) at a distance of 10 cm from the 96-well plate and a fluence rate of 50 mW/cm^2 for 10 min.

2.2.4 Internalization Study of PSI

Initially, cells were plated in 4-well chambered coverglass plates at a density of 10,000 cells per well and incubated overnight in L-15 Medium. Next, cells were arrested for 18 h and incubated with the point closest to the IC_{50} concentration of PSI-LHCI (12.5 μg/ml) for 6, 12, and 24 h. Afterward, cells were washed three times with PBS 1X for 10 min, stained with CellMask™ green plasma membrane dye (Ex/Em = 522/535 nm) for 15 min, and fixed for 20 min with a 3.7% formaldehyde solution at room temperature (RT). After removing the fixing solution and washing it three times with PBS 1X for 5 min, cells were incubated with the

nuclear counterstain NucBlue™ DAPI and the dead, fixed, or apoptotic DNA-selective dye Nuclear Green™ DCS1 (Ex/Em = 503/526 nm) for 15 min at RT, then rapidly removed and washed three times with PBS 1X. Excess wash buffer was removed, cell wells protected from the light, and wells carefully filled with glycerol. Cells were analyzed by in-depth optical sectioning through the sample along the z-axis (Z-series), generating a 3-D image in a Nikon Eclipse Ti confocal laser scanning microscope with a 60X objective and the appropriate dye channels. Untreated control cells were used to detect autofluorescence. Fluorescence intensity was analyzed using NIS-Elements Advanced Research Imaging Software (version 5.20).

2.2.5 Chlorophyll fluorescence induction kinetics

B. braunii UTEX 2441 cells were cultured in modified Chu 13 medium in a UTEX 2L glass photobioreactor system, following Section 2.1.2 set of conditions. For determining the rapid fluorescence transient curves, OJIP, O = Origin, J and I = Intermediate steps, P = peak, *B. braunii* cells samples were harvested at 4 °C, 6,500 *g* for 10 min, resuspended in water, and prepared to a final concentration of 50 µg/ml. *B. braunii* cells were tested with the photosynthetic electron transfer inhibitor DCMU (20 µM) prepared from an ethanol stock solution. Cells were also examined with exogenous nonenzymatic antioxidants and radical scavengers such as 5 mM imidazole, 5 mg/ml L-glutathione reduced, 5 mg/ml L-ascorbic acid, 5 mg/ml uric acid prepared from a 1 M NaOH stock solution, and 5 mg/ml D-α-tocopherol polyethylene glycol succinate added from a stock solution in ethanol.

B. braunii cells were transferred to a 2 ml measurement cuvette and kept in the dark covered for 10 min. Monitoring of the OJIP chlorophyll fluorescent transient analysis of cells was performed upon intense light excitation (3000 μmol photons m^{-2} s^{-1}; λ_{exc} = 450 nm), using the AquaPen-C handheld version of a fluorometer. Each displayed OJIP curve is an average of three independent measurements.

2.2.6 Study of Thylakoid and PSI ROS/Superoxide Generation

The production of the ROS $^1O_2$ upon light irradiation in the isolated thylakoid membrane and PSI (0.5 mg/ml) samples was determined using the spectrometric RNO bleaching assay [130]. The solutions prepared in PBS (pH 7.4) and mixed with each of the samples and controls included 50 μM of the selective scavenger *p*-nitrosodimethylaniline (RNO) and 10 μM of the $^1O_2$ acceptor imidazole. Chlorin e6 (0.5 mg/ml) (Ce6), a second-generation photosensitizer and chlorophyll analog, was used as a singlet oxygen generator positive control and PBS as a negative control. The time course of RNO bleaching was followed spectrophotometrically at 440 nm. Samples and controls were exposed by irradiation to a continuous LED lamp light source (λ_{max}=660 ± 10 nm) at a distance of 10 cm, a fluence rate of 50 mW/cm^2 for 40 min while bubbling with O_2. After incubation, the rate of $^1O_2$ production was determined by measuring the reduction of RNO absorbance, normalized at 440 nm. The ROS/Superoxide Detection Assay Kit (Abcam ab139476) was used to detect total ROS and superoxide production in live MDA-MB-231 cells. First, cells were seeded in sterile 4-well chambered coverglass plates at a density of 10,000 cells per well and incubated for 24 h in L-15 Medium

containing L-Glutamine, 10% FBS, and 1% penicillin/streptomycin at 37 °C in 0% CO_2. After 18 h of serum starvation in 1% FBS L-15 medium, cells were treated with the point closest to the IC_{50} concentration (12.5 µg/ml) of PSI-LHCI for 24 h. In brief, the green oxidative stress reagent (5 mM) that directly reacts and detects H_2O_2, peroxynitrite ($ONOO^-$), ·OH, NO·, and ROO·, the orange superoxide detection reagent (5 mM) that reacts specifically with $O_2^{\bullet-}$, and the positive control and ROS inducer pyocyanin (200 µM) were reconstituted in DMF. Before induction, cells were pre-treated for 30 min with the negative control and ROS inhibitor N-acetyl-L-cysteine (5 mM). Next, cells were loaded with 2X ROS/Superoxide detection mix, prepared by mixing the green and orange reagents in 1X wash buffer to obtain a 1:2500 diluted staining solution as specified by the manufacturers' instructions with PSI-LHCI and the ROS inducer pyocyanin (200 µM). After incubation for 30 min to 1 h at 37 °C, the staining mix solution was removed, washed twice with 1X wash buffer, and the cells were examined using a Nikon Eclipse Ti confocal laser scanning microscope with filter sets compatible with fluorescein (Ex/Em = 490/525 nm) and rhodamine (Ex/Em = 550/620 nm). Fluorescence intensity was analyzed using NIS-Elements Advanced Research Imaging Software (version 5.20).

2.2.7 Annexin V/Propidium Iodide Assay and Caspase 3 Colorimetric Assay

MDA-MB-231 cells were seeded as described before in sterile 4-well chambered plates or 24-well cell culture plates with a 12 mm round glass coverslip and incubated for 24 h in L-15 Medium supplemented with L-Glutamine, 10% FBS,

and 1% Pen/Strep at 37 °C in 0% CO_2. After cell cycle arrest with 1% FBS in the culture medium for 18 h, cells were treated with the point closest to the IC_{50} concentration (12.5 µg/ml) of PSI-LHCI and incubated at 37 °C for 24 h. Afterward, cells were washed with 1X PBS (pH 7.4) and incubated with DAPI, Annexin V, and PI (75 µM) for 5 min. Subsequently, cells were fixed with 3.7% formaldehyde solution for 20 min, washed three times with 1X PBS, and covered with glycerol prior to visualization. Afterward, fixed cells were analyzed to confirm cell death under a Nikon Eclipse Ti confocal laser scanning microscope utilizing a 20X or 60X oil objective with filter sets compatible with DAPI (Ex/Em = 405/420-480 nm), Annexin V Alexa Fluor excited at 488 nm with no emission detected, PSI-LHCI (Ex/Em = 640/663-738 nm, PI (Ex/Em = 561/600-674 nm), and Nuclear Green™ DCS1 (Ex/Em = 503/526 nm). Additionally, 2 µM NucView 405 Caspase-3 Substrate was used for detecting apoptosis in intact cells based on caspase-3/7 activity using confocal microscopy. Briefly, cells were incubated for 30 min at RT with NucView 405 substrate, washed three times with 1X PBS, fixed for 20 min, then washed three times with 1X PBS. After cell fixing, wells were filled with glycerol and stored in the cold room until confocal laser microscopy was performed.

2.2.8 J-C1 Mitochondrial Membrane Potential Assay

The fluorescence-based measurement of mitochondrial membrane potential ($\Delta\Psi M$) of MDA-MB-231 cells was evaluated after treatment with the concentration closest to the point of the IC_{50} (12.5 µg/ml) of PSI-LHCI and using

the J-C1 dye. Briefly, MDA-MB-231 cells were seeded at 10,000 cells/well density in sterile 96-well plates and treated following the above-mentioned cell culturing, serum starvation, and PSI-LHCI treatment specifications. Staining was performed by removing L-15 Medium from PSI-LHCI treated cells, replacing it with J-C1, and incubating for 15 min in a humidified incubator at 37 °C. After incubation, the J-C1 working solution was removed and cells were washed once with 1X PBS. Afterward, wells were covered with 1X PBS, and using the Tecan microplate reader, red fluorescence (excitation at 550 nm, emission at 600 nm) and green fluorescence (excitation at 485 nm, emission at 535 nm) were recorded. The red fluorescence to green fluorescence ratio was determined by dividing both measurements, where a decrease in the ratio is attributed to dead cells or cells undergoing programmed cell death.

2.2.9 Autophagy Assay

An autophagy detection protocol was performed as a fast, specific, and quantifiable method for monitoring lysosome-mediated autophagic activity in cells by fluorescence microscopy. MDA-MB-231 cells were initially grown in 75 cm^2 tissue culture flasks; when the cells had reached a 70% level of confluence, they were transferred to 4-well chambered coverglass plates at a density of 10,000 cells/well and grown in L-15 medium supplemented with L-Glutamine, 10% FBS, and 1% Pen/Strep at 37 °C in 0% CO_2 usual conditions. The autophagy inducer rapamycin (500 nM) and the lysosomal activity inhibitor chloroquine (20 μM) were used as positive controls; untreated cells in media and extraction buffer were used

as the negative control. Cells were pre-treated with rapamycin and chloroquine for 18 h; for chloroquine, starvation conditions in 1% FBS L-15 medium was employed. After the 24 h of initial seeding in the experimental chamber, cells were arrested for 18 h and incubated for 24 h with PSI-LHCI (12.5 µg/ml) in 1% FBS L-15 media. After treatment, the culture medium was removed with the testing reagents and positive controls, and the cells were washed two times with 1X Assay buffer containing 5% FBS. Approximately 500 µl of the Green Microscopy Dual Detection Reagent was added to cover each sample. The samples were protected from the light and incubated for 30 min at 37 °C and 0% CO_2. Next, cells were washed with 100 µl of 1X Assay buffer without FBS and fixed with 3.7% formaldehyde solution for 20 min at RT. Then, the fixing solution was removed, and the 4-well chambered coverglass plates were washed three times with 1X Assay buffer without FBS. Autophagic vacuoles fluorescent signal was analyzed by confocal microscopy using a standard FITC (green) filter set. Nuclei were counterstained with DAPI (blue).

2.2.10 Statistical Analysis

All experiments were performed at least as three biological replicates, plotting values with an average of 8 measurements for each treatment condition as mean ± SD. The quantitative data were analyzed with the statistical software GraphPad Prism 6. Statistical analysis was performed using two-way analysis of variance (ANOVA).

Purification and Characterization of Photosystem I Light-Harvesting Complex I (PSI-LHCI) from the Green Microalga Botryococcus braunii

3.1 Abstract

The purification of Photosystem I Light-Harvesting Complex I (PSI-LHCI) from *Botryococcus braunii* (*B. braunii*) UTEX 2441 was examined. Following the purification by either fast protein liquid chromatography (FPLC) or sucrose-density gradient ultracentrifugation, characterization studies such as absorption, fluorescence, and circular dichroism (CD) spectroscopy, plus polypeptide composition analyses were performed to confirm the main characteristics of the photosystem complex. The data indicated an absorption peak of 679 nm in PSI-LHCI, whereas a characteristic maximum of 677 nm was observed in the PSI reaction center. 77K fluorescence emission spectra showed two peaks, a narrow ~677 nm corresponding to detached LHCI and a broad ~715 nm band typically seen in PSI. Circular dichroism analysis and SDS-PAGE and Blue-Native PAGE further confirmed the presence of PSI-LHCI constituents. Our study has revealed fundamental results regarding the outcome of the PSI reaction center and PSI-LHCI preparation achieved through chromatography or centrifugation separation techniques, facilitating further discoveries of *B. braunii* photosystem complexes.

3.2 Introduction

In the initial stages of oxygenic photosynthesis in algae, light energy is converted into chemical energy. The energy conversion is catalyzed by soluble factors, electron donors and acceptors, and large protein complexes located in the photosynthetic membrane [131]. The photosynthetic apparatus is comprised of two photosystems, photosystem I (PSI) and photosystem II (PSII), that operate in series, each with its own polypeptide-rich reaction center and light-harvesting antenna protein-bound pigment complexes (LHCI, LHCII) associated with them [43,132,133]. PSI is a multisubunit thylakoid membrane-bound pigment-protein complex that drives the light-induced electron transfer from plastocyanin to ferredoxin [134]. PSI has usually been recovered as a trimer or a monomer in cyanobacteria and a monomer or supercomplex of a monomer with the associated light-harvesting antenna complex of PSI (LHCI) in higher plants and green algae [135,136]. The eukaryotic PSI reaction center contains 13 subunits from psaA to psaN. However, psaO appears to be present in green algae and LHCI, which in plants have up to six Lhca subunits [134,137]. PSI core is comprised of psaA/psaB genes binding the primary electron donor P700 chlorophyll dimer and containing the electron acceptors A_0, A_1, and F_x (4Fe-4S) iron-sulfur center. The last components in the electron transport chain, F_A, F_B, and iron-sulfur centers, are coordinated to the psaC gene [138].

B. braunii is a green photosynthetic microalga, a member of the Chlorophyceae class, highly studied due to its hydrocarbon accumulation

capability, secretion, and synthesis [23,25]. *B. braunii* is a green colonial microalga primarily found in fresh and brackish water, reservoirs, and ponds. Under the microscope, colonies of *B. braunii* exhibit a botryoid form of individual pyriform-shaped cells held together by a lipid-containing matrix [23,139]. The matrix's base structure comprises outer walls formed from successive cellular divisions, with the bulk of *B. braunii* hydrocarbons stored in these outer walls [28]. Aside from chlorophyll, this alga contains lutein and β-carotene as their major carotenoid constituents [26]. *B. braunii* is classified into three different races: A, B, and L, defined by the liquid hydrocarbons the microalgae produce. Race A produces majorly C_{25} to C_{31} odd-numbered n-alkadienes, mono-, tri-, tetra-, pentaenes derived from fatty acids [32]. This race has a pale yellow to green colony color in the stationary growth phase and has a distinctive feature among other races with long-chain alkenyl phenols [30].

So far, studies of the photosynthetic apparatus of *B. braunii* have been overlooked, as the focus on the hydrocarbon-accumulation properties of this microalga dominates their research. *B. braunii* is an example of a microorganism that can accumulate up to 86% of its dry weight as hydrocarbon oils, potentially used as a renewable fuel such as biodiesel [7,21,22]. In this work, we were able to elucidate the pigment-protein composition of the PSI-LHCI complex of *B. braunii* after purification by sucrose density gradient ultracentrifugation and characterization studies. The results presented herein have been resolved for the first time while prompting additional work and further knowledge to delve into

alternative applications of *B. braunii* photosynthetic apparatus components, particularly PSI reaction center and PSI-LHCI.

3.3 Results and Discussion

3.3.1 Thylakoid Membrane Preparation and Solubilization

The thylakoid membranes of *B. braunii* were solubilized after a preliminary extraction process to evaluate the best n-Dodecyl β-D-maltoside (DDM) concentration needed via UV-Visible spectroscopy. Mild non-ionic detergents such as DDM are widely used to isolate intact and functional photosynthetic complexes from integral membrane proteins, like PSI, while maintaining protein solubility in solution [140]. Figure 3.1 represents the effect of different DDM concentrations on the absorption spectra at 293.15 K of stroma thylakoid membranes (STM), separated by differential centrifugation. The optimal solubilizing condition for the extraction of PSI from thylakoids was 1% (w/v) DDM; confirmed by the high absorbance peak in stroma membranes at that concentration. A minor red-shift of 6 nm was observed in 1% (w/v) DDM, PSI-rich STM sample, denoting contribution from light-harvesting complex proteins, free pigments, and PSI in the preparation [39,141,142].

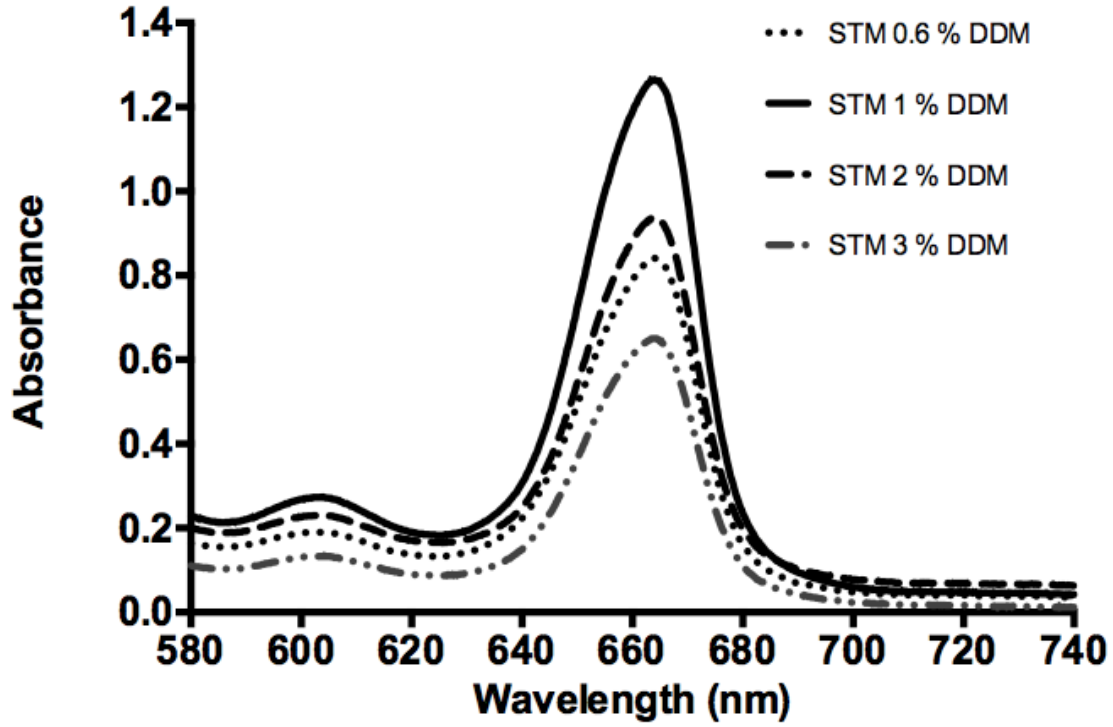

Figure 3.1 Standard room temperature absorption spectra of solubilized stroma thylakoid membranes (STM), 10 mg Chl/ml from *B. braunii* at different DDM concentrations.

An intact chloroplast isolation was performed on a 40/80% Percoll gradient to investigate the structure of thylakoid membranes. The samples prepared for scanning electron microscopy (SEM) were washed, resuspended in water, and then lyophilized. The following SEM images correspond to the loss in structure and organization of the solubilized thylakoid membrane isolated from chloroplasts and

the particles found in them (Fig. 3.2). Upon solubilization and a decrease in the organization, large spherical granules, possibly thylakoid plexus, alongside globules of distinct sizes emerge and eventually gather together [143].

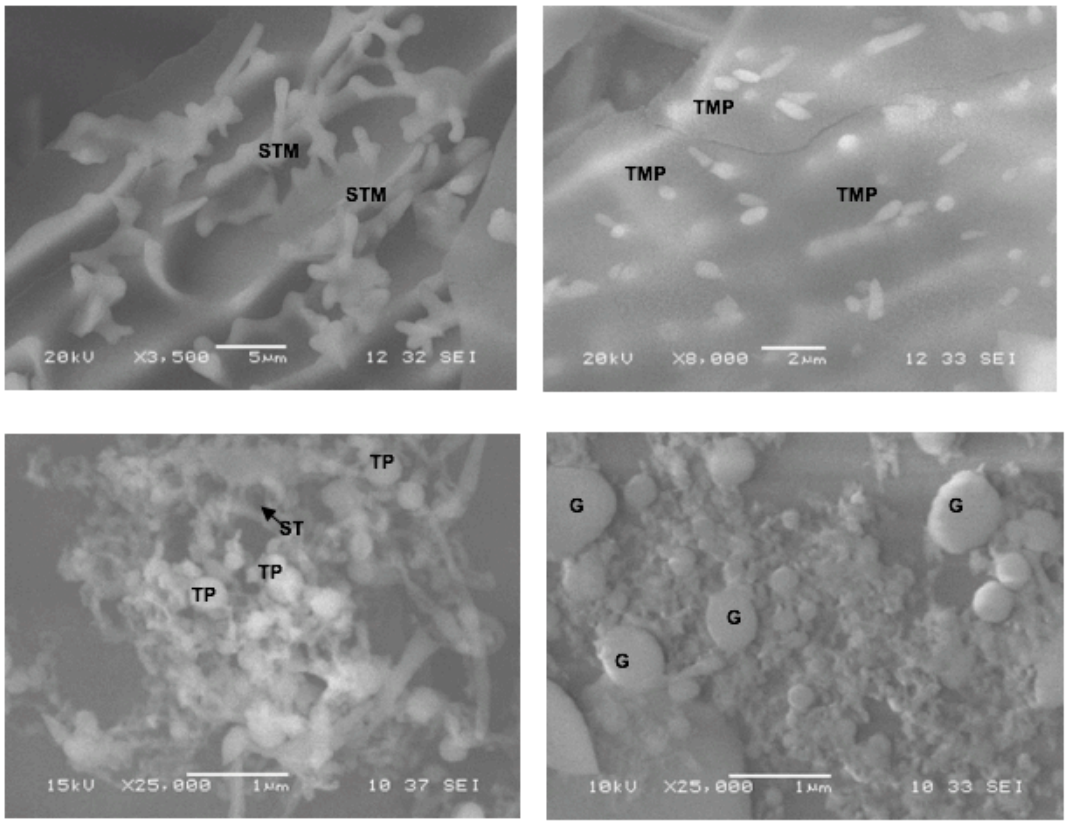

Figure 3.2 Scanning electron micrographs of *B. braunii* chloroplasts isolated by centrifugation through a 40/80% Percoll gradient, where the solubilized stroma thylakoid membrane (STM), transmembrane particles (TMP), thylakoid plexus (TP), and stroma thylakoids (ST) are apparent. Thylakoid spherical globules appear (G). Scale bars, 5 µm, 2 µm, and 1 µm.

3.3.2 PSI reaction center and PSI-LHCI complex purification and spectroscopic characterization

B. braunii PSI-LHCI was purified by loading the DDM-solubilized STM onto a 0.1-1.5 M discontinuous sucrose density gradient. Figure 3.3 (A) presents the two distinct sucrose density gradient bands obtained, with the lowermost green band corresponding to a PSI-rich fraction. The freshly purified fraction was pooled and concentrated, and scanned as observed in Fig. 3.3 (B) to obtain the expected absorption spectrum at room temperature of PSI-LHCI supercomplex, with a maximum peak of 679 nm [55,144].

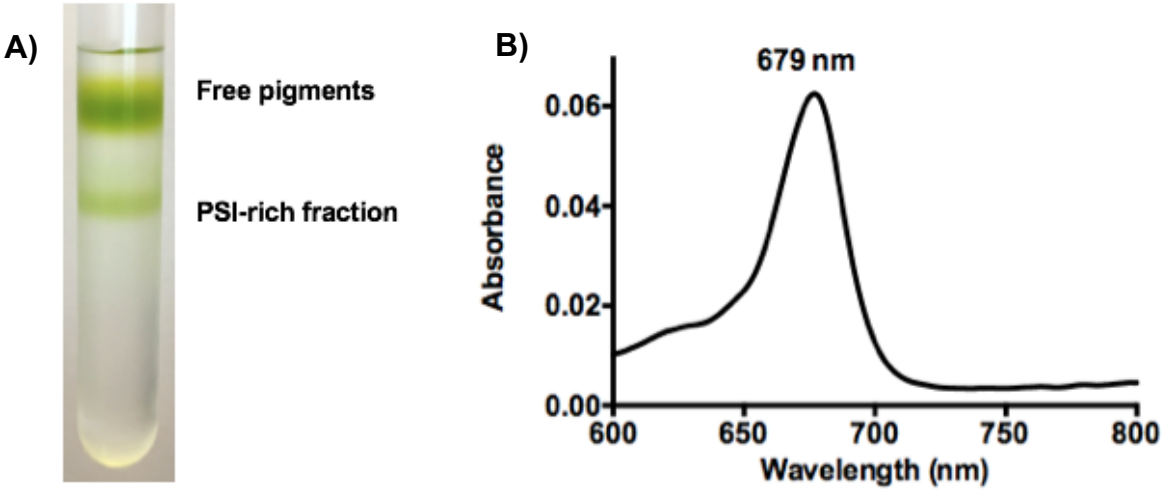

Figure 3.3 Sucrose gradient separation of *B. braunii* thylakoid membranes. The upper band consists of free pigments and unbound proteins, and the lower green band corresponds to the PSI-rich fraction (A). Room temperature absorption spectrum of (0.1-1.5 M) sucrose gradient PSI-LHCI complex fraction (B).

Alternatively, to purify the PSI-RC core complex, FPLC anion exchange chromatography was employed (Fig. 3.4). The PSI-RC fraction eluted after the extraction of free pigments and loosely bound proteins at a concentration of 50 mM $MgSO_4$ and exhibited a maximum absorption peak (1) of 677 nm characteristic of the Chl *a* of the PSI reaction center [144–147]. The second peak (2) detected obtained a maximum absorbance of 673 nm, and in accordance with the literature, results are observed for PSII [148,149]. These two purification processes allowed us to obtain the PSI-LHCI complex and PSI-RC of *B. braunii*.

A)

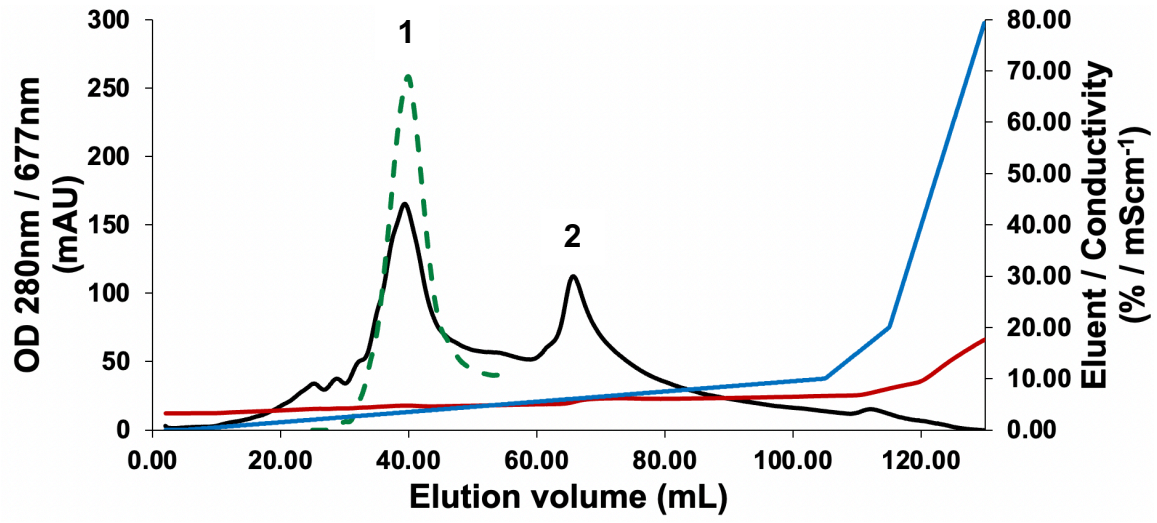

B)

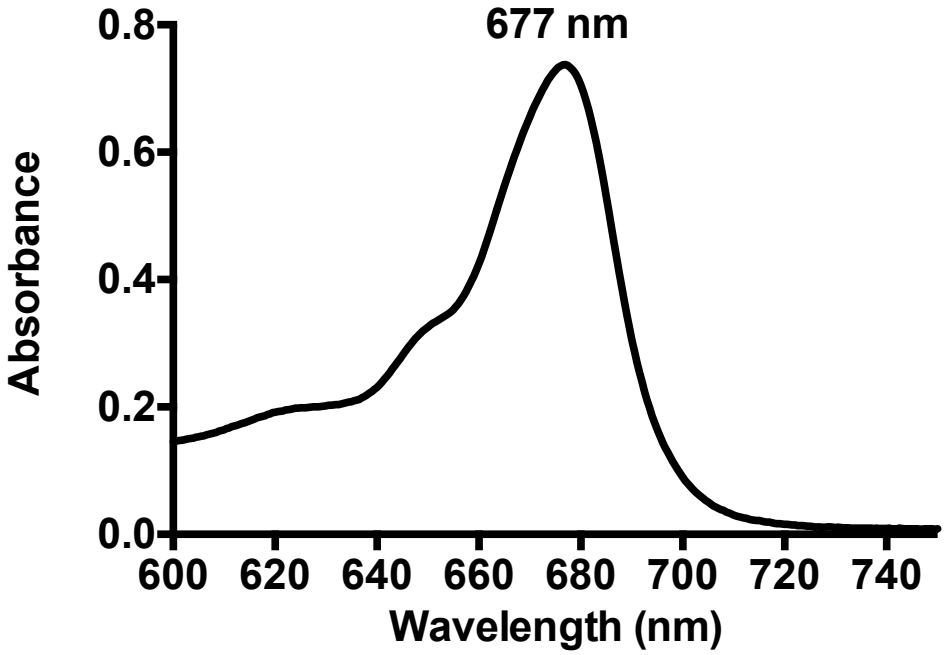

Figure 3.4 Elution profile at 280 nm (solid line) and 677 nm (dotted line) of the purified PSI-RC in elution buffer A with 0.03% (w/v) DDM at a flow rate of 1 ml/min. Purification was performed by anion exchange chromatography on a HiTrap Capto Q column of the crude extract of *B. braunii* thylakoids (A). Room temperature absorption spectrum of FPLC purified PSI-RC eluted with 0.5 M $MgSO_4$ (B).

3.3.3 77 K fluorescence emission measurements

The low temperature (77 K) fluorescence emission spectra of *B. braunii* cells, thylakoids, and PSI-LHCI from 0.1-1.5 M sucrose and 5-30 % glycerol gradient fractions were analyzed as discussed below. In Fig. 3.5 (A), *B. braunii* cells show a broad band at ~715 nm. In contrast, thylakoids show a narrow maximum peak at ~677 nm, suggesting light-harvesting antenna complexes dissociate from photosystems after thylakoid membrane solubilization with mild non-ionic detergents such as DDM, and this disconnection contributes to the fluorescence peaks obtained. *B. braunii* thylakoids and cells sample results are an excellent example of the masking of photosystems by light-harvesting complexes. The high emission fluorescence detected at ~677 nm is due to the detachment of LHCI from PSI and low stability of the PSI-LHCI complex after cell disruption and thylakoid membrane preparation and solubilization in the presence of 0.03% DDM, otherwise, if the photosystems remain connected with the LHC antenna this fluorescence emission peak is absent, as seen in the control (*B. braunii* cells) [150]. The prominent peak at ~677 nm corresponds to disconnected LHCI that, upon solubilization and its inability to effectively transfer its excitation energy to PSI, exhibits a blue-shift spectrum at that wavelength [144,150]. The 77K emission maxima at ~715 nm are characteristically observed in PSI [151]. Both peaks are observed for PSI-LHCI sucrose and glycerol gradient fractions (Chl concentration); however, as explained previously, in *B. braunii* cells, only one broad band is present. At 77 K temperatures, photosynthetic reactions cease, and valuable information regarding the organization of the photosynthetic apparatus, such as

the connection of photosystems with light-harvesting complexes, as reflected on the intensity and fluorescence peaks observed, can be obtained [152]. Overall, PSI emerges as the main contributor in the sucrose and glycerol gradient fractions spectra.

A)

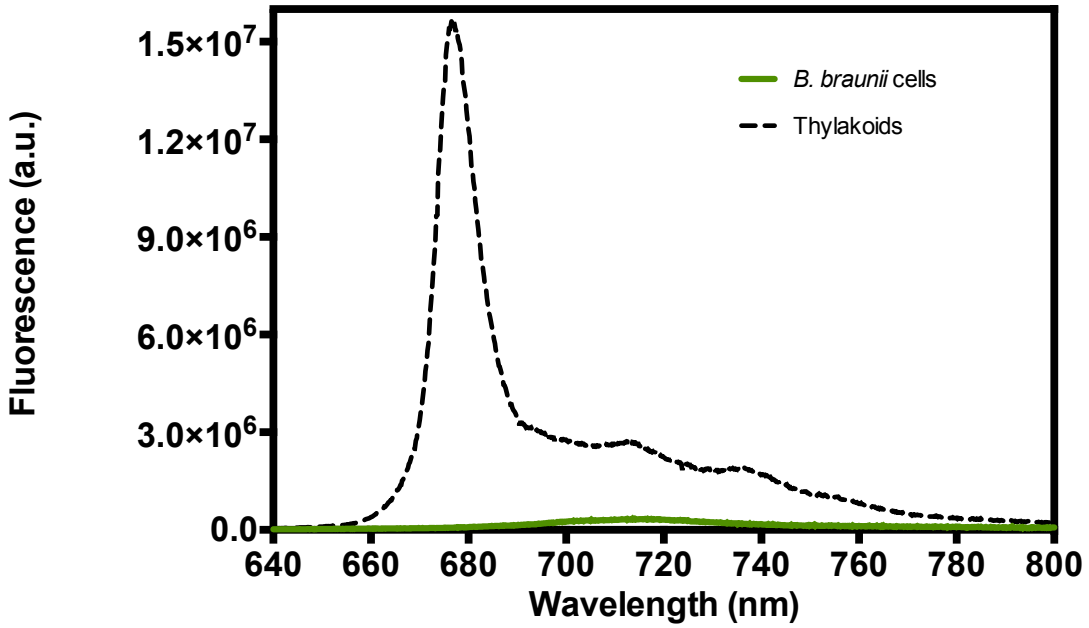

B)

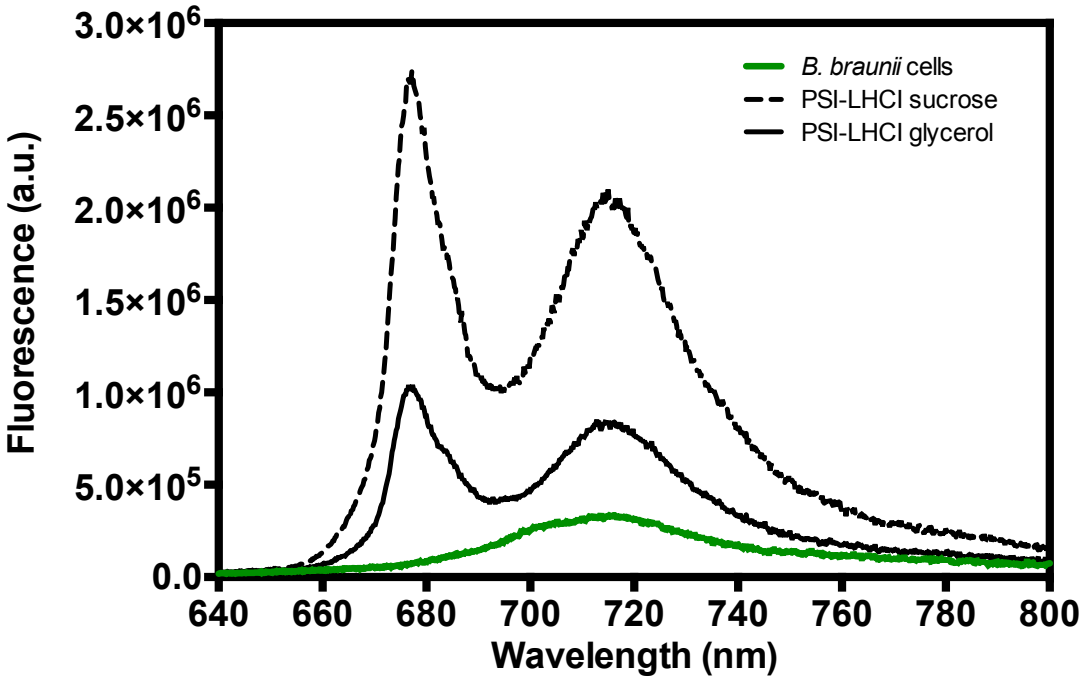

Figure 3.5 The 77K fluorescence emission spectra of thylakoids and *B. braunii* cells (A). PSI-LHCI 0.1-1.5 M sucrose gradient fraction (PSI-LHCI sucrose), 5-30 % glycerol gradient fraction (PSI-LHCI glycerol), and *B. braunii* cells (B). The excitation wavelength was 436 nm.

3.3.4 Circular Dichroism Analysis

In Fig. 3.6, visible CD spectroscopy in the red region revealed the characteristic pigment-pigment and pigment-protein organization of *B. braunii* PSI core complex with their antenna system LHCI (PSI-LHCI) and thylakoids, in agreement with the literature [42]. The longer wavelength positive peak at 668 nm and negative peak at 683 nm corresponds to chlorophyll dimers resulting from the excitonic interplay of Chl *a* in PSI-LHCI supercomplexes, whereas the negative peak at 648 nm is attributed to Chl *b* [153–155]. From the Soret region analysis, the PSI-LHCI visible spectrum showed a positive peak at 444 nm originating from Chl *a*, and three negative peaks at 460 nm and 473 nm, 490 nm prominently observed in thylakoids due to Chl *b* and arising from LHCII, respectively [153,155–157]. Although similar, the CD spectra of PSI-LHCI and *B. braunii* thylakoid presented a slight shift and peaks with somewhat different intensities as explained by the difference in pigments contribution and content from the samples (Table 3.1). These results, as comparably reported in the Qy region of the CD spectrum of PSI-LHCI in the green alga *Chlamydomonas reinhardtii* (*C. reinhardtii*), validated the contribution of LHCI in the sucrose gradient purified PSI and confirmed the absence of any significant contribution from LHCII or PSII [158].

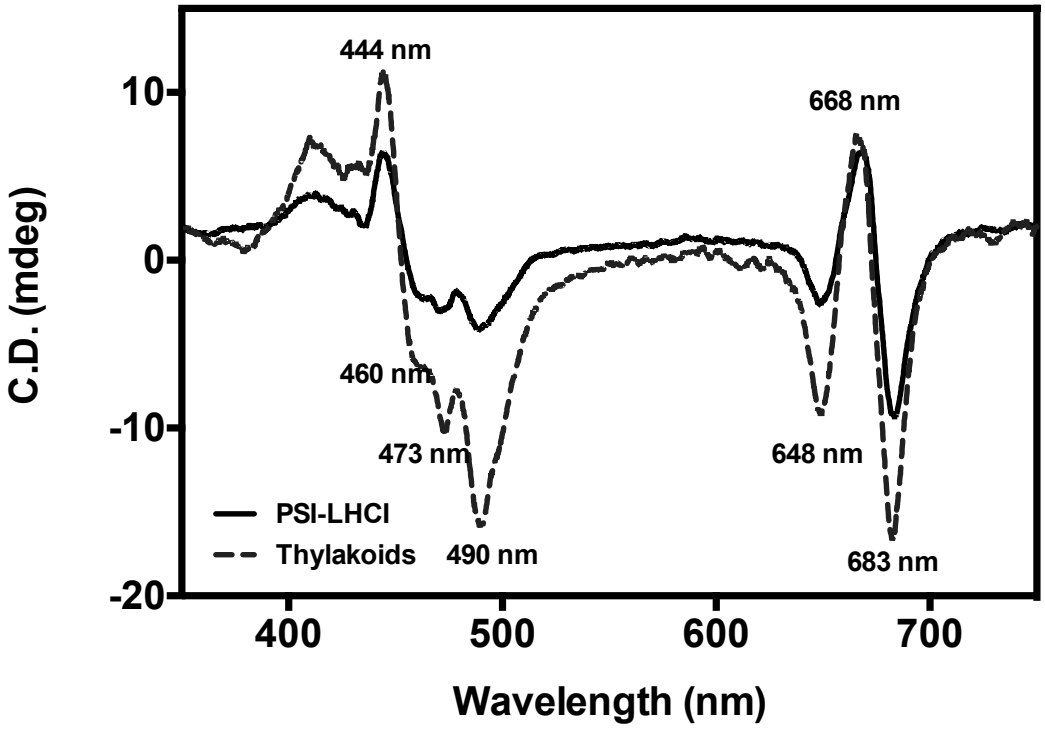

Figure 3.6 Visible CD spectra of purified PSI-LHCI complex and thylakoids measured in a 10 mm quartz cuvette, at a scanning speed of 50 nm/min, a bandwidth of 1 nm, and 25 ^{o}C. Sample concentration was adjusted to 0.4 mg/ml Chl and spectra normalized at the maximum of the Qy region.

3.3.5 Pigment composition

In Table 3.1, the analysis of the pigment content of *B. braunii* cells, thylakoid membrane, and PSI-LHCI complex revealed significant differences amongst them. A strong predominance of Chl *a* is observed in all samples, particularly for PSI-LHCI with (1.50 µg/ml) compared to Chl *b* (0.45 µg/ml).For PSI-LHCI, the Chl *a*/*b*

ratio obtained was 3.4, a much lower value if compared to higher plants such as *Arabidopsis thaliana* (9.7) and the ratio observed in the green microalga *C. reinhardtii* (4.4) [55,159]. A possible increase in abundance in the peripheral pigment antenna system may contribute to these results [160]. The purification treatment influenced the spectroscopic features of PSI-LHCI. Compared to the preparation by glycerol gradient centrifugation, the sucrose fraction displayed the characteristic absorption spectra, fluorescence emission, and CD signals validating PSI-LHCI identity and was subsequently selected as the main purification method.

Table 3.1 Pigment content and yield of *B. braunii* cells, thylakoid membrane, and PSI-LHCI complex extracted in 90% methanol.

Parameter	***Cells***	***Thylakoid Membrane***	***PSI-LHCI***
Carotenoids (µg/ml)	2.1 ± 0.4	0.28 ± 0.02	0.31 ± 0.01
Chl* a *(µg/ml)	1.6 ± 0.5	1.02 ± 0.03	1.50 ± 0.01
Chl* b *(µg/ml)	0.8 ± 0.3	0.53 ± 0.09	0.45 ± 0.03
Chl* a /b *ratio (w/w)	1.93± 0.06	2.0 ± 0.3	3.4 ± 0.2
Total Chl (µg/ml)	2.4 ± 0.8	1.6 ± 0.1	1.94 ± 0.04

[1] Average values are presented as means of two independent experiments ± SD.

3.3.6 PSI-LHCI polypeptide composition by SDS-PAGE

SDS-PAGE evaluated the polypeptide composition of the PSI-LHCI complex obtained from the 0.1-1.5 M sucrose gradient preparation. As observed in Fig. 3.7, our results indicate the presence of six bands, four of them being small subunits detected in the region of 9-30 kDa. A diffuse band was detected with an apparent molecular weight of ~62 kDa corresponding to PSI reaction center core subunits; Photosystem I P700 chlorophyll *a* apoprotein A1 (PsaA) and Photosystem I P700 chlorophyll *a* apoprotein A2 (PsaB), validated quantitatively by LC-MS/MS for the identification of *B. braunii* PSI-LHCI proteins (Table 3.2). The bands visualized in the 20-30 kDa range were assigned to the LHC antenna and PSI stromal subunits PsaD and PsaF. In contrast, those that appear around 10 kDa arise from small PSI subunits, such as Photosystem I iron-sulfur center subunit VII, psaC [55,161]. The sequencing analysis findings presented in Table 3.2 provide the peptide sequence where the proteins identified were filtered, and all high confidence matches closely related *B. braunii* races. Our results indicate that PSI-LHCI was present in the sucrose gradient purified fraction, further characterized by BN-PAGE and 2D native/SDS-PAGE.

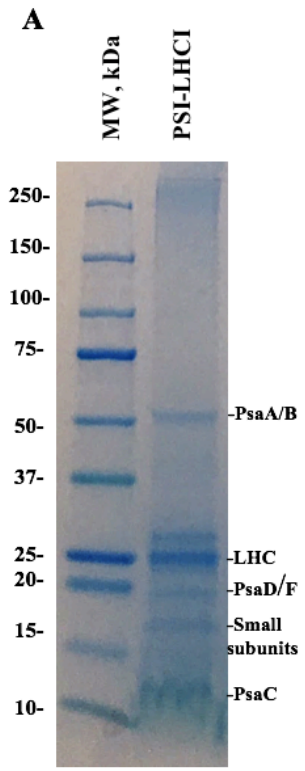

B

Table 3.2. Polypeptide profile of 0.1-1.5 M sucrose gradient purified PSI-LHCI complex from *B. braunii*

No.	Protein identification	Accession number	Gene	De novo sequence protein fragment	Total score
1	Photosystem I P700 chlorophyll a apoprotein A1	A0A097KQ63	psaA	DYDPTNNYNNLLDR ALSITQGR FPCDGPGR VAPAIQPR LLDAGIDPK	49.90
2	Photosystem I P700 chlorophyll a apoprotein A2	A0A097KQ46	psaB	DFGYSFPCDGPGR	8.56
3	Photosystem I iron-sulfur center	A0A097KQ83	psaC	IYDTCIGCTQCVR VYLGAETTR	16.28
4	ATP synthase subunit beta, chloroplastic	A0A097KQ64	atpB	VALVYGQMNEPPGAR VALVYGQMNEPPGAR TVLIMELINNIAK VVDLLAPYR IGLFGGAGVGK LSIFETGIK	61.09
5	ATP synthase subunit alpha, chloroplastic	A0A097KQ55	atpA	TAVAIDTILNQK ELIIGDRQTGK ELIIGDR	24.99
6	ATP synthase subunit alpha	A0A0U2F033	atp1	ELIIGDRQTGK AVDSLVPIGR ELIIGDR STVAQLVK VLDTLGQPIDGK	22.08
7	Cytochrome f	A0A097KQ58	petA	VQLAEMNF	2.21

Figure 3.7 Polypeptide composition of *B. braunii* PSI-LHCI (1.0 mg/mL). Electrophoresis was performed on a 4-20% polyacrylamide gel. The gel was Coomassie blue-stained (A). Polypeptide composition of *B. braunii* PSI-LHCI complex. Proteins were identified by LC-MS/MS (B).

3.3.7 Analysis of PSI-LHCI by BN-PAGE and 2D-PAGE

Figure 3.8 depicts the BN-PAGE of *B. braunii* thylakoids and PSI-LHCI (0.7 mg/ml Chl *a*). Mass estimation was achieved using NativeMarkTM unstained protein standard (~20 to 1,200 kDa) to generate a molecular weight (MW) standard curve of the log MW versus the migration distance of the protein through the gel divided by the migration distance of the dye front (R_f) [162]. PSI-LHCI complexes were resolved and qualitatively visualized in a BN-PAGE gel where several bands were identified and deduced according to previous reports. The high molecular values estimated were 669 kDa appointed to supercomplexes (SC), ~ 600 kDa to PSI-LHCI, 481 kDa to PSI, 324-303 kDa to ATPase, 250 kDa to dimer Cyt b6/f, 121 kDa to monomer Cyt b6/f and 93 kDa to LHCII subunits [55,141]. Two-dimensional native/ SDS-PAGE was accomplished in a gradient 4-12% Bis-Tris gel in MES running buffer at 150 V for 1 h with the excised PSI-LHCI complex BN-PAGE gel lane obtained previously that underwent reduction, alkylation, and quenching as indicated in the manufacturer's protocol. A prestained protein standard was used to estimate PSI-LHCI and co-eluting components (~3.5 to 260 kDa). Second dimension 2D native/SDS-PAGE polypeptide spots detected indicated a high abundance of PSI-LHCI complex components and subunits as observed in previous reports providing an assessment of the polypeptide composition of our preparation [140,163]. Although we notice a small contribution

for LHCII, a mobile antenna, judging from our 77K fluorescence assay, it is deemed not a major contributor [150,151]. To the best of our knowledge, this is the first time such an exhaustive characterization study on *B. braunii* PSI-LHCO has been conducted.

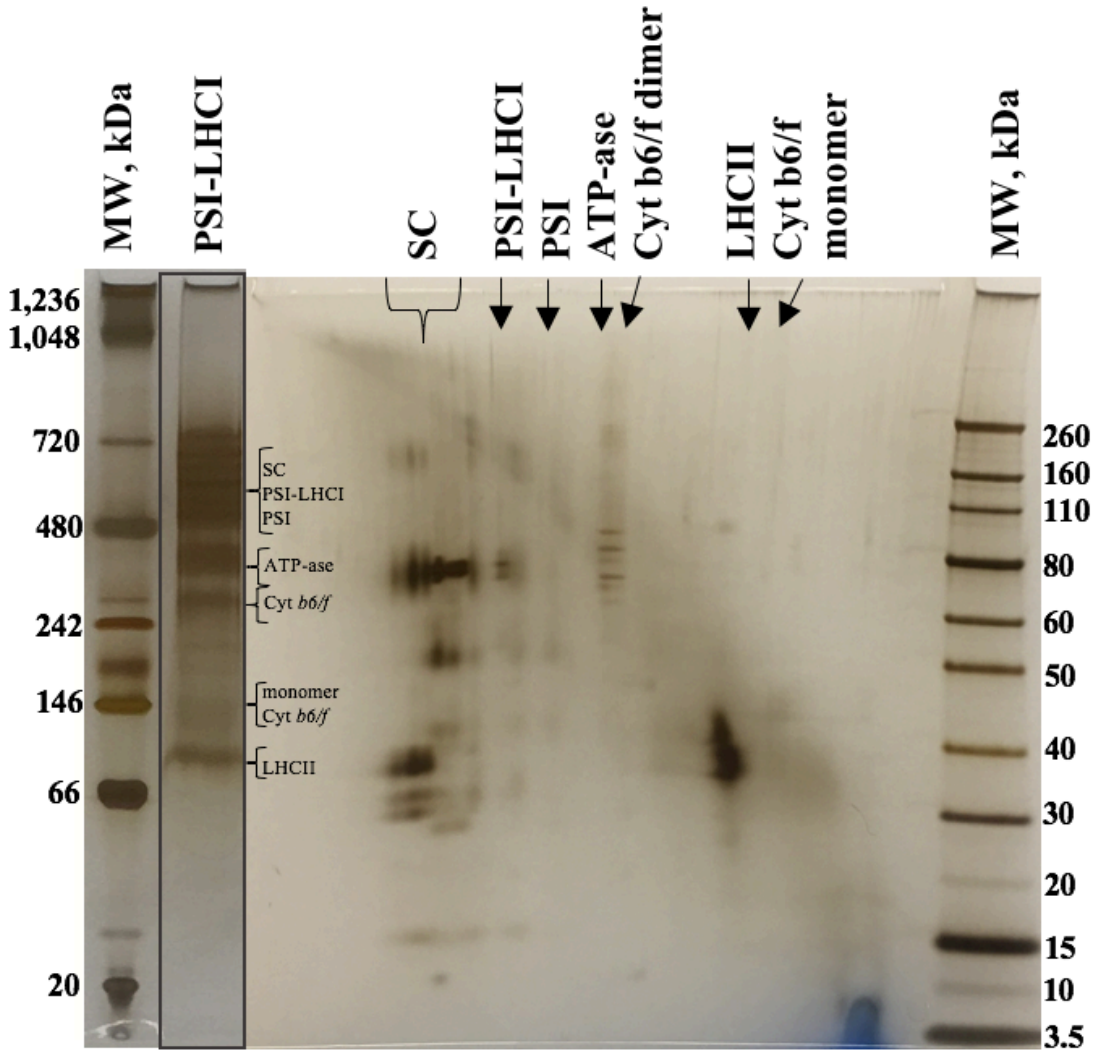

Figure 3.8 BN-PAGE separation of purified PSI-LHCI complexes and thylakoids from *B. braunii* at a concentration of 0.7 mg/ml Chl. The selected lane was excised and applied to a two-dimensional SDS-PAGE gel to separate PSI-LHCI polypeptides and co-eluting complexes.

3.4 Conclusions

In summary, two purification protocols that generate PSI-RC and PSI-LHCI from *Botryococcus braunii* UTEX2441 have been established and studied in detail. We found that the FPLC system with the HiTrap Capto Q prepacked strong anion exchanger column yields a PSI core preparation, excluding contamination from other protein complexes. At the same time, a discontinuous sucrose density gradient ultracentrifugation process produced a PSI-LHCI complex. Characterization results of both purification protocols were evaluated by absorbance and fluorescence spectroscopic studies, CD measurements, pigment, and polypeptide composition analysis. *B. braunii* is a green microalga highly studied due to its oil generation and use in the biofuel industry. However, its biomedical application is currently underway, setting the base for broadening PSI's relevance and use. This dissertation highlights the PSI core complex and surrounding LHCI antenna system organization, furthering the understanding and studies of this organism's pigment-protein complex.

Botryococcus braunii Photosystem I induce ROS-dependent decrease in cell viability by necrosis and autophagy pathways

4.1 Summary

In green microalgae, such as *B. braunii*, the thylakoid membrane, principally PSI, obtained following Specific Aim 1 descriptions, is the main contributor to ROS's overall production. ROS generation in TM and PSI, specifically $^1O_2$, was monitored spectrophotometrically using the p-nitrosodimethylaniline, RNO assay, at 440 nm, which produced RNO dye bleaching upon singlet oxygen generation.

Taking into consideration that *B. braunii* TM and PSI generate $^1O_2$, we determined Chlorophyll *a* OJIP (O = origin and equivalent to F_o, J and I = intermediate steps, P = peak and equivalent to F_m at saturating light conditions) fluorescence induction transients, after saturating light conditions and the addition of antioxidants, ROS scavengers, and photosynthesis inhibitors, used in photosynthesis research to study photosynthetic efficiency, and pigments photoprotective roles [164]. We performed *in vitro* cell viability studies to investigate the cell death mechanisms, particularly in the triple-negative breast cancer cell line MDA-MB-231. A concentration-dependent reduction in cell viability was observed after incubation for 6, 12, and 24 h using different PSI-LHCI concentrations (6.25, 12.5, 25, and 50 µg/ml). Fluorescence confocal microscopy studies, particularly Z-series, examined the intracellular localization of PSI-LHCI,

which after 24 h of treatment, appeared to be present in the cytoplasm. After incubation with PSI-LHCI, total ROS production and superoxide detection in live MDA-MB-231 cells was determined by confocal microscopy. We found that PSI-LHCI under serum starvation conditions induced oxidative stress, increased ROS levels and superoxide production, and reduced mitochondrial membrane potential. An increment in the autophagy marker dye's fluorescence accumulated in the autophagosomes confirmed PSI-LHCI-induced cell death via autophagy. DNA content in dead cells was examined; analyses with Annexin V/PI only exhibited a red concentrated cell nucleus suggesting necrotic cell staining, whereas Annexin V did not show any typical early apoptosis green fluorescence signal. Our results indicate that MDA-MB-231 cells undergo autophagy and necrosis after treatment with PSI-LHCI for 24 h.

4.2 Introduction

Breast cancer is the most often diagnosed cancer among women worldwide and the second leading cause of death after lung cancer [165]. Up to 80% of breast cancer cases express hormone receptors such as ER, PR, and ERBB2 or HER2/neu; the rest of the breast cancer diagnosed fall into the triple receptor-negative category, characterized by the lack of expression of these receptor proteins [166]. Early and late-stage breast cancer therapeutic options rely on hormone therapy targeting nuclear or surface receptors with pharmacological agents such as tamoxifen and trastuzumab [166]. TNBC is an aggressive breast cancer subtype with a poor prognosis that remains resistant to existing targeted

hormone treatments relying predominantly on chemotherapy as standard treatment [167]. Current TNBC pharmacological strategies involve the anti-programmed death receptor 1 drug, pembrolizumab, combined with nab-paclitaxel, paclitaxel, or gemcitabine/carboplatin chemotherapeutic agents, reporting statistical significance [122]. As one of the 27 human breast cancer cell lines classified as TNBC most cited in the literature, MDA-MB-231, isolated in 1970, is one of the most commonly studied cell lines and the central topic in this research study [167]. We investigated a possible anticancer treatment using a natural source reactive oxygen species (ROS) generator.

In green microalgae, such as *B. braunii*, PSI, a pigment-protein complex located in the thylakoid membrane involved in photosynthesis, is the leading production site of ROS [168]. A surplus of ROS produces irreversible oxidative damage by reacting with proteins, lipids, and nucleic acids, thus activating signaling pathways that promote cell death [90]. Under stress conditions, ROS and autophagy studies in photosynthetic organisms have been predominantly associated with cell death. Autophagy acts as a defense mechanism mediating the removal of oxidatively damaged molecules and ROS-generating organelles by a nonselective engulfing process by the autophagosome and ultimate delivery to the lysosome for degradation [90,169]. In mammalian cells, ROS selectively target malignant cells and activate autophagy; accordingly, an accumulation of ROS in the mitochondria makes them a potential target for degradation [170,171]. Cancer cells undergo an increase in the lysosomal membrane permeabilization process

promoting lipid peroxidation, making them more susceptible to ROS-mediated cell death via apoptosis, autophagy, and necrosis pathways [172].

In this work, we report for the first time the cytotoxic impact of oxidative stress generated by the green microalga *B. braunii* PSI-LHCI in triple-negative human breast cancer cells (MDA-MB-231) through a ROS-dependent decrease in cell viability, thus elucidating a lysosome-mediated type of cell death via necrosis and autophagic pathways.

4.3 Results and Discussion

4.3.1 Chlorophyll Fluorescence Induction Studies

Light provides the energy needed for the photosynthesis process, but exposure to intense light conditions can also be toxic to the photosynthetic apparatus and damage it [173]. Diuron (3-(3,4-dichlorophenyl)-1,1-dimethylurea or DCMU), a widely used phenylurea herbicide known to inhibit the photosynthetic electron transport between PSII and PSI by binding specifically to the Q_B binding pocket at the PSII D1 protein, thereby blocking the electron transfer between the plastoquinone binding sites of Q_A and Q_B on the reducing side of PSII, has been shown to photodestroy chlorophyll and carotenoid pigments [174–176]. Inhibiting electron transport overwhelms the triplet chlorophyll-to-carotenoid dissipation mechanism for excessive absorbed light energy that generally protects the chloroplast, thus inducing pigments phytotoxicity [177,178].

Incubation of 50 µg/mL *B. braunii* UTEX2441 cells with 20 µM DCMU was performed to investigate the photoprotective effect of pigments, in particular, Chl

a, against oxidative stress after exposure of *B. braunii* cells to DCMU in aqueous solution after illuminating them with intense light excitation conditions (450 nm light of 3000 μmol photons m^{-2} s^{-1}), as studies with DCMU bring awareness of the relationship among chlorophyll fluorescence and the light-dependent reactions of photosynthesis [179].

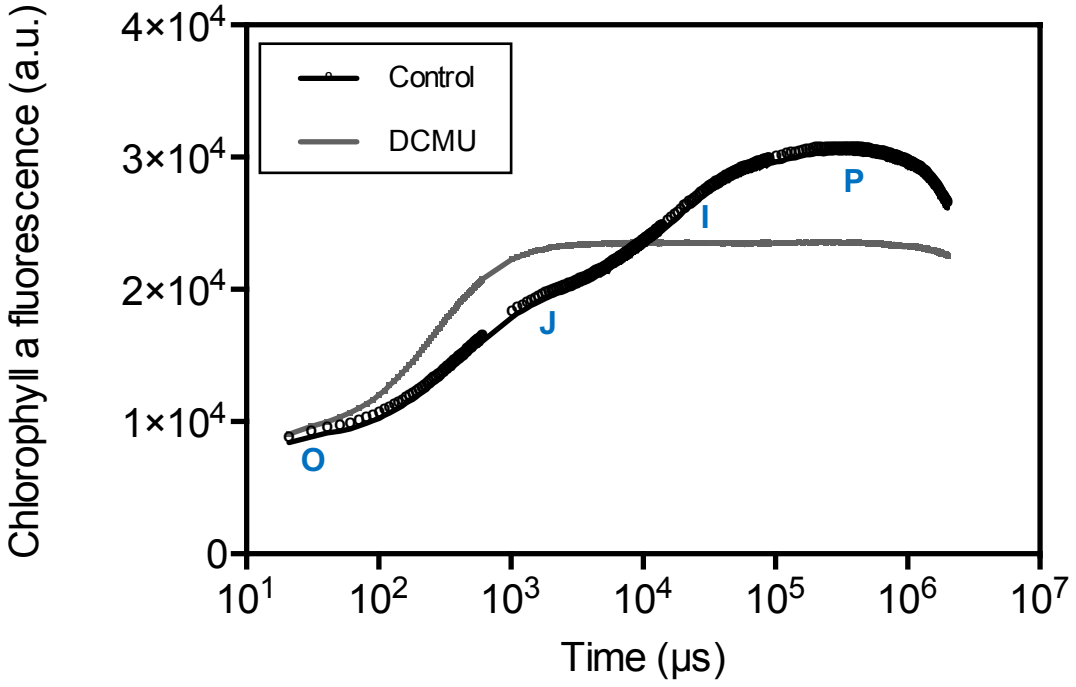

Figure 4.1 Chlorophyll *a* fluorescence transient OJIP for *B. braunii* cells after strong light excitation (3000 μmol photons m^{-2} s^{-1}; λ_{exc} = 450 nm), in the absence (control) or presence of DCMU.

Figure 4.1 displays the inability of Chl *a* to protect against excessive illumination and dissipate its absorbed light energy as observed in the steep initial rise of the fast fluorescent transient, the OJIP curve on a logarithmic time scale of the dark-adapted DCMU-treated vs. the control samples. Dark adaptation of the samples for 10 min was crucial to obtain reproducible Chl *a* fluorescence results

consequence of the well-defined photosynthetic apparatus state while avoiding inducing photosynthetic activity [164]. Upon adding 20 μM DCMU, Chl *a* fluorescence progresses quickly, reaching maximum fluorescence without presenting the characteristic J and I inflection points observed in untreated cells, implying full inhibition of electron flow and PSII with an apparent quenching of fluorescence (F_M value) due to an oxidized PQ pool, as similarly reported in the literature [180]. This process is connected to the photosystems, particularly to the reaction centers that get saturated, stimulating an increase in fluorescence intensity.

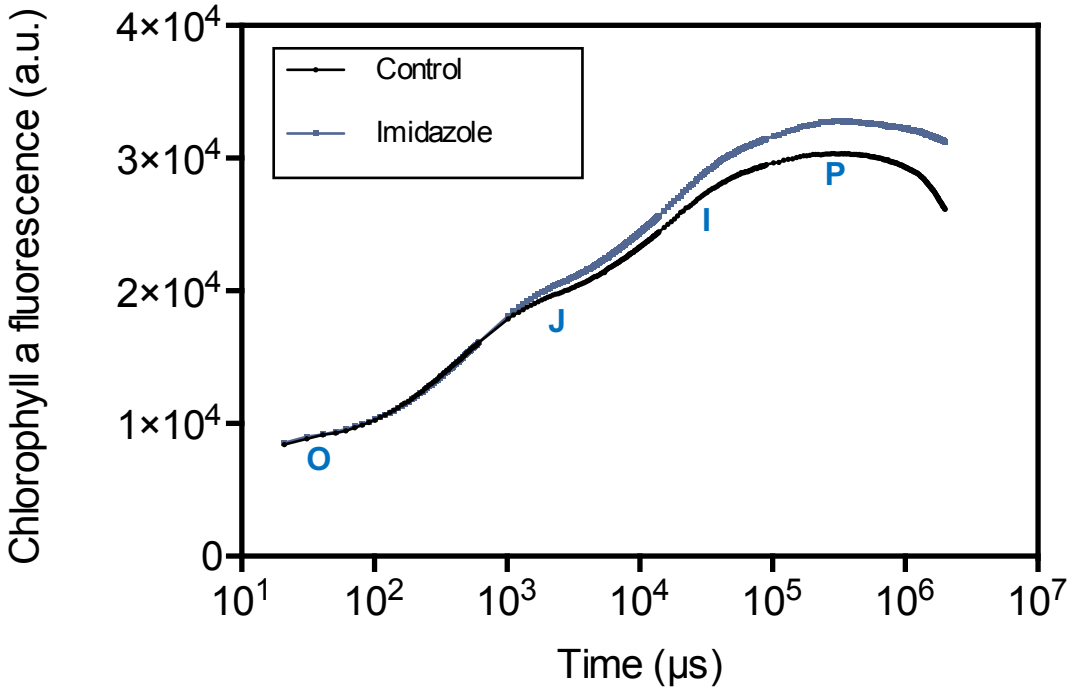

Figure 4.2 Effects of Imidazole on the chlorophyll *a* fluorescence transient OJIP for *B. braunii cells* after strong light excitation (3000 μmol photons m^{-2} s^{-1}; λ_{exc} = 450 nm).

After adding 5 mM imidazole to *B. braunii* cells, we determined that imidazole, a chemical trap used to detect $^1O_2$, confers no photoprotection capacity to Chl *a* against light intensity damage (Figure 4.2). The fluorescence transients observed, plotted on a logarithmic scale, followed the typical OJIP pattern, where the origin (F_O) or initial value of fluorescence appears at 21 μs, the J and I inflection points appear at about 2 ms and 30 ms, respectively, and the peak (F_M) or maximum value under saturating light evidently distinguishable [48]. Focusing on the OJ segment or initial rise kinetics of Chl *a* fluorescence of control samples and the water-soluble compound and $^1O_2$ acceptor imidazole-treated samples, we resolve that the OJ traces appear indistinguishable up until nearly reaching the ~2 ms J inflection point. Moreover, we determined that imidazole offers no protection to pigment molecules against photodamage and oxidative stress caused by high light intensity conditions.

B. braunii cells Chl *a* fluorescence OJIP transients (Fig. 4.3 and Fig. 4.4) were generated after applying exogenous nonenzymatic antioxidants, radical scavengers, and the photosynthetic electron transport inhibitor DCMU. The OJIP fluorescence measurements, a crucial biophysical signal reflecting the time course of photosynthesis, provide insight into the capacity of microalgal cultures to withstand environmental stresses and to which extent the photosynthetic apparatus is damaged [164]. After blue light excitation of 450 nm (Chl *a*) and continuous illumination (3000 μmol photons $m^{-2}s^{-1}$), Alpha-tocopherol, which deactivates photosynthesis derived singlet oxygen, was used and compared to the antioxidant, and singlet oxygen scavenger power of L-glutathione reduced that

scavenges/reduces ROS; also it was compared to L-Ascorbic Acid, a potent ROS scavenger, and Uric Acid which inhibit ROS producing enzymes.

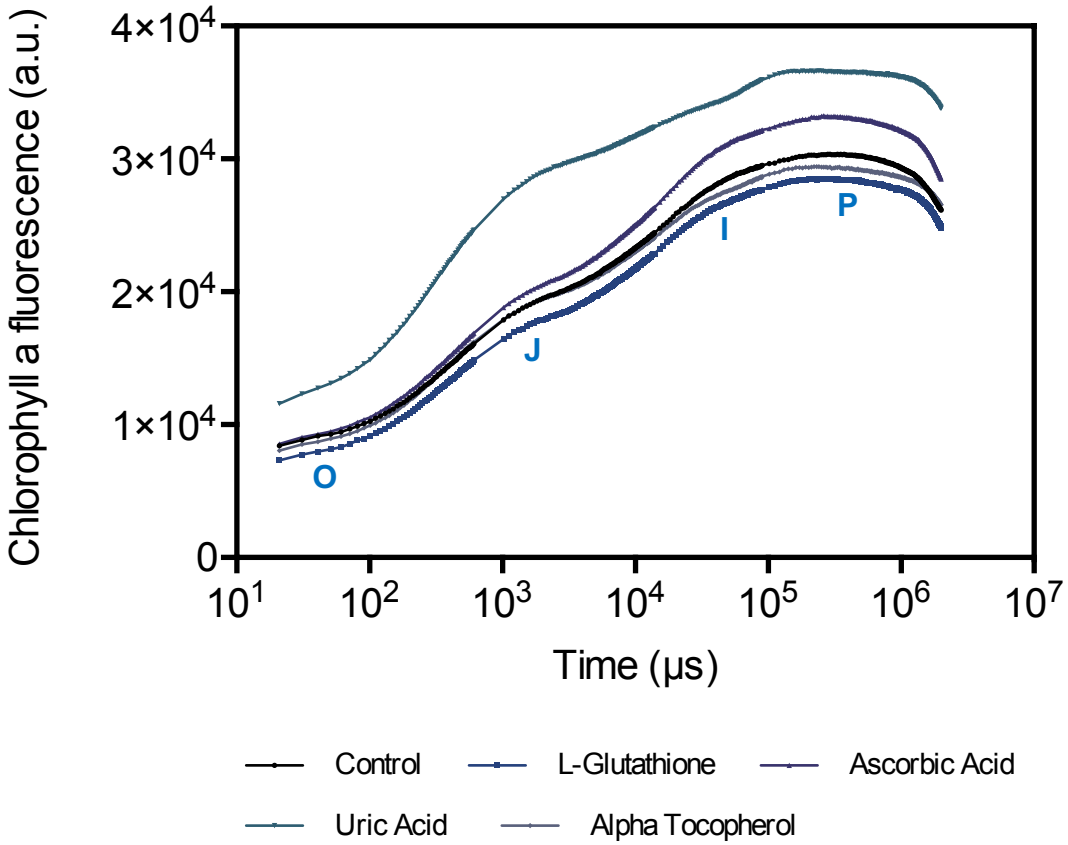

Figure 4.3 Chlorophyll *a* fluorescence transient OJIP for *B. braunii* cells after strong light excitation (3000 µmol photons m^{-2} s^{-1}; λ_{exc} = 450 nm), in the absence (control) or presence of L-glutathione, Ascorbic Acid, Uric Acid and Alpha Tocopherol.

Figure 4.3 illustrates the use of L-glutathione reduced, Ascorbic Acid, Uric Acid, and Alpha-Tocopherol as antioxidants and $^1O_2$ scavengers. An enhanced fluorescence is observed with Uric Acid and Ascorbic Acid, thereby implying the

protection of Chl *a* due to the potent $^1O_2$ scavenging efficiency and enzymatic inhibitory effect of these substances. Figure 4.4 compares the halt of photosynthesis by the effect of the herbicide DCMU, the use of the singlet oxygen chemical trap, imidazole, and the application of antioxidant species as means of offering photoprotection to excited Chls *a*.

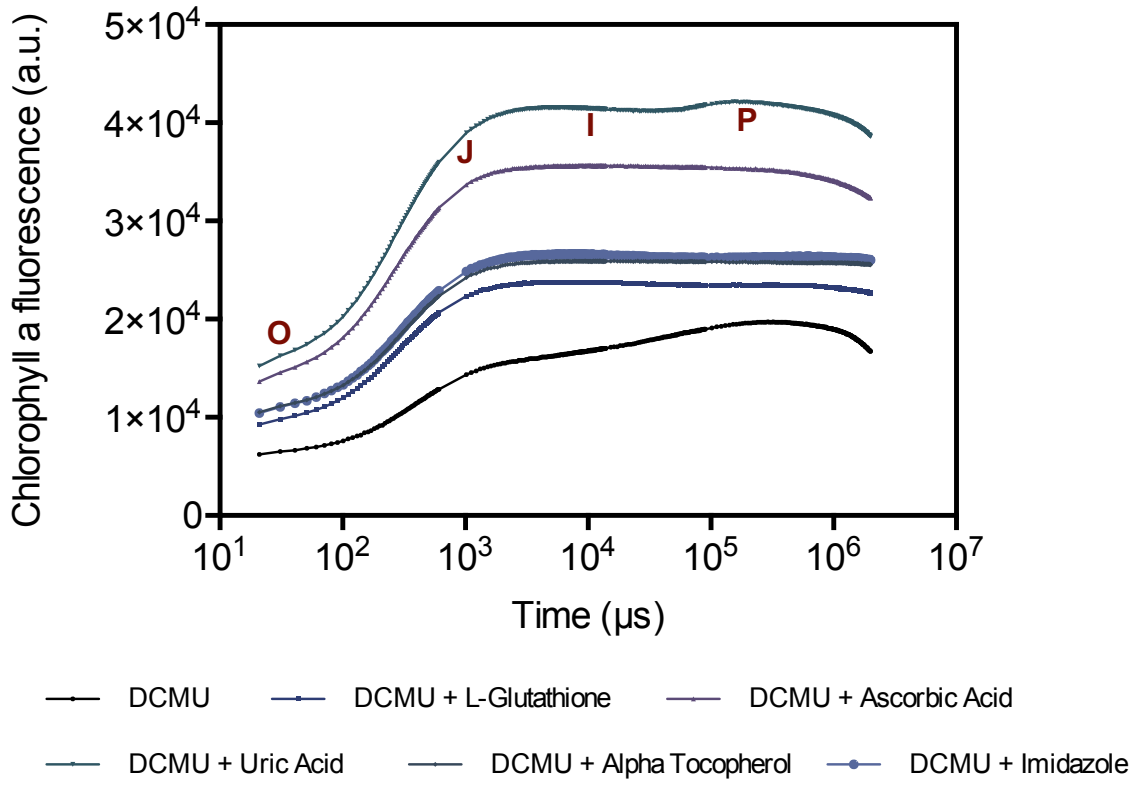

Figure 4.4. Chlorophyll *a* fluorescence transient OJIP for *B. braunii* cells after strong light excitation (3000 µmol photons m^{-2} s^{-1}; λ_{exc} = 450 nm), in the presence of DCMU, and DCMU with L-Glutathione, Ascorbic Acid, Uric Acid, Alpha Tocopherol, and Imidazole.

As seen in Figure 4.3 and Figure 4.4, the increase in Chl fluorescence due to the photoprotection influence of these additives' antioxidant activity and their singlet oxygen scavenger capacity relies on their ability to donate electrons. The redox catalyst action capable of reducing and neutralizing ROS, was first seen occurring in Uric Acid, followed by Ascorbic acid, Alpha-tocopherol, and lastly in L-Glutathione reduced. Similar photoprotection effects were observed in the presence of DCMU, an environmental stressor that halts photosynthesis completely (PSII photosynthetic electron transport).

Artificial electron donors, such as the antioxidant additives, circumvent the DCMU block and damage during illumination by conferring an observable degree of protection against Chl a photodestruction. According to their antioxidant capacity or strength, the OJIP curves of fluorescence induction exhibit a corresponding inclination in the logarithmic scale graph, thus confirming the presence of ROS [177].

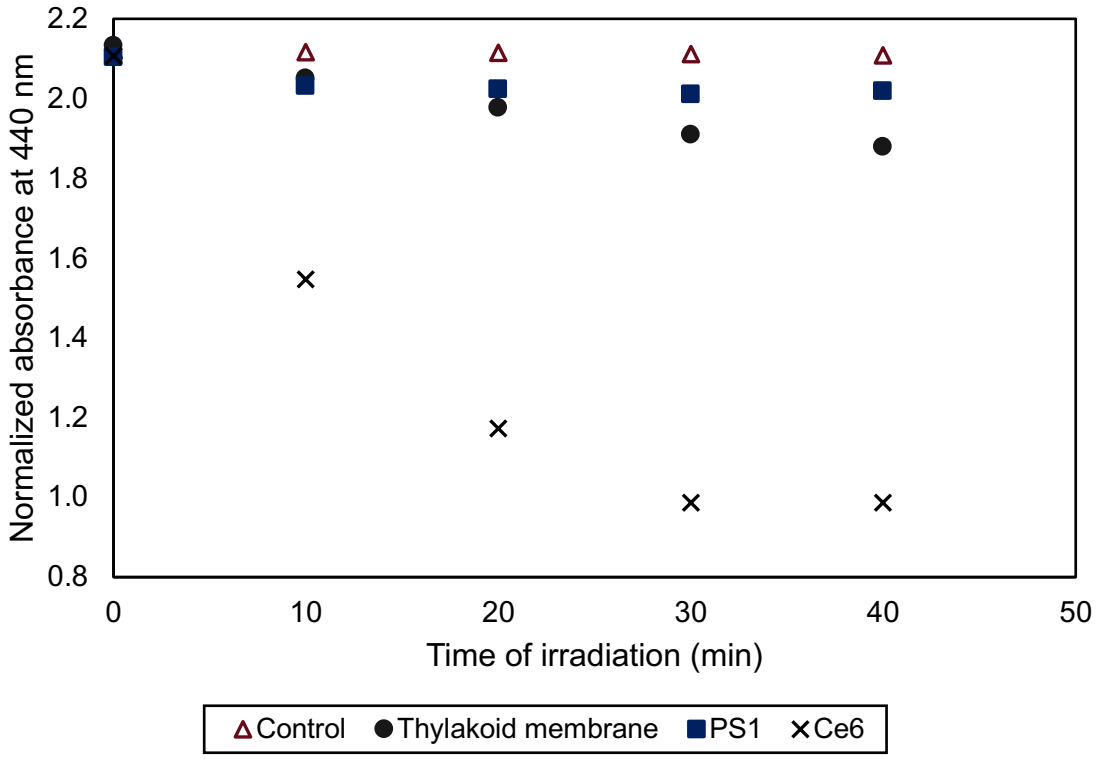

Figure 4.5. The time course of RNO bleaching at 440 nm of *B. braunii* thylakoid membrane and PSI in the presence of imidazole (10 μM) and RNO (50 μM) in phosphate buffer (pH 7.4). Chlorin (Ce6) was used as a singlet oxygen generator.

Singlet-state oxygen is a highly reactive form of ROS, generated as a byproduct of light trapping and energy conversion during photosynthesis. It is responsible for damaging oxygenic photosynthetic microorganisms, particularly the D1 protein, required for the PSII repair system, inhibiting *de novo* protein synthesis, and leading to PSII inactivation [181,182]. The organism under study, *B. braunii*, has naturally producing $^1O_2$ components, such as TM and PSI, which act as light-sensitive molecules called photosensitizers. Photoactivation causes the formation of $^1O_2$, a byproduct of photosynthesis that produces peroxidative

reactions that can cause cell damage and death; thereby, we performed the p-nitrosodimethylaniline bleaching assay.

As shown in Figure 4.5, using RNO as a selective scavenger and imidazole as a $^1O_2$ acceptor, RNO is bleached as followed spectrophotometrically at 440 nm. The $^1O_2$ capture by the imidazole ring results in the formation of a trans-annular peroxide intermediate promoting the bleaching of RNO. This imidazole plus RNO system was used as a sensible assay to measure $^1O_2$ in *B. braunii* TM and PSI aqueous solutions [183]. Exposure occurred to LED light (λ_{max}=660 ± 10 nm) at a distance of 10 cm and a fluence rate of 50 mW/cm^2 for 40 min. Photoactivation triggers the formation of $^1O_2$ with a higher degree in thylakoid membranes than PSI due to the production of $^1O_2$ within the hydrophobic domains of the thylakoid membrane, where Chl *a* is located. In Fig. 4.5, we can observe the generation of $^1O_2$ by the singlet oxygen generator and positive control chlorin e6 (Ce6), untreated cells with no apparent generation of $^1O_2$, and slight bleaching of RNO at 440nm by *B. braunii* TM and PSI. It is essential to mention that intense irradiation damages the photosystems; therefore, a more accurate ROS and superoxide detection assay is required to successfully monitor the generation of reactive oxygen species and not only $^1O_2$.

4.3.2 <u>Phototoxicity Evaluation and Cell Viability Studies</u>

Initially, cell-based screening studies assessed the effect of PSI-LHCI on the HeLa (human cervical adenocarcinoma) cell line. Phototoxicity in HeLa cells was assessed after incubation with PSI-LHCI (3.125, 6.25, 12.5, 25, and 50 µg/ml)

for 24 h, and irradiation with a LED lamp (λ_{max}=660 ± 10 nm) at a distance of 10 cm from the 96-well plate and a fluence rate of 50 mW/cm^2 for 10 min before measurements. Extraction buffer A was added to HeLa cells at the highest concentration tested as a negative control.

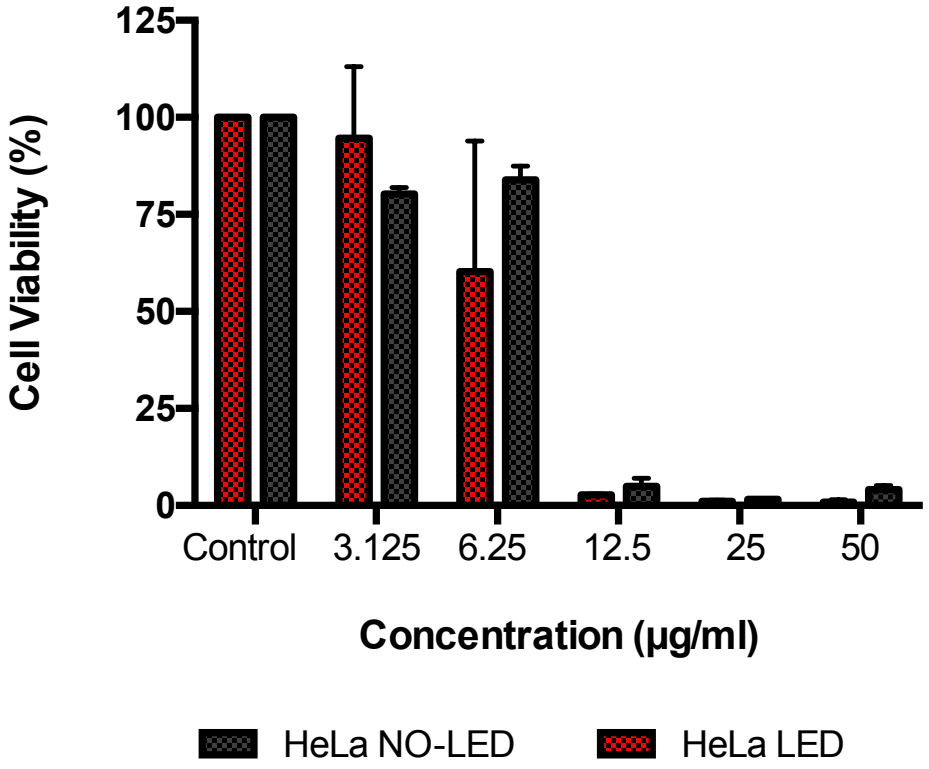

Figure 4.6. Cell viability in HeLa cells. Effect of PSI-LHCI in cell viability following treatment with different concentrations of PSI-LHCI (from 3.125 to 50 µg/ml) in the presence and absence of LED irradiation (λ_{max} =660 ± 10 nm) after 24 h of incubation. Incubation with the extraction buffer A (control) at the highest experimental concentration (50 µg/ml) was included.

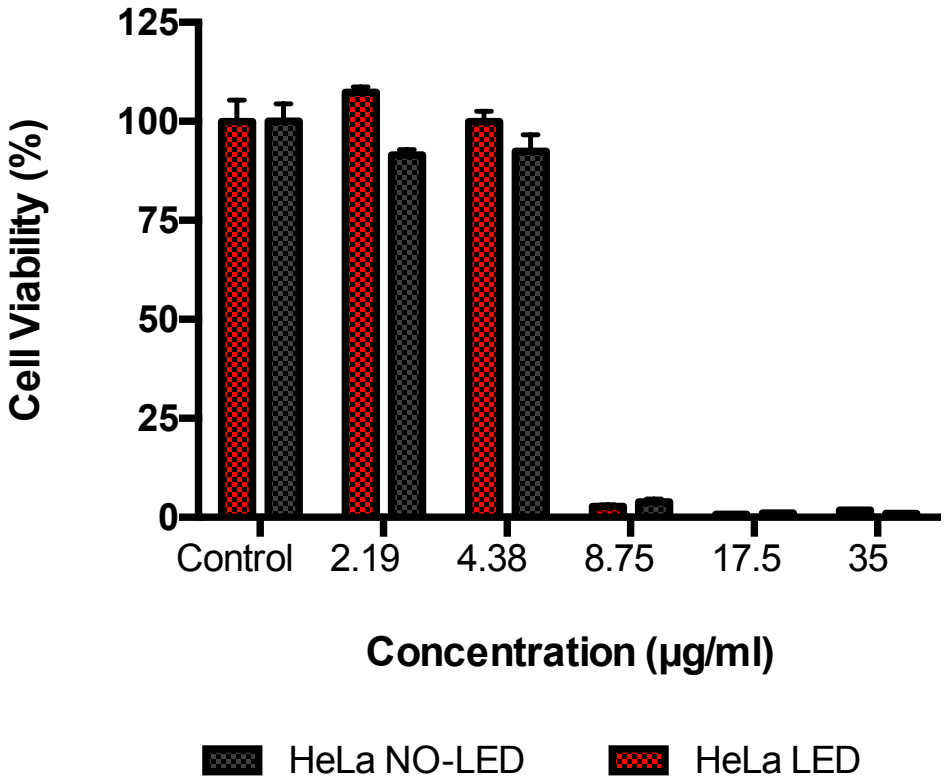

Figure 4.7. Cell viability in HeLa cells. Effect of PSI-LHCI in cell viability following treatment with different concentrations of PSI-LHCI (from 2.19 to 35 µg/ml) in the presence and absence of LED irradiation (λ_{max} =660 ± 10 nm) after 24 h of incubation. Incubation with the extraction buffer A (control) at the highest experimental concentration (35 µg/ml) was included.

A drastic reduction in cell viability was observed, particularly at the 12.5 µg/ml PSI-LHCI concentration (Figure 4.6). Although a decrease in viability was detected, the IC_{50} values calculated with GraphPad Prism 6 for HeLa cells with LED irradiation (IC_{50} =9.628 µg/ml, R^2 = 0.1263) and HeLa cells without LED irradiation (IC_{50} = 9.755 µg/ml, R^2 = 0.05038) obtained R-squared with 10% or 5%

variation within the data. Thus, we examined varying concentrations in the range closer to the value corresponding to the drop in cell viability previously observed in HeLa cells. Consequently, HeLa cells were incubated with PSI-LHCI concentrations (2.19, 4.38, 8.75, 17.5, and 35 µg/ml), and after 24 h, similar results were obtained, particularly at the 8.75 µg/ml PSI-LHCI concentration (Figure 4.7). Once again, HeLa cells irradiated with a LED light source obtained an IC_{50} = 6.101 µg/ml and R^2 = 0.1083. Hela cells minus LED irradiation attained an IC_{50} = 8.207 µg/ml and R^2 = 0.1744, which only explained 10% variability within the data. Regardless of irradiation, cell viability experienced a steep decline to less than 5% in both experiments with at least three experimental replicates. Due to these outcomes, variable IC_{50} results, and poor R-squared values, the HeLa cell line was deemed not the best model for PSI-LHCI toxicity studies.

PSI-LHCI samples treated with irradiation obtained mixed toxicity results; thus, LED radiation was deemed unnecessary to achieve toxic effects. Furthermore, chlorophyll *a* fluorescence induction studies results (Section 4.3.1) support the reasoning behind the discouragement of using light irradiation to generate ROS in cell viability analyses of cancer cell lines incubated with PSI-LHCI as the photosensitizer pigments (e.g., chlorophyll and carotenoids) alongside the proteins within the pigment-protein complexes these are attached to, are also irreversibly photo-oxidatively destroyed [177].

Before selecting the best cancer cell line *in vitro* model system, we assessed the cell viability of HeLa cells after a 24 h treatment with cytochrome c at a range of concentrations from (12.5 - 100 µg/ml) dissolved in the extraction buffer A (50 mM HEPES, pH 7.2; 5 mM $MgCl_2$; 5 mM $CaCl_2$; 20% glycerol; 1X protease inhibitor SIGMAFAST; 1 mM EDTA; 0.03% DDM). We performed this assay to examine if the non-ionic detergent DDM and concentration used had a role in the membrane permeability that allows negatively charged and ROS-producing PSI-LHCI to enter the cell membrane and induce a decrease in cell viability. Cytochrome c is a membrane-impermeable apoptosis-initiating protein and an ideal candidate to test this hypothesis in cancerous cells such as HeLa [184]. From the non-statistically significant results observed in Figure 4.8, in replicate experiments, Cyt c was unable to induce a decrease in cell viability, confirming that the detergent concentration used in the buffer is not a factor that allows membrane-impermeable proteins to be transported across the phospholipid bilayer of the membrane. Therefore, PSI-LHCI must be interacting with the cell membrane via an alternate mechanism.

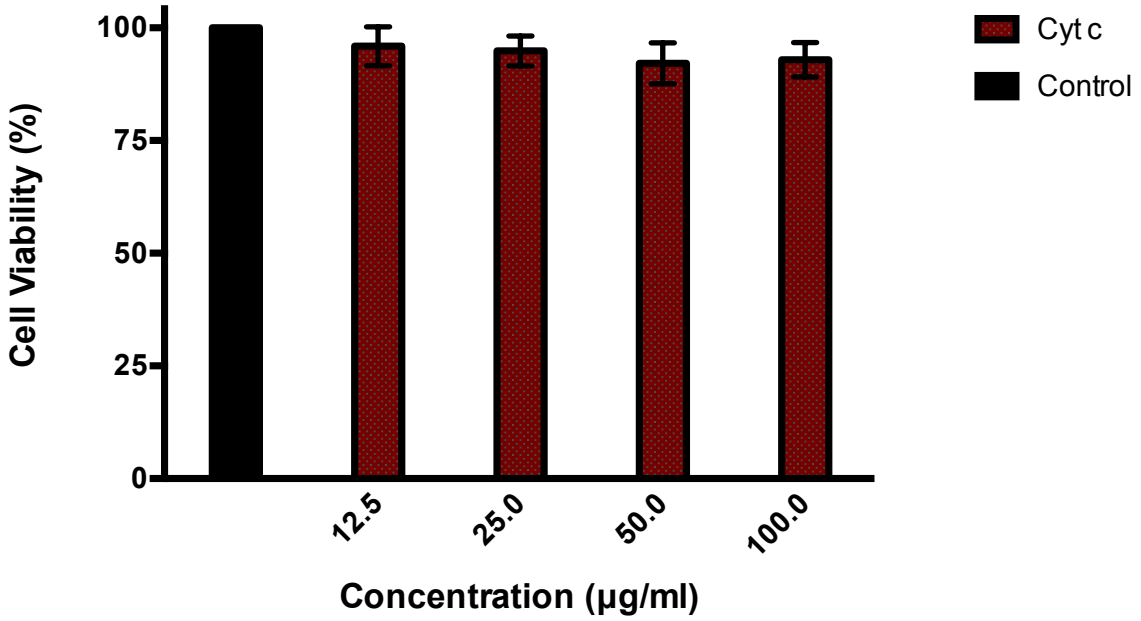

Figure 4.8. Cell viability in HeLa cells. Effect of Cyt c in cell viability following treatment with different concentrations of Cyt c (12.5 to 100 µg/ml) in the presence of extraction buffer A supplemented with 0.03% DDM after 24 h of incubation.

Next, we preliminarily performed cell viability studies in the triple-negative breast cancer cell line MDA-MB-231 after incubation with PSI-LHCI (6.25 - 50 µg/ml) for 24 h as a screening and testing method for an alternate cancerous cell line model system. As observed in Figure 4.9, previously arrested for 18 h in serum starvation media, MDA-MB-231 cells treated with PSI-LHCI for 24 h induced a decrease in cell viability of 53% at a concentration of 12.5 µg/ml compared to untreated cells (control) with 90% cell viability. The MTS assay results were used to determine the IC_{50} values calculated using GraphPad Prism 6 as previously indicated in Chapter 2 - Materials and Methods - Section 2.2.3. The resulting IC_{50}

values obtained for PSI-LHCI were 11.43 µg/ml, and the R-squared value was 0.9787. As a control, extraction buffer A was added to MDA-MB-231 cells at the highest concentration tested (50 µg/ml). Dunnett's multiple comparisons test for one-way repeated measures ANOVA reported statistically significant results for concentrations 12.5 (**P < 0.01), 25 and 50 µg/ml (***P < 0.001) compared to the control. In this work, the TNBC MDA-MB-231 cell line was selected as a model fit to test for cell viability and further studies.

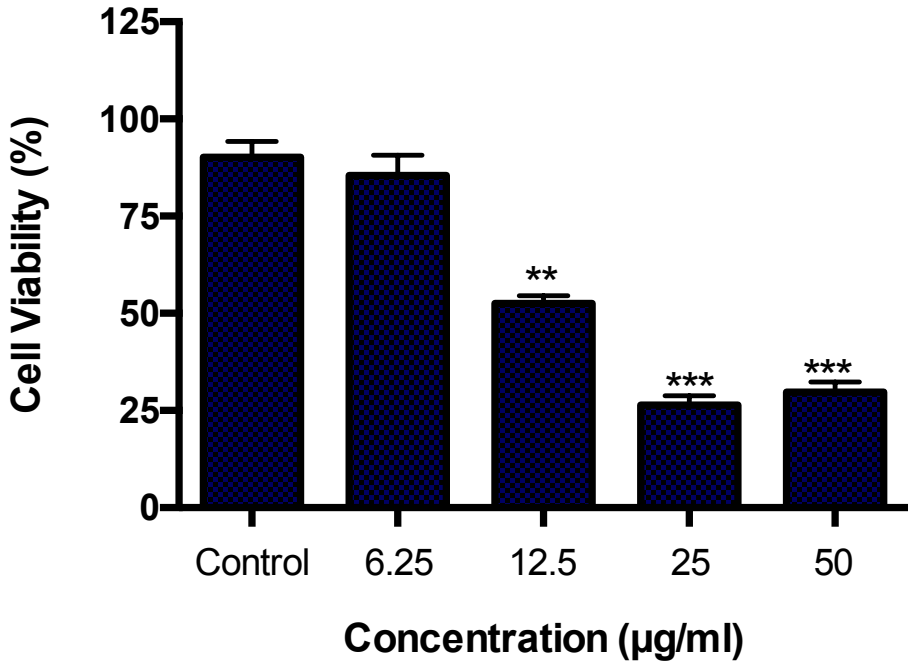

Figure 4.9. Cell viability in the MDA-MB-231 cell line. Effect of PSI-LHCI in cell viability following treatment with different concentrations (from 6.25 to 50 µg/ml) after 24 h of incubation. Incubation with the extraction buffer A at the highest experimental concentration (50 µg/ml) served as a control. Asterisks indicate statistical significance with $^{**}P < 0.01$ and $^{***}P < 0.001$.

Cellular viability (MTS) assays monitored toxicity in TNBC MDA-MB-231 cells upon exposure to cell arrest for 18 h, PSI-LHCI concentrations of 6.25, 12.5, 25, and 50 µg/ml, and incubation times for 6, 12, and 24 h, where n=8.

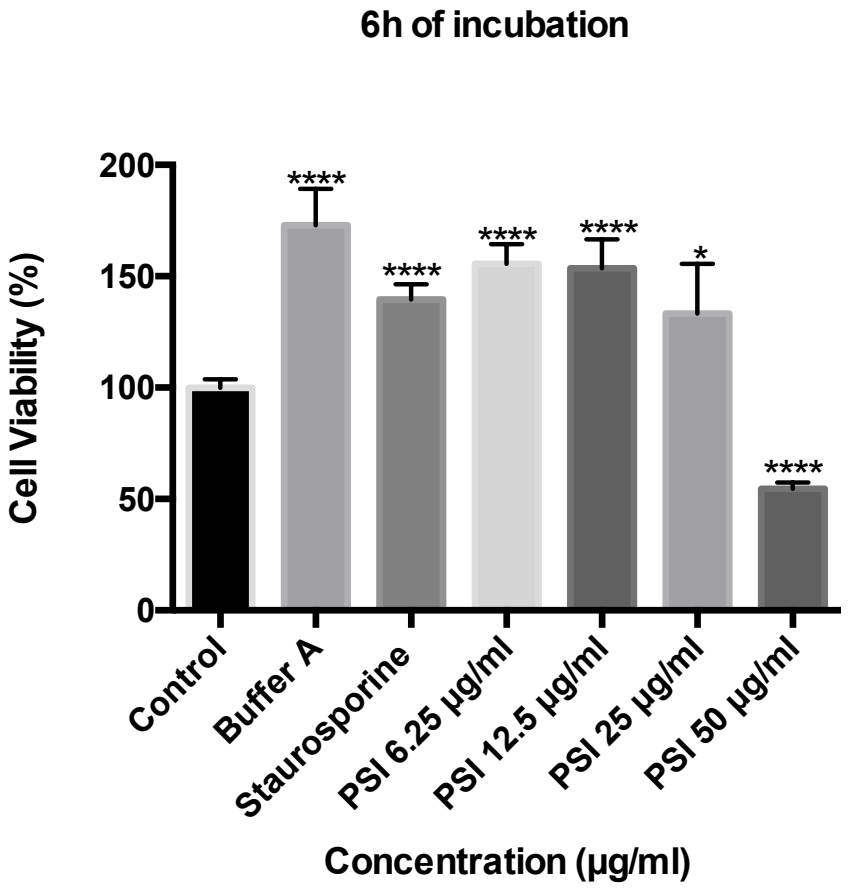

Figure 4.10. Time and Concentration-Dependent Effect of PSI-LHCI in MDA-MB-231 Cells. Effect of PSI-LHCI in cell viability following treatment with different concentrations (6.25 to 50 µg/ml) after 6 h of incubation. Incubation with the extraction buffer A at the highest concentration (50 µg/ml) was used as an experimental control. Staurosporine (2 µM) was used as a positive control. Untreated cells were used as negative control. Asterisks indicate statistical significance with *$P < 0.05$ and ****$P < 0.0001$.

Cell viabilities above 100% were observed after 6 h of incubation period with the negative control of extraction buffer A and the positive control Staurosporine and in concentrations lower than 50 µg/ml PSI-LHCI compared to untreated cells (Figure 4.10). Although a decrease in cell viability at 50 µg/ml PSI-LHCI of 55% was detected, the values observed for 6.25 to 25 µg/ml of PSI-LHCI exceeded the 100% value. This 6 h cell viability assay's experimental uncertainty (error bars) indicated large data variability, thus regarded as a negative result, and discarded as a potential testing parameter.

Consequently, we performed cell viability studies in the MDA-MB-231 cell line after incubation with PSI-LHCI (6.25 - 50 µg/ml) for 12 and 24 h. Our MTS assay results revealed the remarkable time- and concentration-dependent effects of decreased cell viability of *B. braunii* PSI-LHCI against MDA-MB-231 cells. With an increment in PSI-LHCI concentration after 12 and 24 h of incubation, a reduction in cell viability was observed, showing an inverse relationship between proliferation and cell death. A decline in cell viability of 87% was observed for the 12 h incubation period, commencing with the 6.25 µg/ml PSI-LHCI concentration. A reduction in viability was detected around 84% and 79% for the 12.5 and 25 µg/ml PSI-LHCI concentration, respectively, and a considerably lower value of 49% in the highest concentration tested of 50 µg/ml (Figure 4.11). We compared our results with Staurosporine, a strong cytotoxic positive control, used at peak plasma concentration (2 µM), and negative and experimental controls. As observed in Figure 4.12, after 24 h of incubation we observed a statistically significant decrease in viable cells from 100% with negative controls to below 32%

with 25 and 50 µg/ml of PSI-LHCI (****P < 0.0001), in contrast to 52% with Staurosporine.

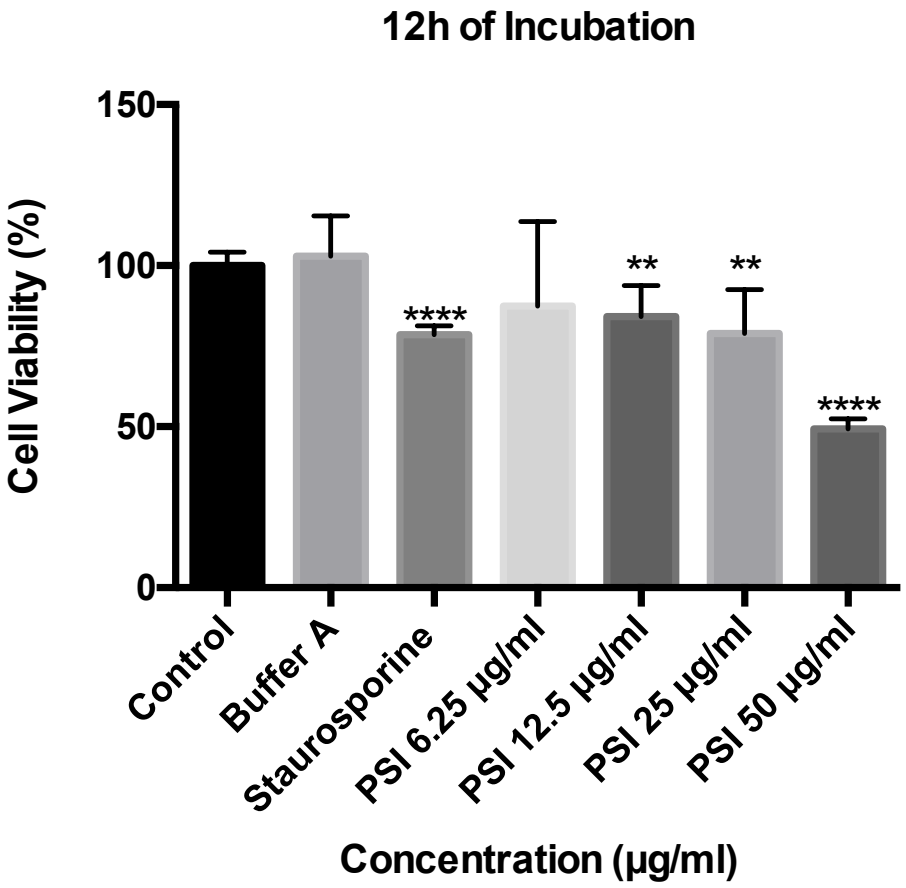

Figure 4.11. Time and Concentration-Dependent Effect of PSI-LHCI in MDA-MB-231 Cells. Effect of PSI-LHCI in cell viability following treatment with different concentrations (6.25 to 50 µg/ml) after 12 hours of incubation. Incubation with the extraction buffer A at the highest concentration tested (50 µg/ml) was used as an experimental control. Staurosporine (2 µM) was used as a positive control. Untreated cells were used as negative control. Asterisks indicate statistical significance with ***P* < 0.01 and ****P* < 0.0001.

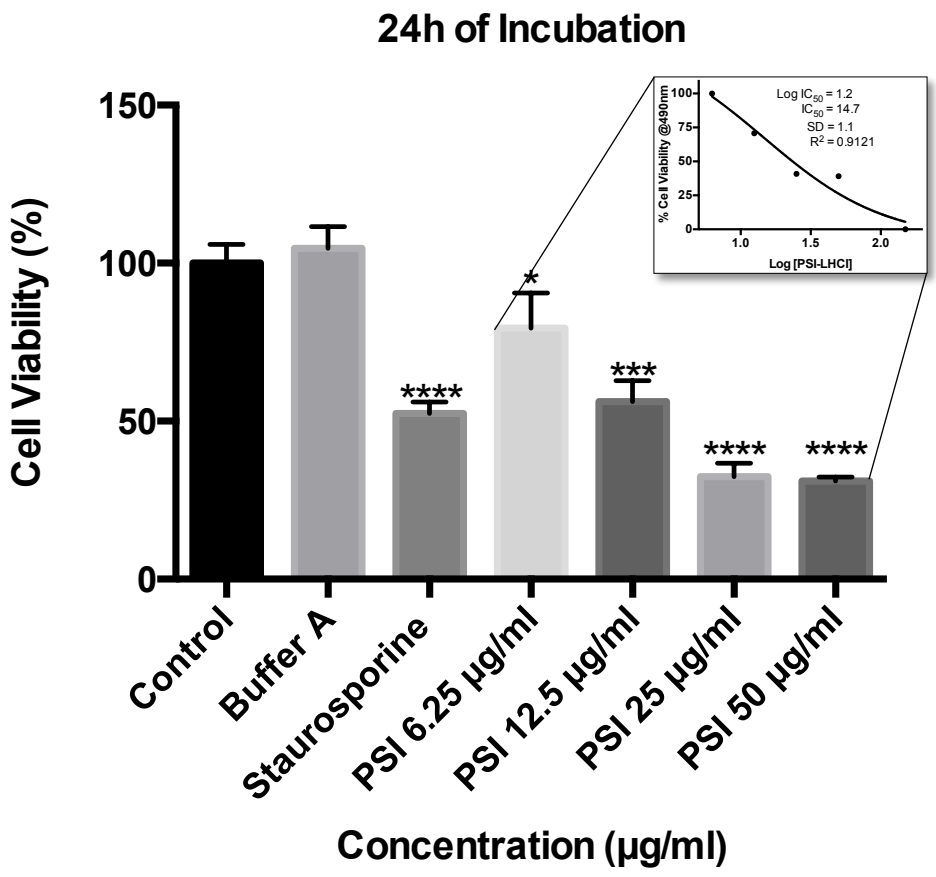

Figure 4.12. Time and Concentration-Dependent Effect of PSI-LHCI in MDA-MB-231 Cells. Effect of PSI-LHCI in cell viability following treatment with different concentrations (6.25 to 50 µg/ml) after 24 h of incubation. Incubation with the extraction buffer A at the highest concentration tested (50 µg/ml) was used as an experimental control. Staurosporine (2 µM) was used as a positive control. Untreated cells were used as a negative control. Asterisks indicate statistical significance with $*P < 0.05$, $***P < 0.01$ and $****P < 0.0001$. Data shown are expressed as mean ± SD performed in triplicate, where n = 8, and the statistical method performed used the two-way analysis of variance (ANOVA).

It is important to highlight that after 6 hours of incubation with PSI-LHCI, a considerable increment in cell viability at low doses showed opposing effects. Accordingly, cell proliferation was inhibited by high concentrations of PSI-LHCI; a hormetic phenomenon was deemed responsible for the stimulatory or proliferative impact observed by the increment in viability at low PSI-LHCI concentrations [185]. Hence, the indicated event of hormesis illustrates the proliferative or adaptive compensatory feedback of cells upon a disturbance in homeostasis due to exposure to low doses of chemical or environmental agents, which otherwise pose damaging effects at higher doses [186].

Moreover, we conducted additional in vitro cell viability studies in TNBC cell lines MDA-MB-231, MDA-MB-468, and the non-cancer cell line, NIH-3T3. Similarly, a concentration-dependent reduction in cell viability was observed after incubation for 6, 12, and 24 h using various concentrations of PSI-LHCI (6.25, 12.5, 25, and 50 µg/ml). At the highest PSI-LHCI concentration (50 µg/ml), a drastic decrease in cell viability was observed to less than 18% in NIH-3T3 cells, and 14% and 7% decreased cell viability in MDA-MB-468 and MDA-MB-231 cells, respectively (data not shown). The findings of the analyzed MTS assay indicate a dose-dependent manner reduction in cellular viability upon treatment of MDA-MB-231 cells with PSI-LHCI. We proceeded to choose the concentration point closest to the IC_{50} value (12.5 µg/ml PSI-LHCI, ***$P < 0.01$) revealed after exposure of MDA-MB-231 cells to PSI-LHCI following 24 h of incubation. The IC_{50} value attained was 14.7 µg/ml with an R squared value of 0.9121, standard error of 1.1, and Log IC_{50} equal to 1.2. Our results confirmed that PSI-LHCI induces a decrease

in cell viability in the triple-negative breast cancer cell line, MDA-MB-231, with superior results than the well-known cancer cell line positive control Staurosporine [187,188].

4.3.3 Cellular Internalization Studies of PSI in MDA-MB-231 Cells

The internalization of PSI-LHCI was determined by confocal laser scanning microscopy (CLSM) after the TNBC MDA-MB-231 cell line, and the non-cancer cell line, NIH-3T3 were seeded at 10,000 cells/well, arrested with 1% FBS in L-15 culture medium for 18 h, and subsequently incubated with PSI-LHCI (12.5 µg/ml) at 37 °C for 24 h. After incubation and fixing, the cells were imaged using a Nikon Eclipse Ti confocal microscope. PSI-LHCI was detected at 663-738 nm after excitation at 640 nm, and DAPI was excited at 405 nm with its emission spotted from 420-480 nm.

A

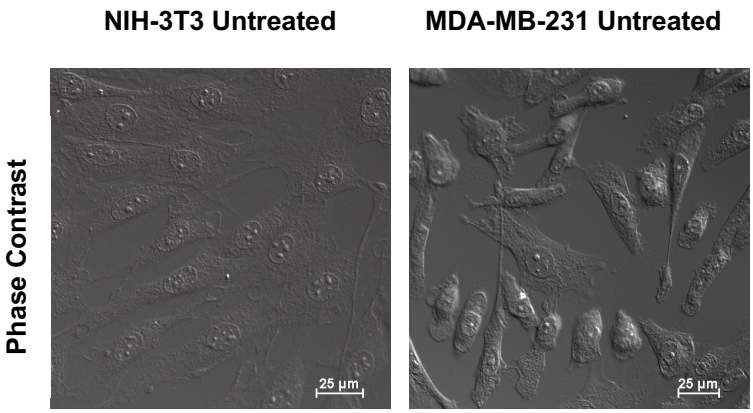

Figure 4.13 *Cont.*

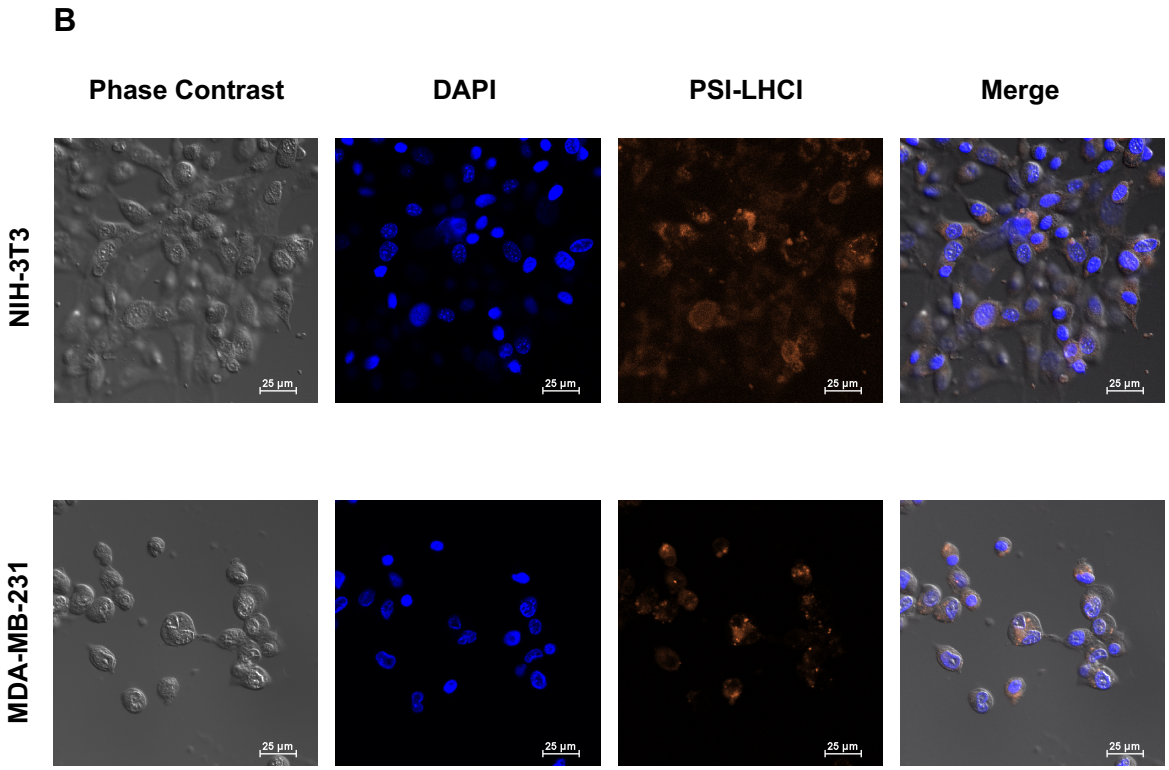

Figure 4.13. Confocal microscopy studies in NIH -3T3 and MDA-MB-231 cell lines. (A) Phase contrast of NIH-3T3 (left) and MDA-MB-231 (right) untreated cells after 24 h of incubation. (B) Internalization of PSI-LHCI. NIH -3T3 and MDA-MB-231 cells were incubated with PSI-LHCI (orange). Nuclei were stained with DAPI (blue). All images were taken at 20X magnification.

As illustrated in Figure 4.13, after 24 h of incubation, PSI-LHCI (orange) is observed in the cell cytoplasm, suggesting the internalization of PSI-LHCI is not cell line-specific, as it exhibited fluorescence by both NIH-3T3 and MDA-MB-231 cells. To visualize and study the intracellular localization and endocytic fate of PSI-LHCI, MDA-MB-231 cells were co-incubated with the amphiphilic marker FM 4-64 for 24 h. Endosomal entrapment was identified by confocal microscopy of Z-series or Z-stack images. Still, as depicted in Fig. 4.14, after 24 h of incubation with PSI-

LHCI (orange) and FM 4-64 (red), PSI-LHCI appears to be present in the cell cytoplasm and not in the nucleus. The merged image manifested a significant obstacle, FM 4-64 emission excited PSI-LHCI sample, thus interfering with the analysis of endosomal entrapment, highlighting the need for a fluorescent probe whose signal does not occlude PSI-LHCI or present overlapping spectra.

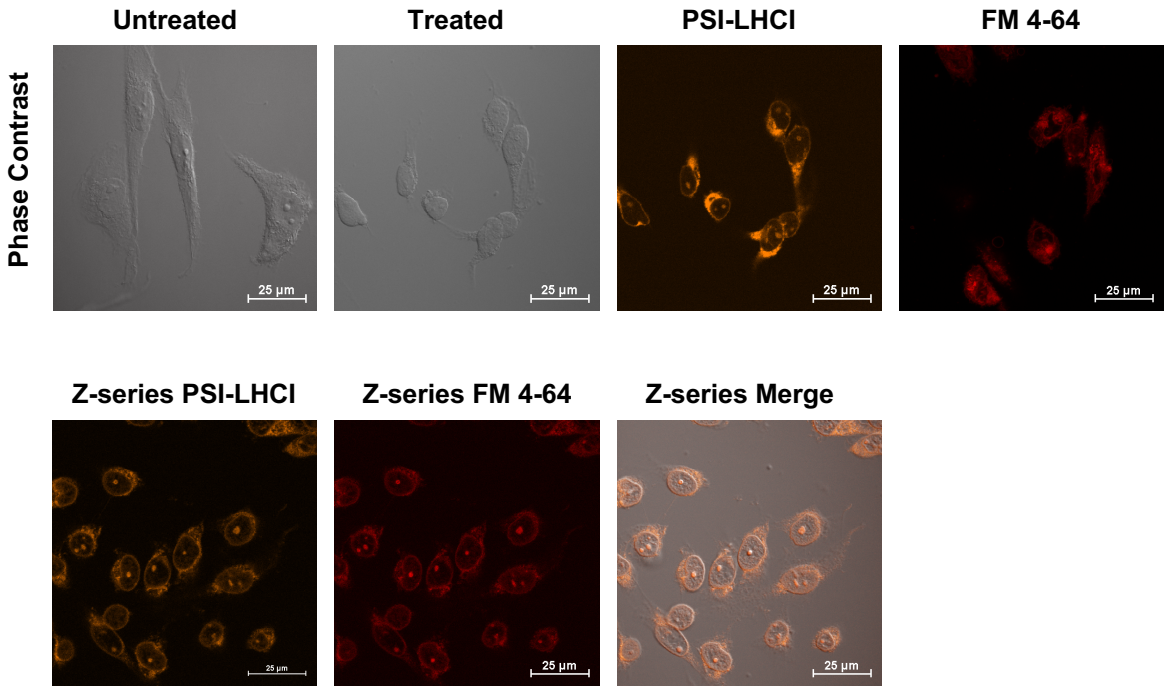

Figure 4.14. Confocal microscopy studies in MDA-MB-231 cells. Phase-contrast MDA-MB-231 (upper left panel) untreated cells, treated cells, and controls after 24 h of incubation with PSI-LHCI. Z-Series Internalization of PSI. MDA-MB-231 cells were incubated with PSI-LHCI (orange) and FM 4-64 (red). All images were taken at 60X magnification.

Supplementary staining procedures addressed fluorescent markers interference and constraints. Internalization studies after 6, 12, and 24 h of incubation were performed and studied by monitoring the distribution of the fluorescence signal of PSI-LHCI (12.5 µg/ml) on MDA-MB-231 cells surface and intracellular localization with CLSM as observed in Fig. 4.15, Fig. 4.16, and Fig. 4.17, respectively. MDA-MB-231 cells plasma membrane was labeled with the CellMask green plasma membrane stain to help define the cellular components bound by the cell membrane after treatment with PSI-LHCI. PSI-LHCI-treated MDA-MB-231 cells were visualized using the Z-series, a straightforward technique of analyzing multiple images at different focal planes (z-stack) of the sample of interest to determine their location within the cell [189].

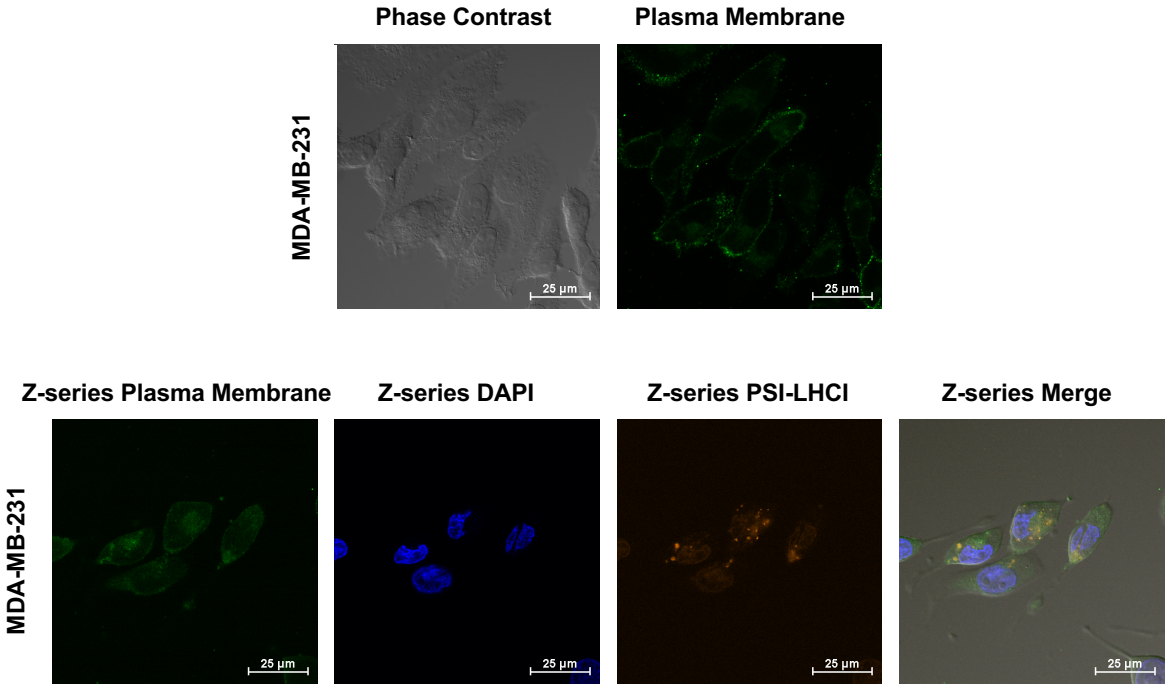

Figure 4.15. Confocal microscopy studies in MDA-MB-231 cells. Phase contrast (upper left panel) and CellMask green plasma membrane (upper right panel) of

MDA-MB-231 cells after 6 h of incubation with PSI-LHCI. Internalization of PSI-LHCI. MDA-MB-231 cells were incubated with PSI-LHCI (orange), DAPI (blue), and CellMask Plasma Membrane (green). All images were taken at 60X magnification.

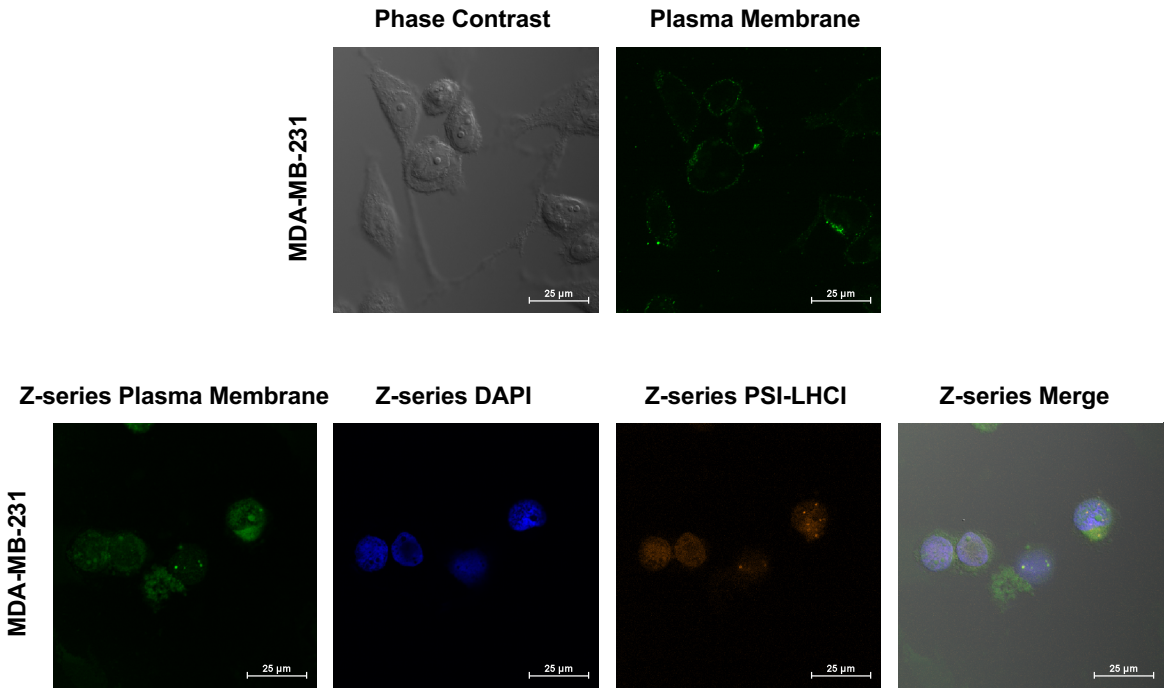

Figure 4.16. Confocal microscopy studies in MDA-MB-231 cells. Phase contrast (upper left panel) and CellMask green plasma membrane (upper right panel) of MDA-MB-231 cells after 12 h of incubation with PSI-LHCI. Internalization of PSI-LHCI. MDA-MB-231 cells were incubated with PSI-LHCI (orange), DAPI (blue), and CellMask Plasma Membrane (green). All images were taken at 60X magnification.

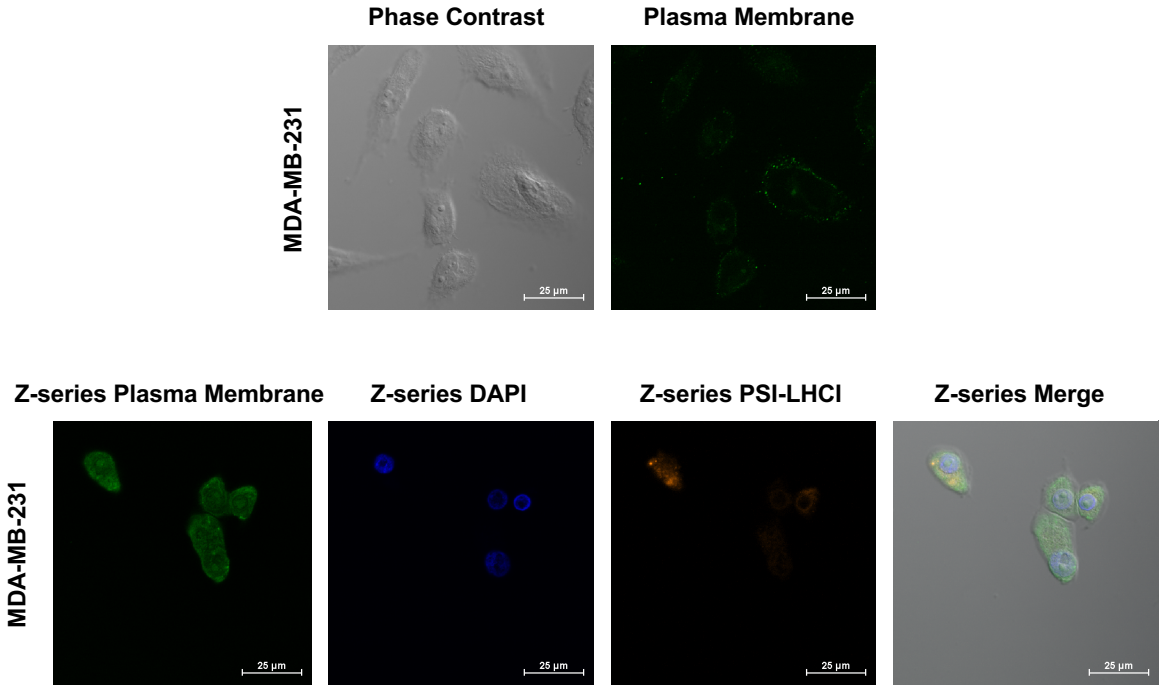

Figure 4.17. Confocal microscopy studies in MDA-MB-231 cells. Phase contrast (upper left panel) and CellMask green plasma membrane (upper right panel) of MDA-MB-231 cells after 24 h of incubation with PSI-LHCI. Internalization of PSI-LHCI. MDA-MB-231 cells were incubated with PSI-LHCI (orange), DAPI (blue), and CellMask Plasma Membrane (green). All images were taken at 60X magnification.

Out of all the incubation times tested, following 24 hours of treatment, PSI-LHCI, which exhibits natural emission or autofluorescence, appeared to have produced the most impairment to the cell membrane. Qualitative visual results of PSI-LHCI (orange), plasma membrane (green), DAPI nuclear stain (blue), and a merged image of all the dyes provided a clear depiction of the fate of PSI-LHCI

and cell membrane integrity. Green fluorescence signal intensity increased significantly from localized plasma membrane boundaries observed after 6 h of incubation to uniform cytoplasmic (12 h of incubation) and widespread nuclear distribution, representing PSI-LHCI impact and location within the membrane after 24 h of treatment (Fig. 4.17). The mean fluorescence intensity (MFI) of MDA-MB-231 cells after 6 h of incubation with PSI-LHCI, when compared with control, represented as mean ± standard deviation (SD), was 108.03 ± 12.23 and 94.14 ± 48.72. After 12 h of incubation with PSI-LHCI compared with control, MDA-MB-231 cells MFI was 503.08 ± 146.01 and 74.12 ± 10.02 respectively. According to the literature, internalized proteins and, for instance, PSI-LHCI in a receptor-unbound state are expected to undergo lysosomal trafficking [190]. Internalization and localization studies of PSI-LHCI in MDA-MB-231 cells monitored time-dependent intracellular traffic and contributed critical knowledge towards reporting non-specific internalization and PSI-LHCI damage-mediated cytotoxicity while differentiating surface membrane staining from intracellular staining. Therefore, supporting the premise that PSI-LHCI does not remain on the cell's surface; instead, it is ultimately internalized.

4.3.4 Study of ROS Generation in Thylakoids and in MDA-MB-231 Cells after PSI Treatment

Cellular total ROS production and superoxide detection were directly monitored and determined using CLSM. Fixed and live MDA-MB-231 cells in complete and serum starvation L-15 medium (1% FBS) were monitored in real-

time after incubating with PSI-LHCI (12.5 µg/ml) for 1 h or 24h, ROS inducer (Pyocyanin 1µM), and ROS inhibitor/scavenger (N-acetyl-L-cysteine) which were used as positive and negative controls, respectively. Sample pretreatment performed for 30 min with N-acetyl-L-cysteine prevented ROS generation. Compensation correction was performed with single-stained standards.

As observed in Figure 4.18A, untreated cells present a low autofluorescence signal. In contrast, a vivid uniform green cytoplasmic stain was observed at the occurrence of increased levels of oxidative stress, and bright red nuclear staining was detected in superoxide-positive cells. Pyocyanin-induced samples exhibited a bright nuclear and cytoplasmic signal, while cells pretreated for 30 min with the negative control and ROS inhibitor, N-acetyl-L-cysteine, did not show uniform fluorescence upon induction. Figure 4.18B results resolved, PSI-LHCI increased reactive oxygen species generation and superoxide production in serum-starved conditions following normal experimental conditions of 24 h versus 1 h incubation treatment in complete media. The MFI of MDA-MB-231 cells after 1 h incubation exhibited a PSI-LHCI (120.77 ± 5.54), oxidative stress (142.13 ± 54.24), and superoxide (98.63 ± 36.03) signal when compared to 24 h incubation which presented an intensified PSI-LHCI (201.45 ± 46.11), oxidative stress (366.73 ± 85.95), and superoxide (101.01 ± 37.64) signal.

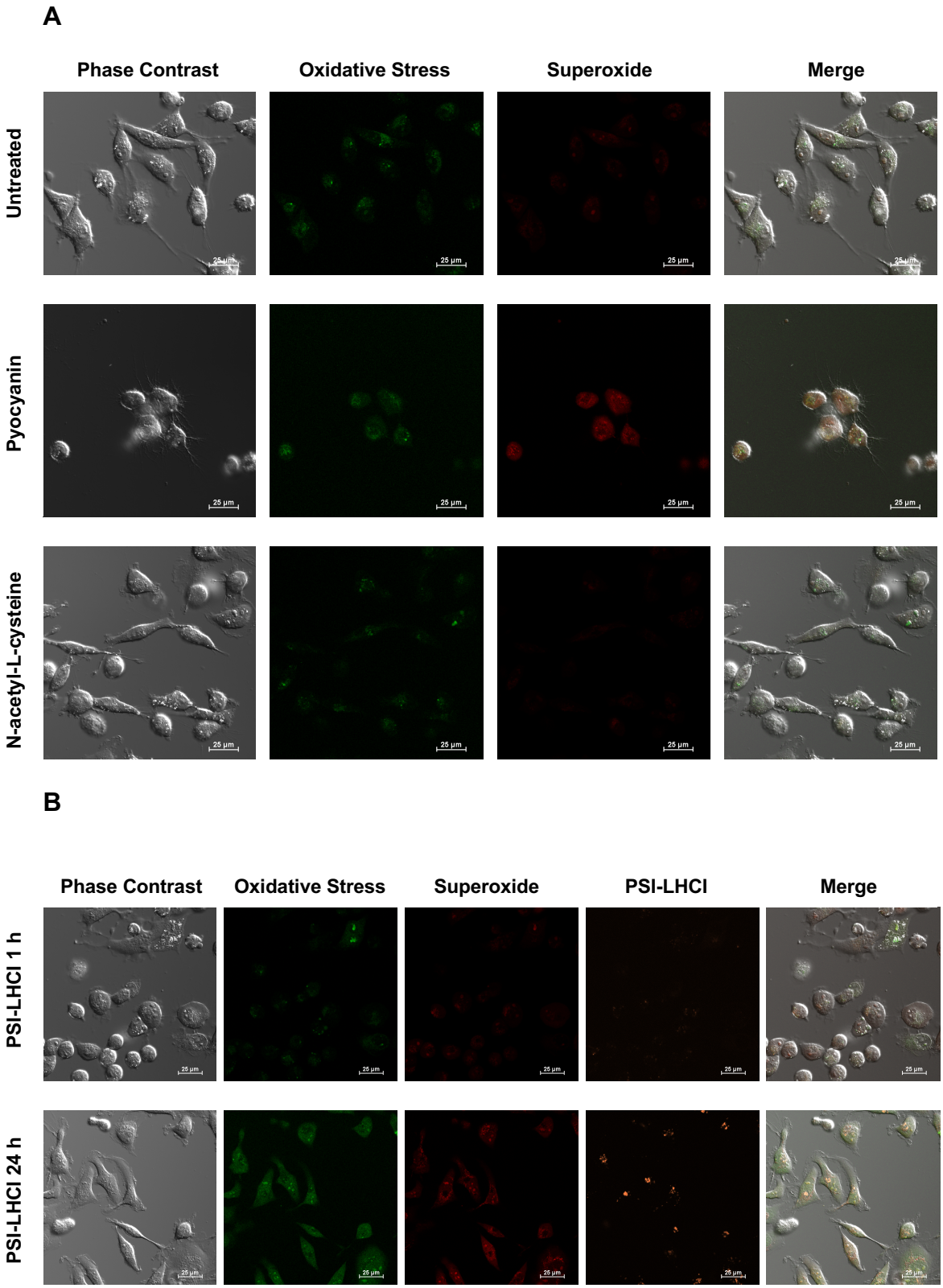
A
Phase Contrast
Oxidative Stress
Superoxide
Merge
Untreated
Pyocyanin
N-acetyl-L-cysteine
B
Phase Contrast
Oxidative Stress
Superoxide
PSI-LHCI
Merge
PSI-LHCI 1 h
PSI-LHCI 24 h

Figure 4.18. ROS/Superoxide detection microscopy studies in MDA-MB-231 live cells. Phase-contrast MDA-MB-231 untreated cells, positive (Pyocyanin) and negative control ROS inhibitor (N-acetyl-L-cysteine) (A). PSI-LHCI (12.5 μg/ml) after 1 h of incubation (B). Green cytoplasmic stain (FITC filter), red nuclear stain (CY3 filter), orange PSI-LHCI (Alexa 555) of cells in serum-starved or complete medium. All images were taken at 20X magnification.

Thus, a marked contrast in the fluorescence signal was observed between 1 h and 24 h incubation periods for the two fluorescent dyes: green oxidative stress detection reagent and red superoxide detection reagent. Time-course fluorescence changes reinforced the constitutive internalization of PSI-LHCI after 24 h of incubation which was monitored by the increment in orange signal in the Alexa Fluor 555 channel. An increase in signal intensity was detected over time when oxidative stress and superoxide concentration levels were monitored, surveyed in the FITC channel and CY3 filter channel, respectively. Hence, ROS and superoxide generation and accumulation and subsequent rise in oxidative stress have thereby been further confirmed after MDA-MB-231 cells were exposed to PSI-LHCI (12.5 μg/ml) and analyzed through this ROS/Superoxide assay.

4.3.5 Annexin V/Propidium Iodide and Caspase-3 Staining Assays for Cell-Death Assessment

Analyzing the unique morphological hallmarks in ongoing cell demise requires distinguishing among the different cell death pathways, including

apoptosis, necrosis, and autophagy, by multiparameter studies involving qualitative and functional criteria.

In our research, qualitative cell death mechanism analyses were carried out, starting with the nuclear counterstain DAPI, which can help identify the condensed nuclei of apoptotic cells. Apoptosis was studied via the Alexa Fluor 488 Annexin V and with the live and apoptotic impermeant dye PI to help distinguish apoptotic cells from dead cells, respectively. Alternatively, we used the Nuclear Green DCS1 was used to analyze dead cells. MDA-MB-231 cells plasma membrane was labeled with the CellMask green plasma membrane stain to help define the cellular components bound by the cell membrane after treatment with PSI-LHCI. Unlike lipophilic dyes such as FM 4-64, the fluorescent probes were selected to avoid interference with the sample, which created an imaging problem due to the excitation of the sample by the emission of the FM 4-64 dye. Apoptosis activation was checked for Caspase 3 activity with NucView 405 Caspase-3 substrate to detect caspase-3/7 activity by confocal microscopy using the DAPI channel. This substrate contains the caspase-3/7 DEVD recognition sequence and a fluorescent DNA dye, allowing for the detection of caspase activity and nuclear morphological changes by confocal imaging [191].

An increase in ROS may cause cell death; therefore, we initially searched for hallmarks of apoptosis using DAPI, Annexin V, and PI (Figure 4.19). The analysis of DAPI-stained MDA-MB-231 cells unveiled a brightly stained nuclear morphology and minor condensation, initially regarded as an early apoptotic marker; however, dead or necrotic cells appeared stained bright red due to the

differential uptake of the DNA binding dye (PI) that do not traverse the plasma membrane of apoptotic or living cells [192]. The merged image in magenta is interpreted as the overlap between neighboring fluorophores or colocalization of the blue (DAPI) and red (PI) signals and used as a discernable method to detect apoptosis; however, distinguishing apoptotic to non-apoptotic cell death is not a straightforward process [193]. After staining the cells with Annexin V, no apparent green fluorescence was detected. Therefore, this assay did not identify early apoptotic cells. Nevertheless, the stronger and condensed red fluorescence observed has been generally represented as the typical nuclear staining of dead cells [194]. Caspase-3 activity was examined due to their active role in programmed cell death or apoptosis; no signal was detected [192]. Thus, an alternative cell death pathway should be responsible for the cellular cytotoxicity sustained by MDA-MB-231 cells after 24 h treatment with PSI-LHCI.

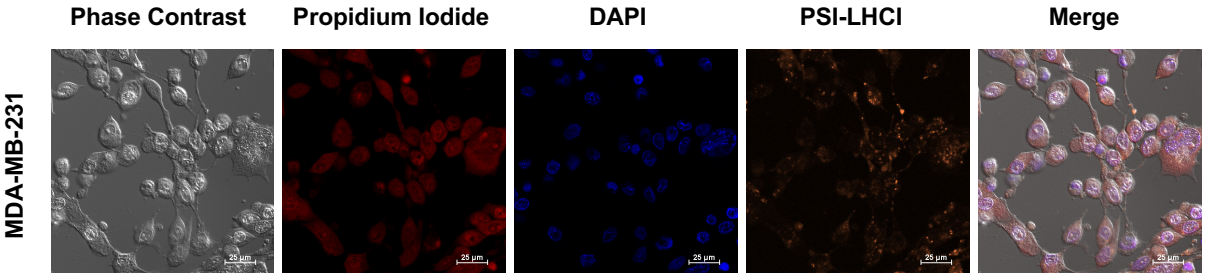

Figure 4.19. Confocal microscopy studies in MDA-MB-231 cell line. DAPI/PI-stained cells were treated with PSI-LHCI after 24 h of incubation to determine apoptosis and PSI-LHCI localization. Merged image (magenta) represents the colocalization of DAPI (blue) and PI (red) staining and PSI-LHCI localization in MDA-MB-231 cells. All images were taken at 20X magnification.

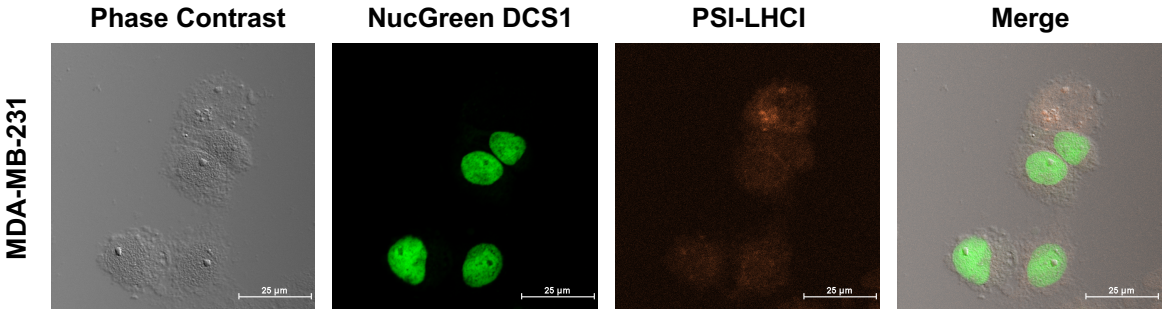

Figure 4.20. DNA content microscopy studies in MDA-MB-231 cells. Phase-contrast MDA-MB-231 cells after 24 hours of incubation with PSI-LHCI at a concentration of 12.5 µg/ml. Green nuclear stain (FITC filter), orange PSI-LHCI (Alexa 555 filter) of cells in serum starvation medium. All images were taken at 60X magnification.

In Figure 4.20, we analyzed DNA content in dead cells with the DNA-selective and cell-impermeant green, fluorescent dye Nuclear Green. MDA-MB-231 cells exhibited a high-intensity fluorescence after treatment with PSI-LHCI (12.5 µg/ml) and 24 h of incubation, representing the labeling of necrotic and apoptotic cells after PSI-LHCI treatment. Previous studies with Annexin V/PI only exhibited a red concentrated cell nucleus suggesting necrotic or late apoptosis cell staining, whereas Annexin V did not show any typical apoptosis marker. Nuclear green DCS1 results indicate MDA-MB-231 cells undergo late-stage apoptosis or necrosis after PSI-LHCI 24 h treatment. Necrosis is evidenced by the presence of dead cells product of environmental perturbations and pathologies that led to ROS increase and mitochondria disruption, but fails to specify how the death occurred; thus, further cell death mechanism assays followed [192,195].

4.3.6 Mitochondrial Membrane Potential Assay

Intracellular loss of mitochondrial membrane potential ($\Delta\Psi M$) was evaluated in MDA-MB-231 cells using the lipophilic cationic fluorescent dye (5,5',6,6'-tetrachloro-1,1',3,3'- tetraethylbenzimidazolylcarbocyanine iodide) through the JC-1 assay by measuring the ratio of the aggregated red form fluorescence, which tends to accumulate in the mitochondrial matrix, divided by the green monomeric form fluorescence, that localizes in the cytosol. The ratio of red to green fluorescence presents a decline in the average fluorescence signal upon increasing the PSI-LHCI dose. In Figure 4.21, we observed that the PSI-LHCI concentration of 50 µg/ml induced a decrease in the mitochondrial membrane potential of MDA-MB-231 cells after treatment and incubation with JC-1 dye for 15 min, likely by direct interaction and destabilization of the mitochondrial membrane, and consequently triggering cell death like other ROS-generating anticancer activity drugs [196]. These results are statistically significant at the level of ****$P < 0.0001$ compared to the positive control Staurosporine with a significance level of **$P < 0.01$. However, at PSI-LHCI concentrations of 12.5 µg/ml. MDA-MB-231 cells retained their mitochondrial membrane potential.

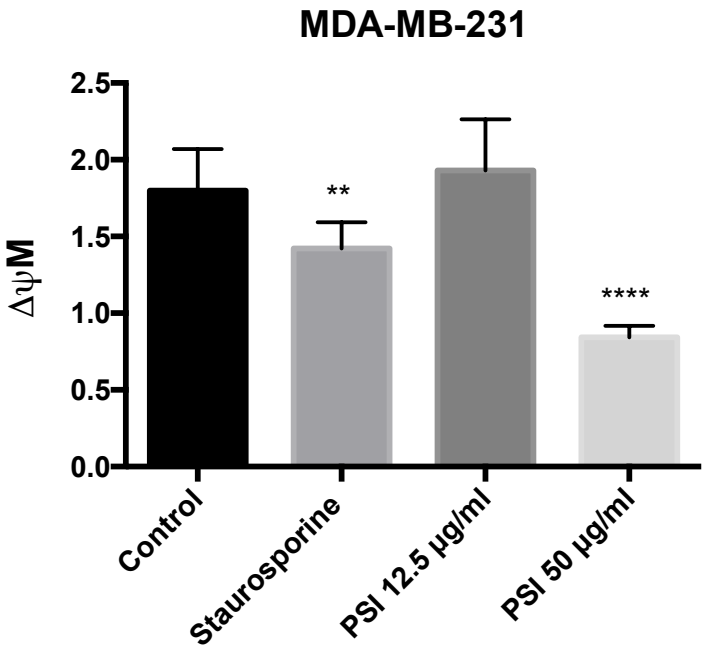

Figure 4.21. Evaluation of the mitochondrial membrane potential (ΔΨM) of MDA-MB-231 cells after treatment with PSI-LHCI. The bars represent mean ± S.D. where n = 8. Asterisks indicate statistical significance with ***P* < 0.01 and ****P* < 0.0001.

The red to green fluorescence ratio is reduced in dead cells and in cells experiencing apoptotic or non-apoptotic cell death compared to healthy cells. Thus, a decrease in mitochondrial membrane potential or depolarization is linked to the opening of mitochondrial membrane permeability pores and the loss in electrochemical gradient, which is utilized as a symbol of cell health [197]. Hence, these results indicate that MDA-MB-231 cell death upon treatment with PSI-LHCI is mediated by a mitochondrial-dependent pathway.

4.3.7 Autophagy-Associated Cell Death Assay

The final cell death mechanism examined was ROS-induced autophagy, also known as macroautophagy via the LC3 lysosomal pathway. The housekeeping ROS-induced autophagic cell death pathway was determined following treatment with PSI-LHCI (12.5 µg/ml) in synchronously nutrient-starved MDA-MB-231 cells. During the highly regulated lysosome-based cellular recycling process, degradation of cytoplasmic components is mediated by the double-membrane vesicles or autophagosomes, the morphological hallmark of macroautophagy [198].

To directly measure autophagic vacuoles and monitor autophagic flux, complete media and serum starvation conditions were used. Untreated negative control MDA-MB-231 cells, positive controls, namely the autophagy inducer rapamycin, and the lysosomal activity inhibitor and autophagic flux detector chloroquine, in addition to experimental samples treated with PSI-LHCI after 24 h of the incubation period, or induction was used. Fluorescence intensity was detected in autophagic vacuoles after incubation with the green microscopy dual detection reagent by confocal microscopy. Fixed-stained cells were monitored for autophagy activity at 40X magnification using the standard FITC filter set for imaging the autophagic signal. In contrast, the nuclear signal was obtained using the DAPI channel. As observed in Figure 4.22, the accumulation of the green detection reagent, represented by localized globular autophagic vacuoles or vesicles, was identified in the positive controls, rapamycin, rapamycin & chloroquine as dotted structures of increased fluorescence intensity.

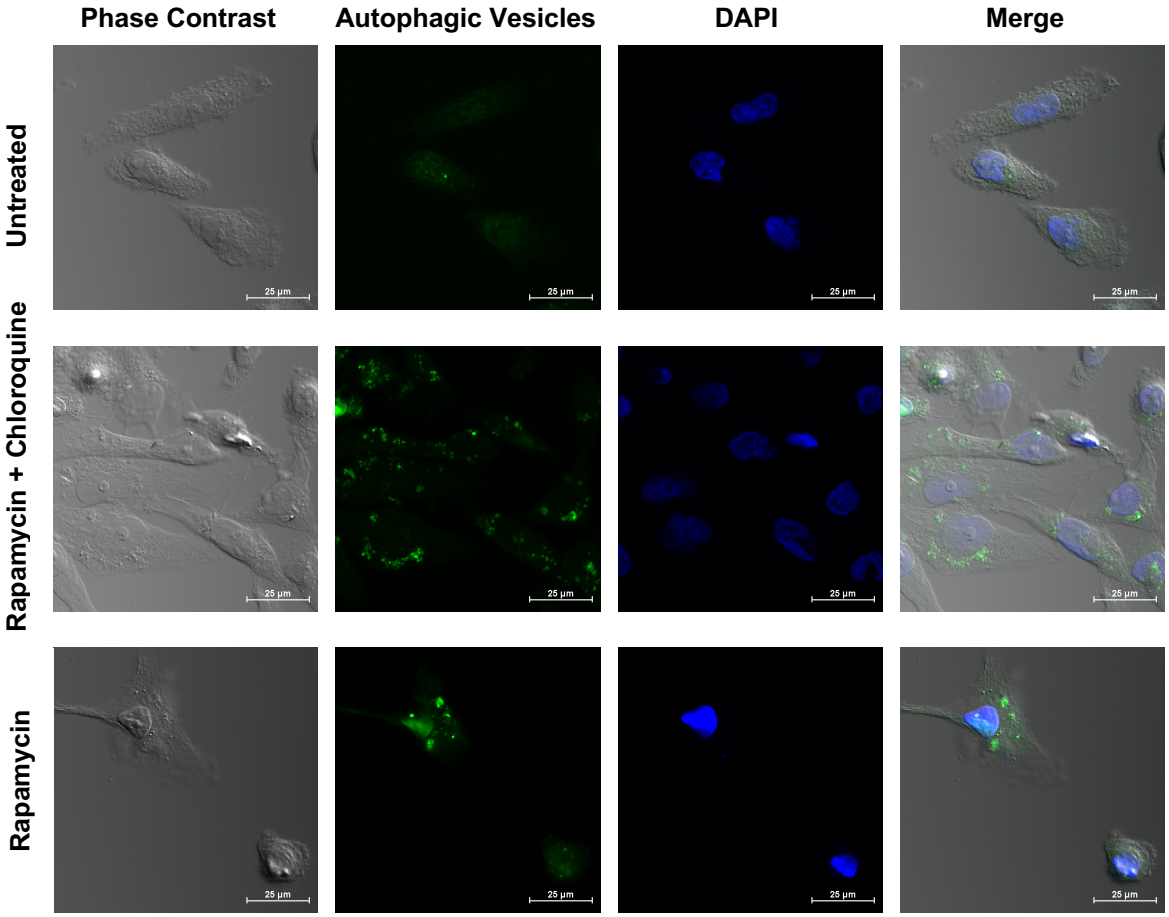

Figure 4.22. Autophagy confocal microscopy studies in MDA-MB-231 cells. Phase-contrast of MDA-MB-231 cells, untreated cells, autophagy inducer rapamycin, and chloroquine as a positive control. Blue nuclear stain (DAPI filter) and green autophagic vesicles (FITC filter) of cells in complete medium. All images were taken at 40X magnification.

Untreated and chloroquine-treated MDA-MB-231 cells were incubated in L-15 medium with 1% FBS, where the starvation medium is recognized as an autophagy inducer treatment and chloroquine as a positive control. Figure 4.23A

revealed a typical uniform but diffused positive autophagy signal in the cytoplasm and the nucleus, likely due to the incubation period as stated in the manufacturers' protocol response to controls is time and concentration dependent. The starvation medium is recognized as an autophagy inducer treatment.

After treatment with low critical micellar concentration detergents such as DDM, membrane pigment-protein complexes such as PSI-LHCI self-assemble in larger mixed protein-detergent oblate ellipsoid micelles while retaining their functional and biological properties, thus enabling interaction with the cell membrane and cytotoxic effects during in vitro studies [140]. Experimental treatment of MDA-MB-231 cells with PSI-LHCI (12.5 µg/ml) after 24 h of incubation time revealed a bright fluorescent orange signal obtained using the Alexa Fluor 555 channel corresponding to the autofluorescent pigment-protein complex. The blue nuclear stain Hoechst exhibited typical nuclear staining. The green detection signal observed in the TNBC MDA-MB-231 cells as punctuate structures in the autophagic vacuoles and diffused throughout the nucleus and cytoplasm is presumably the LC3 autophagosome marker protein. These results confirm that ROS-rich PSI-LHCI pigment-protein complex in serum starvation conditions induces autophagy (Fig. 4.23B) [199].

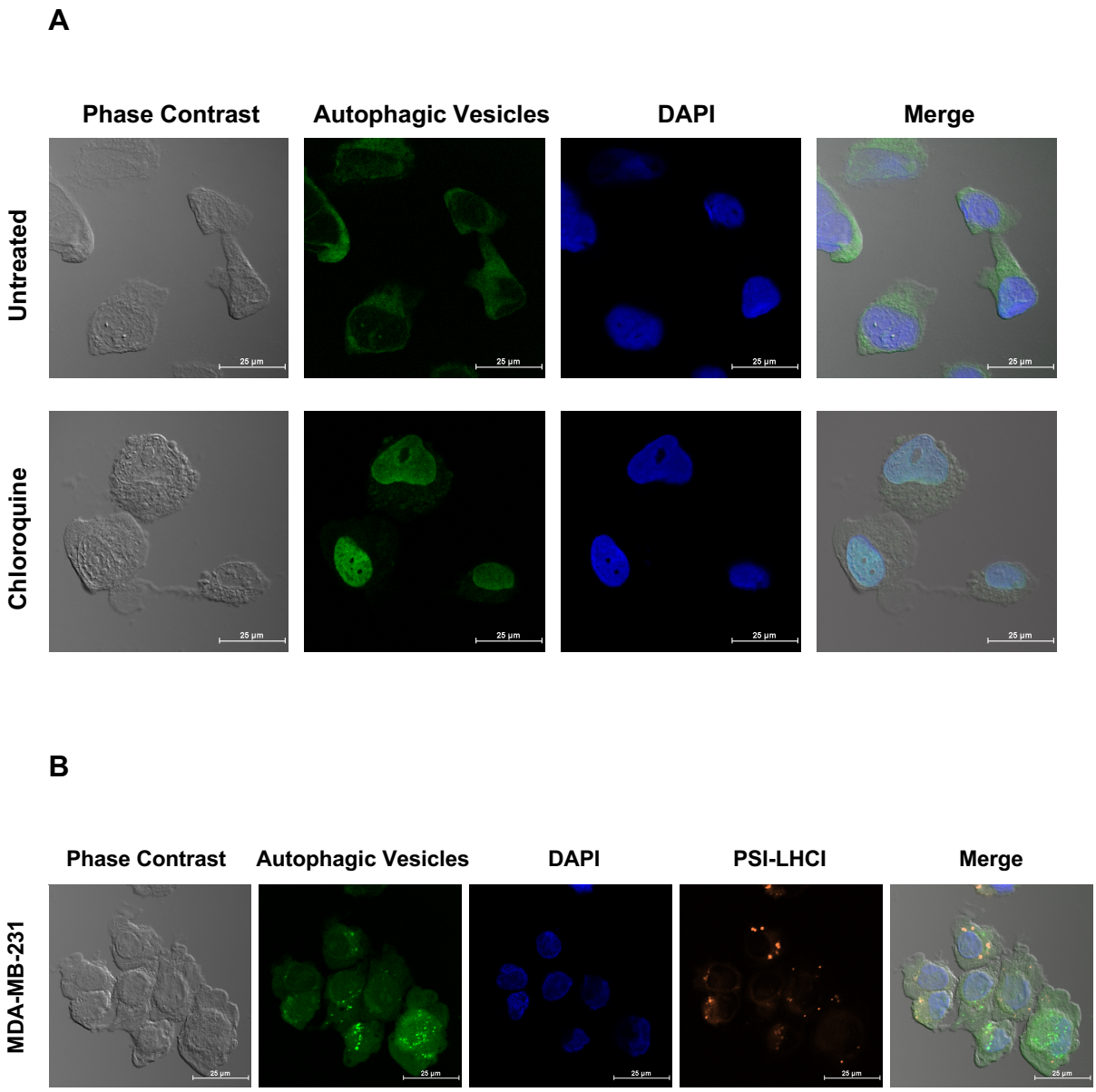

Figure 4.23. Autophagy confocal microscopy studies in MDA-MB-231 cells. Phase-contrast MDA-MB-231 cells, untreated cells, starvation, and Chloroquine as a positive control (A). PSI-LHCI after 24 h of incubation with a concentration of 12.5 μg/ml (B). Blue nuclear stain (DAPI filter), green autophagic vesicles (FITC filter), PSI-LHCI (Alexa 555 filter) of cells in serum starvation medium. All images were taken at 40X magnification.

4.4 Conclusions

At first, Chl *a* fluorescence transients OJIP analysis was used as a ROS stress and high light energy detector to study photoprotective defense mechanisms. As a photosynthetic organism, *B. braunii* must avoid the adverse effects of excess light; consequently, with the results obtained, intense LED light conditions to generate ROS were averted. Exposure of MDA-MB-231 cells to ROS-rich PSI-LHCI has resulted in attenuated cell death following autophagic and necrotic cell death mechanisms. This research explores the potential of *B. braunii* PSI-LHCI as a human breast cancer cell therapy candidate, however, strategies in designing microalgal PSI-LHCI delivery systems to ensure the specificity, stability, efficacy, and increased bioavailability of the pigment-protein complex for *in vivo* application are critical for forthcoming studies. The assessment of proliferation, migration, and invasion of cancer cells would address PSI-LHCI potential as an anticancer agent. Future work will focus on the processing technologies and economic feasibility of microalgal-based high-value products by optimizing protein purification methods, improving yield, and addressing pharmaceutical marketability challenges. Unanswered questions remain; thus, careful consideration should be given to the interplay and manipulation of ROS and autophagy to induce death in cancerous cells. To date, and as far as we know, this is the first study to report the cytotoxic effects and mechanisms of cell death induced by *B. braunii* PSI-LHCI against the TNBC cell line MDA-MB-231.

References:

1. Wellman, C.H.; Osterloff, P.L.; Mohiuddin, U. Fragments of the Earliest Land Plants. *Nature* **2003**, *425*, 282–285, doi:10.1038/nature01884.
2. Katiyar, R.; Gurjar, B.R.; Biswas, S.; Pruthi, V.; Kumar, N.; Kumar, P. Microalgae: An Emerging Source of Energy Based Bio-Products and a Solution for Environmental Issues. *Renew. Sustain. Energy Rev.* **2017**, *72*, 1083–1093, doi:10.1016/j.rser.2016.10.028.
3. Department of Energy Announces Nearly $34 Million to Advance Waste and Algae Bioenergy Technology.
4. Khan, M.I.; Shin, J.H.; Kim, J.D. The Promising Future of Microalgae: Current Status, Challenges, and Optimization of a Sustainable and Renewable Industry for Biofuels, Feed, and Other Products. *Microb. Cell Factories* **2018**, *17*, 36, doi:10.1186/s12934-018-0879-x.
5. Tan, J.S.; Lee, S.Y.; Chew, K.W.; Lam, M.K.; Lim, J.W.; Ho, S.-H.; Show, P.L. A Review on Microalgae Cultivation and Harvesting, and Their Biomass Extraction Processing Using Ionic Liquids. *Bioengineered* **2020**, *11*, 116–129, doi:10.1080/21655979.2020.1711626.
6. Pugliese, A.; Biondi, L.; Bartocci, P.; Fantozzi, F. Selenastrum Capricornutum a New Strain of Algae for Biodiesel Production. *Fermentation* **2020**, *6*, 46, doi:10.3390/fermentation6020046.
7. Mata, T.M.; Martins, A.A.; Caetano, Nidia.S. Microalgae for Biodiesel Production and Other Applications: A Review. *Renew. Sustain. Energy Rev.* **2010**, *14*, 217–232, doi:10.1016/j.rser.2009.07.020.
8. Abo, B.O.; Odey, E.A.; Bakayoko, M.; Kalakodio, L. Microalgae to Biofuels Production: A Review on Cultivation, Application and Renewable Energy. *Rev. Environ. Health* **2019**, *34*, 91–99, doi:10.1515/reveh-2018-0052.
9. Anemaet, I.G.; Bekker, M.; Hellingwerf, K.J. Algal Photosynthesis as the Primary Driver for a Sustainable Development in Energy, Feed, and Food Production. *Mar. Biotechnol. N. Y. N* **2010**, *12*, 619–629, doi:10.1007/s10126-010-9311-1.
10. Arif, M.; Bai, Y.; Usman, M.; Jalalah, M.; Harraz, F.A.; Al-Assiri, M.S.; Li, X.; Salama, E.-S.; Zhang, C. Highest Accumulated Microalgal Lipids (Polar and Non-Polar) for Biodiesel Production with Advanced Wastewater Treatment: Role of Lipidomics. *Bioresour. Technol.* **2020**, *298*, 122299, doi:10.1016/j.biortech.2019.122299.
11. Barkia, I.; Saari, N.; Manning, S.R. Microalgae for High-Value Products towards Human Health and Nutrition. *Mar. Drugs* **2019**, *17*, E304, doi:10.3390/md17050304.
12. Alishah Aratboni, H.; Rafiei, N.; Garcia-Granados, R.; Alemzadeh, A.; Morones-Ramírez, J.R. Biomass and Lipid Induction Strategies in Microalgae for Biofuel Production and Other Applications. *Microb. Cell Factories* **2019**, *18*, 178, doi:10.1186/s12934-019-1228-4.

13. Williams, P.J. le B.; Laurens, L.M.L. Microalgae as Biodiesel & Biomass Feedstocks: Review & Analysis of the Biochemistry, Energetics & Economics. *Energy Environ. Sci.* **2010**, *3*, 554, doi:10.1039/b924978h.
14. Caporgno, M.P.; Mathys, A. Trends in Microalgae Incorporation Into Innovative Food Products with Potential Health Benefits. *Front. Nutr.* **2018**, *5*, 58, doi:10.3389/fnut.2018.00058.
15. Hernández, D.; Riaño, B.; Coca, M.; García-González, M.C. Saccharification of Carbohydrates in Microalgal Biomass by Physical, Chemical and Enzymatic Pre-Treatments as a Previous Step for Bioethanol Production. *Chem. Eng. J.* **2015**, *262*, 939–945, doi:10.1016/j.cej.2014.10.049.
16. Hosikian, A.; Lim, S.; Halim, R.; Danquah, M.K. Chlorophyll Extraction from Microalgae: A Review on the Process Engineering Aspects. *Int. J. Chem. Eng.* **2010**, *2010*, 1–11, doi:10.1155/2010/391632.
17. Bez, G. de C.; Jordão, B.Q.; Vicentini, V.E.P.; Mantovani, M.S. Differential Protection of A and B Chlorophyll in MMC-Mediated Induction of Chromatid and Isochromatid Breaks in Human Lymphocytes Culture. *Cytologia (Tokyo)* **2001**, *66*, 313–318, doi:10.1508/cytologia.66.313.
18. Bleakley, S.; Hayes, M. Algal Proteins: Extraction, Application, and Challenges Concerning Production. *Foods* **2017**, *6*, 33, doi:10.3390/foods6050033.
19. Galasso, C.; Gentile, A.; Orefice, I.; Ianora, A.; Bruno, A.; Noonan, D.M.; Sansone, C.; Albini, A.; Brunet, C. Microalgal Derivatives as Potential Nutraceutical and Food Supplements for Human Health: A Focus on Cancer Prevention and Interception. *Nutrients* **2019**, *11*, E1226, doi:10.3390/nu11061226.
20. Niehaus, T.D.; Okada, S.; Devarenne, T.P.; Watt, D.S.; Sviripa, V.; Chappell, J. Identification of Unique Mechanisms for Triterpene Biosynthesis in Botryococcus Braunii. *Proc. Natl. Acad. Sci. U. S. A.* **2011**, *108*, 12260–12265, doi:10.1073/pnas.1106222108.
21. Brown, A.C.; Knights, B.A.; Conway, E. Hydrocarbon Content and Its Relationship to Physiological State in the Green Alga Botryococcus Braunii. *Phytochemistry* **1969**, *8*, 543–547, doi:10.1016/S0031-9422(00)85397-2.
22. Chisti, Y. Biodiesel from Microalgae. *Biotechnol. Adv.* **2007**, *25*, 294–306, doi:10.1016/j.biotechadv.2007.02.001.
23. Eroglu, E.; Okada, S.; Melis, A. Hydrocarbon Productivities in Different Botryococcus Strains: Comparative Methods in Product Quantification. *J. Appl. Phycol.* **2011**, *23*, 763–775, doi:10.1007/s10811-010-9577-8.
24. van den Berg, T.E.; van Oort, B.; Croce, R. Light-Harvesting Complexes of Botryococcus Braunii. *Photosynth. Res.* **2018**, *135*, 191–201, doi:10.1007/s11120-017-0405-8.
25. Ranga Rao, A.; Sarada, R.; Ravishankar, G.A. Influence of CO2 on Growth and Hydrocarbon Production in Botryococcus Braunii. *J. Microbiol. Biotechnol.* **2007**, *17*, 414–419.
26. Dayananda, C.; Sarada, R.; Kumar, V.; Ravishankar, G.A. Isolation and Characterization of Hydrocarbon Producing Green Alga Botryococcus Braunii from Indian Freshwater Bodies. *Electron. J. Biotechnol.* **2007**, *10*, 78–91, doi:10.2225/vol10-issue1-fulltext-11.

27. Armstrong, G.A.; Hearst, J.E. Carotenoids 2: Genetics and Molecular Biology of Carotenoid Pigment Biosynthesis. *FASEB J. Off. Publ. Fed. Am. Soc. Exp. Biol.* **1996**, *10*, 228–237, doi:10.1096/fasebj.10.2.8641556.
28. Metzger, P.; Largeau, C. Botryococcus Braunii: A Rich Source for Hydrocarbons and Related Ether Lipids. *Appl. Microbiol. Biotechnol.* **2005**, *66*, 486–496, doi:10.1007/s00253-004-1779-z.
29. Dayananda, C.; Sarada, R.; Bhattacharya, S.; Ravishankar, G.A. Effect of Media and Culture Conditions on Growth and Hydrocarbon Production by Botryococcus Braunii. *Process Biochem.* **2005**, *40*, 3125–3131, doi:10.1016/j.procbio.2005.03.006.
30. Banerjee, A.; Sharma, R.; Chisti, Y.; Banerjee, U.C. Botryococcus Braunii: A Renewable Source of Hydrocarbons and Other Chemicals. *Crit. Rev. Biotechnol.* **2002**, *22*, 245–279, doi:10.1080/07388550290789513.
31. David, M.; Metzger, P.; Casadevall, E. Two Cyclobotryococcenes from the B Race of the Green Alga Botryococcus Braunii. *Phytochemistry* **1988**, *27*, 2863–2867, doi:10.1016/0031-9422(88)80677-0.
32. Metzger, P.; Allard, B.; Casadevall, E.; Berkaloff, C.; Coute, A. Structure and Chemistry of a New Chemical Race of Botryococcus Braunii (Chlorophyceae) That Produces Lycopadiene, a Tetraterpenoid Hydrocarbon. *J. Phycol.* **1990**, *26*, 258–266, doi:10.1111/j.0022-3646.1990.00258.x.
33. UTEX B 2441 Botryococcus Braunii.
34. Scott, S.A.; Davey, M.P.; Dennis, J.S.; Horst, I.; Howe, C.J.; Lea-Smith, D.J.; Smith, A.G. Biodiesel from Algae: Challenges and Prospects. *Curr. Opin. Biotechnol.* **2010**, *21*, 277–286, doi:10.1016/j.copbio.2010.03.005.
35. Thomas, W.H.; Tornabene, T.G.; Weissman, J. *Screening for Lipid Yielding Microalgae: Activities for 1983. Final Subcontract Report*; 1984; p. SERI/STR-231-2207, 6838870;
36. Amaro, H.M.; Guedes, A.C.; Malcata, F.X. Advances and Perspectives in Using Microalgae to Produce Biodiesel. *Appl. Energy* **2011**, *88*, 3402–3410, doi:10.1016/j.apenergy.2010.12.014.
37. Sforza, E.; Simionato, D.; Giacometti, G.M.; Bertucco, A.; Morosinotto, T. Adjusted Light and Dark Cycles Can Optimize Photosynthetic Efficiency in Algae Growing in Photobioreactors. *PloS One* **2012**, *7*, e38975, doi:10.1371/journal.pone.0038975.
38. Schenk, P.M.; Thomas-Hall, S.R.; Stephens, E.; Marx, U.C.; Mussgnug, J.H.; Posten, C.; Kruse, O.; Hankamer, B. Second Generation Biofuels: High-Efficiency Microalgae for Biodiesel Production. *BioEnergy Res.* **2008**, *1*, 20–43, doi:10.1007/s12155-008-9008-8.
39. Caffarri, S.; Tibiletti, T.; Jennings, R.; Santabarbara, S. A Comparison Between Plant Photosystem I and Photosystem II Architecture and Functioning. *Curr. Protein Pept. Sci.* **2014**, *15*, 296–331, doi:10.2174/1389203715666140327102218.
40. Raymond, J.; Blankenship, R.E. Horizontal Gene Transfer in Eukaryotic Algal Evolution. *Proc. Natl. Acad. Sci.* **2003**, *100*, 7419–7420, doi:10.1073/pnas.1533212100.

41. Raymond, J.; Blankenship, R.E. The Evolutionary Development of the Protein Complement of Photosystem 2. *Biochim. Biophys. Acta* **2004**, *1655*, 133–139, doi:10.1016/j.bbabio.2003.10.015.
42. Wu, F.; Yang, Z.; Su, X.; Gong, Y.; Kuang, T. Molecular Reorganization Induced by Ca2+ of Plant Photosystem I Reconstituted into Phosphatidylglycerol Liposomes. *Chem. Phys. Lipids* **2005**, *136*, 73–82, doi:10.1016/j.chemphyslip.2005.04.002.
43. Wollman, F.-A. State Transitions Reveal the Dynamics and Flexibility of the Photosynthetic Apparatus. *EMBO J.* **2001**, *20*, 3623–3630, doi:10.1093/emboj/20.14.3623.
44. Iwuchukwu, I.J.; Vaughn, M.; Myers, N.; O'Neill, H.; Frymier, P.; Bruce, B.D. Self-Organized Photosynthetic Nanoparticle for Cell-Free Hydrogen Production. *Nat. Nanotechnol.* **2010**, *5*, 73–79, doi:10.1038/nnano.2009.315.
45. Merchant, S.; Sawaya, M.R. The Light Reactions: A Guide to Recent Acquisitions for the Picture Gallery. *Plant Cell* **2005**, *17*, 648–663, doi:10.1105/tpc.105.030676.
46. Govindjee; Kern, J.F.; Messinger, J.; Whitmarsh, J. *Photosystem II*; 1st ed.; Wiley, 2001; ISBN 978-0-470-01617-6, doi: 10.1002/9780470015902.a0000669.pub2.
47. Grossman, A.R.; Bhaya, D.; Apt, K.E.; Kehoe, D.M. Light-Harvesting Complexes in Oxygenic Photosynthesis: Diversity, Control, and Evolution. *Annu. Rev. Genet.* **1995**, *29*, 231–288, doi:10.1146/annurev.ge.29.120195.001311.
48. Stirbet, A.; Govindjee, On the Relation between the Kautsky Effect (Chlorophyll a Fluorescence Induction) and Photosystem II: Basics and Applications of the OJIP Fluorescence Transient. *J. Photochem. Photobiol. B* **2011**, *104*, 236–257, doi:10.1016/j.jphotobiol.2010.12.010.
49. Stirbet, A.; Govindjee, Chlorophyll a Fluorescence Induction: A Personal Perspective of the Thermal Phase, the J-I-P Rise. *Photosynth. Res.* **2012**, *113*, 15–61, doi:10.1007/s11120-012-9754-5.
50. Shevela, D.; Do, H.-N.; Fantuzzi, A.; Rutherford, A.W.; Messinger, J. Bicarbonate-Mediated CO2 Formation on Both Sides of Photosystem II. *Biochemistry* **2020**, *59*, 2442–2449, doi:10.1021/acs.biochem.0c00208.
51. van Rensen, J.J.S. Role of Bicarbonate at the Acceptor Side of Photosystem II. *Photosynth. Res.* **2002**, *73*, 185–192, doi:10.1023/A:1020451114262.
52. Fromme, P.; Jordan, P.; Krauß, N. Structure of Photosystem I. *Biochim. Biophys. Acta BBA - Bioenerg.* **2001**, *1507*, 5–31, doi:10.1016/S0005-2728(01)00195-5.
53. Eberhard, S.; Finazzi, G.; Wollman, F.-A. The Dynamics of Photosynthesis. *Annu. Rev. Genet.* **2008**, *42*, 463–515, doi:10.1146/annurev.genet.42.110807.091452.
54. Baker, N.R. Chlorophyll Fluorescence: A Probe of Photosynthesis in Vivo. *Annu. Rev. Plant Biol.* **2008**, *59*, 89–113, doi:10.1146/annurev.arplant.59.032607.092759.
55. Drop, B.; Webber-Birungi, M.; Fusetti, F.; Kouřil, R.; Redding, K.E.; Boekema, E.J.; Croce, R. Photosystem I of Chlamydomonas Reinhardtii Contains Nine

Light-Harvesting Complexes (Lhca) Located on One Side of the Core. *J. Biol. Chem.* **2011**, *286*, 44878–44887, doi:10.1074/jbc.M111.301101.
56. Zhu, X.-G.; Long, S.P.; Ort, D.R. Improving Photosynthetic Efficiency for Greater Yield. *Annu. Rev. Plant Biol.* **2010**, *61*, 235–261, doi:10.1146/annurev-arplant-042809-112206.
57. Strasser, R.J.; Govindjee The Fo and the O-J-I-P Fluorescence Rise in Higher Plants and Algae. In *Regulation of Chloroplast Biogenesis*; Argyroudi-Akoyunoglou, J.H., Ed.; Springer US: Boston, MA, 1992; pp. 423–426 ISBN 978-1-4613-6485-6.
58. Pfannschmidt, T.; Yang, C. The Hidden Function of Photosynthesis: A Sensing System for Environmental Conditions That Regulates Plant Acclimation Responses. *Protoplasma* **2012**, *249 Suppl 2*, S125-136, doi:10.1007/s00709-012-0398-2.
59. Whatley, J.M.; Whatley, F.R. Chloroplast Evolution. *New Phytol.* **1981**, *87*, 233–247, doi:10.1111/j.1469-8137.1981.tb03195.x.
60. Marchand, J.; Heydarizadeh, P.; Schoefs, B.; Spetea, C. Ion and Metabolite Transport in the Chloroplast of Algae: Lessons from Land Plants. *Cell. Mol. Life Sci. CMLS* **2018**, *75*, 2153–2176, doi:10.1007/s00018-018-2793-0.
61. Pribil, M.; Labs, M.; Leister, D. Structure and Dynamics of Thylakoids in Land Plants. *J. Exp. Bot.* **2014**, *65*, 1955–1972, doi:10.1093/jxb/eru090.
62. Kirchhoff, H. Chloroplast Ultrastructure in Plants. *New Phytol.* **2019**, *223*, 565–574, doi:10.1111/nph.15730.
63. Rochaix, J.-D. The Dynamics of the Photosynthetic Apparatus in Algae. In *Applied Photosynthesis - New Progress*; Najafpour, M.M., Ed.; InTech, 2016 ISBN 978-953-51-2267-8.
64. Amorim, M.L.; Soares, J.; Coimbra, J.S.D.R.; Leite, M. de O.; Albino, L.F.T.; Martins, M.A. Microalgae Proteins: Production, Separation, Isolation, Quantification, and Application in Food and Feed. *Crit. Rev. Food Sci. Nutr.* **2021**, *61*, 1976–2002, doi:10.1080/10408398.2020.1768046.
65. Broser, M.; Gabdulkhakov, A.; Kern, J.; Guskov, A.; Müh, F.; Saenger, W.; Zouni, A. Crystal Structure of Monomeric Photosystem II from Thermosynechococcus Elongatus at 3.6-a Resolution. *J. Biol. Chem.* **2010**, *285*, 26255–26262, doi:10.1074/jbc.M110.127589.
66. Caffarri, S.; Kouril, R.; Kereïche, S.; Boekema, E.J.; Croce, R. Functional Architecture of Higher Plant Photosystem II Supercomplexes. *EMBO J.* **2009**, *28*, 3052–3063, doi:10.1038/emboj.2009.232.
67. Kashino, Y.; Lauber, W.M.; Carroll, J.A.; Wang, Q.; Whitmarsh, J.; Satoh, K.; Pakrasi, H.B. Proteomic Analysis of a Highly Active Photosystem II Preparation from the Cyanobacterium Synechocystis Sp. PCC 6803 Reveals the Presence of Novel Polypeptides. *Biochemistry* **2002**, *41*, 8004–8012, doi:10.1021/bi026012+.
68. Umena, Y.; Kawakami, K.; Shen, J.-R.; Kamiya, N. Crystal Structure of Oxygen-Evolving Photosystem II at a Resolution of 1.9 Å. *Nature* **2011**, *473*, 55–60, doi:10.1038/nature09913.
69. Ago, H.; Adachi, H.; Umena, Y.; Tashiro, T.; Kawakami, K.; Kamiya, N.; Tian, L.; Han, G.; Kuang, T.; Liu, Z.; et al. Novel Features of Eukaryotic Photosystem

II Revealed by Its Crystal Structure Analysis from a Red Alga. *J. Biol. Chem.* **2016**, *291*, 5676–5687, doi:10.1074/jbc.M115.711689.
70. Shi, L.-X.; Hall, M.; Funk, C.; Schröder, W.P. Photosystem II, a Growing Complex: Updates on Newly Discovered Components and Low Molecular Mass Proteins. *Biochim. Biophys. Acta BBA - Bioenerg.* **2012**, *1817*, 13–25, doi:10.1016/j.bbabio.2011.08.008.
71. Ozakca, D.U. Effect of Abiotic Stress on Photosystem I-Related Gene Transcription in Photosynthetic Organisms. In *Photosynthesis*; Dubinsky, Z., Ed.; InTech, 2013 ISBN 978-953-51-1161-0.
72. Bengis, C.; Nelson, N. Purification and Properties of the Photosystem I Reaction Center from Chloroplasts. *J. Biol. Chem.* **1975**, *250*, 2783–2788, doi:10.1016/S0021-9258(19)41558-5.
73. Toporik, H.; Khmelnitskiy, A.; Dobson, Z.; Riddle, R.; Williams, D.; Lin, S.; Jankowiak, R.; Mazor, Y. The Structure of a Red-Shifted Photosystem I Reveals a Red Site in the Core Antenna. *Nat. Commun.* **2020**, *11*, 5279, doi:10.1038/s41467-020-18884-w.
74. Lam, E.; Ortiz, W.; Malkin, R. Chlorophyll a/b Proteins of Photosystem I. *FEBS Lett.* **1984**, *168*, 10–14, doi:10.1016/0014-5793(84)80197-0.
75. Luimstra, V.M.; Schuurmans, J.M.; de Carvalho, C.F.M.; Matthijs, H.C.P.; Hellingwerf, K.J.; Huisman, J. Exploring the Low Photosynthetic Efficiency of Cyanobacteria in Blue Light Using a Mutant Lacking Phycobilisomes. *Photosynth. Res.* **2019**, *141*, 291–301, doi:10.1007/s11120-019-00630-z.
76. Tanaka, A.; Ito, H.; Tanaka, R.; Tanaka, N.K.; Yoshida, K.; Okada, K. Chlorophyll a Oxygenase (CAO) Is Involved in Chlorophyll b Formation from Chlorophyll a. *Proc. Natl. Acad. Sci. U. S. A.* **1998**, *95*, 12719–12723, doi:10.1073/pnas.95.21.12719.
77. Humphrey, A.M. Chlorophyll as a Color and Functional Ingredient. *J. Food Sci.* **2006**, *69*, C422–C425, doi:10.1111/j.1365-2621.2004.tb10710.x.
78. Filimon, R.V.; Rotaru, L.; Filimon, R.M. Quantitative Investigation of Leaf Photosynthetic Pigments during Annual Biological Cycle of Vitis Vinifera L. Table Grape Cultivars. *South Afr. J. Enol. Vitic.* **2016**, *37*, doi:10.21548/37-1-753.
79. Teramoto, H.; Ono, T.; Minagawa, J. Identification of Lhcb Gene Family Encoding the Light-Harvesting Chlorophyll-a/b Proteins of Photosystem II in Chlamydomonas Reinhardtii. *Plant Cell Physiol.* **2001**, *42*, 849–856, doi:10.1093/pcp/pce115.
80. Barera, S.; Pagliano, C.; Pape, T.; Saracco, G.; Barber, J. Characterization of PSII-LHCII Supercomplexes Isolated from Pea Thylakoid Membrane by One-Step Treatment with α- and β-Dodecyl-D-Maltoside. *Philos. Trans. R. Soc. Lond. B. Biol. Sci.* **2012**, *367*, 3389–3399, doi:10.1098/rstb.2012.0056.
81. Tikkanen, M.; Grieco, M.; Nurmi, M.; Rantala, M.; Suorsa, M.; Aro, E.-M. Regulation of the Photosynthetic Apparatus under Fluctuating Growth Light. *Philos. Trans. R. Soc. Lond. B. Biol. Sci.* **2012**, *367*, 3486–3493, doi:10.1098/rstb.2012.0067.

82. Das, K.; Roychoudhury, A. Reactive Oxygen Species (ROS) and Response of Antioxidants as ROS-Scavengers during Environmental Stress in Plants. *Front. Environ. Sci.* **2014**, *2*, doi:10.3389/fenvs.2014.00053.
83. Apel, K.; Hirt, H. Reactive Oxygen Species: Metabolism, Oxidative Stress, and Signal Transduction. *Annu. Rev. Plant Biol.* **2004**, *55*, 373–399, doi:10.1146/annurev.arplant.55.031903.141701.
84. Barati, B.; Gan, S.-Y.; Lim, P.-E.; Beardall, J.; Phang, S.-M. Green Algal Molecular Responses to Temperature Stress. *Acta Physiol. Plant.* **2019**, *41*, 26, doi:10.1007/s11738-019-2813-1.
85. Rezayian, M.; Niknam, V.; Ebrahimzadeh, H. Oxidative Damage and Antioxidative System in Algae. *Toxicol. Rep.* **2019**, *6*, 1309–1313, doi:10.1016/j.toxrep.2019.10.001.
86. Takagi, D.; Takumi, S.; Hashiguchi, M.; Sejima, T.; Miyake, C. Superoxide and Singlet Oxygen Produced within the Thylakoid Membranes Both Cause Photosystem I Photoinhibition. *Plant Physiol.* **2016**, *171*, 1626–1634, doi:10.1104/pp.16.00246.
87. Pospíšil, P. Production of Reactive Oxygen Species by Photosystem II as a Response to Light and Temperature Stress. *Front. Plant Sci.* **2016**, *7*, doi:10.3389/fpls.2016.01950.
88. Nelson, N.; Ben-Shem, A. The Structure of Photosystem I and Evolution of Photosynthesis. *BioEssays News Rev. Mol. Cell. Dev. Biol.* **2005**, *27*, 914–922, doi:10.1002/bies.20278.
89. Chen, Y.; Azad, M.B.; Gibson, S.B. Superoxide Is the Major Reactive Oxygen Species Regulating Autophagy. *Cell Death Differ.* **2009**, *16*, 1040–1052, doi:10.1038/cdd.2009.49.
90. Pérez-Pérez, M.E.; Lemaire, S.D.; Crespo, J.L. Reactive Oxygen Species and Autophagy in Plants and Algae. *Plant Physiol.* **2012**, *160*, 156–164, doi:10.1104/pp.112.199992.
91. Nishiyama, Y.; Allakhverdiev, S.I.; Murata, N. Protein Synthesis Is the Primary Target of Reactive Oxygen Species in the Photoinhibition of Photosystem II. *Physiol. Plant.* **2011**, *142*, 35–46, doi:10.1111/j.1399-3054.2011.01457.x.
92. Liu, J.; Lu, Y.; Hua, W.; Last, R.L. A New Light on Photosystem II Maintenance in Oxygenic Photosynthesis. *Front. Plant Sci.* **2019**, *10*, 975, doi:10.3389/fpls.2019.00975.
93. Allakhverdiev, S.I.; Kreslavski, V.V.; Fomina, I.R.; Los, D.A.; Klimov, V.V.; Mimuro, M.; Mohanty, P.; Carpentier, R. *Inactivation and Repair of Photosynthetic Machinery under Heat Stress*; First Edition.; IK International Publishing House: New Delhi, 2012; ISBN 978-93-81141-00-7.
94. Ugya, A.Y.; Imam, T.S.; Li, A.; Ma, J.; Hua, X. Antioxidant Response Mechanism of Freshwater Microalgae Species to Reactive Oxygen Species Production: A Mini Review. *Chem. Ecol.* **2020**, *36*, 174–193, doi:10.1080/02757540.2019.1688308.
95. Asada, K. Production and Scavenging of Reactive Oxygen Species in Chloroplasts and Their Functions. *Plant Physiol.* **2006**, *141*, 391–396, doi:10.1104/pp.106.082040.

96. Inupakutika, M.A.; Sengupta, S.; Devireddy, A.R.; Azad, R.K.; Mittler, R. The Evolution of Reactive Oxygen Species Metabolism. *J. Exp. Bot.* **2016**, *67*, 5933–5943, doi:10.1093/jxb/erw382.
97. Gamaley, I.A.; Klyubin, I.V. Roles of Reactive Oxygen Species: Signaling and Regulation of Cellular Functions. *Int. Rev. Cytol.* **1999**, *188*, 203–255, doi:10.1016/s0074-7696(08)61568-5.
98. Peleg, Z.; Walia, H.; Blumwald, E. Integrating Genomics and Genetics to Accelerate Development of Drought and Salinity Tolerant Crops. In *Plant Biotechnology and Agriculture*; Elsevier, 2012; pp. 271–286 ISBN 978-0-12-381466-1.
99. Paliwal, C.; Mitra, M.; Bhayani, K.; Bharadwaj, S.V.V.; Ghosh, T.; Dubey, S.; Mishra, S. Abiotic Stresses as Tools for Metabolites in Microalgae. *Bioresour. Technol.* **2017**, *244*, 1216–1226, doi:10.1016/j.biortech.2017.05.058.
100. Wagner, D.; Przybyla, D.; Op den Camp, R.; Kim, C.; Landgraf, F.; Lee, K.P.; Würsch, M.; Laloi, C.; Nater, M.; Hideg, E.; et al. The Genetic Basis of Singlet Oxygen-Induced Stress Responses of Arabidopsis Thaliana. *Science* **2004**, *306*, 1183–1185, doi:10.1126/science.1103178.
101. Aki, T.; Nara, A.; Uemura, K. Cytoplasmic Vacuolization during Exposure to Drugs and Other Substances. *Cell Biol. Toxicol.* **2012**, *28*, 125–131, doi:10.1007/s10565-012-9212-3.
102. Piszczek, E.; Gutman, W. Caspase-like Proteases and Their Role in Programmed Cell Death in Plants. *Acta Physiol. Plant.* **2007**, *29*, 391–398, doi:10.1007/s11738-007-0086-6.
103. Glick, D.; Barth, S.; Macleod, K.F. Autophagy: Cellular and Molecular Mechanisms. *J. Pathol.* **2010**, *221*, 3–12, doi:10.1002/path.2697.
104. Parzych, K.R.; Klionsky, D.J. An Overview of Autophagy: Morphology, Mechanism, and Regulation. *Antioxid. Redox Signal.* **2014**, *20*, 460–473, doi:10.1089/ars.2013.5371.
105. Mizushima, N.; Levine, B.; Cuervo, A.M.; Klionsky, D.J. Autophagy Fights Disease through Cellular Self-Digestion. *Nature* **2008**, *451*, 1069–1075, doi:10.1038/nature06639.
106. Yun, C.W.; Lee, S.H. The Roles of Autophagy in Cancer. *Int. J. Mol. Sci.* **2018**, *19*, E3466, doi:10.3390/ijms19113466.
107. Malty, R.H.; Jessulat, M.; Jin, K.; Musso, G.; Vlasblom, J.; Phanse, S.; Zhang, Z.; Babu, M. Mitochondrial Targets for Pharmacological Intervention in Human Disease. *J. Proteome Res.* **2015**, *14*, 5–21, doi:10.1021/pr500813f.
108. Claude-Taupin, A.; Fonderflick, L.; Gauthier, T.; Mansi, L.; Pallandre, J.-R.; Borg, C.; Perez, V.; Monnien, F.; Algros, M.-P.; Vigneron, M.; et al. ATG9A Is Overexpressed in Triple Negative Breast Cancer and Its in Vitro Extinction Leads to the Inhibition of Pro-Cancer Phenotypes. *Cells* **2018**, *7*, E248, doi:10.3390/cells7120248.
109. Liang, C.; Jung, J.U. Autophagy Genes as Tumor Suppressors. *Curr. Opin. Cell Biol.* **2010**, *22*, 226–233, doi:10.1016/j.ceb.2009.11.003.
110. Nagai, H.; Kim, Y.H. Cancer Prevention from the Perspective of Global Cancer Burden Patterns. *J. Thorac. Dis.* **2017**, *9*, 448–451, doi:10.21037/jtd.2017.02.75.

111. Hamurcu, Z.; Delibaşı, N.; Geçene, S.; Şener, E.F.; Dönmez-Altuntaş, H.; Özkul, Y.; Canatan, H.; Ozpolat, B. Targeting LC3 and Beclin-1 Autophagy Genes Suppresses Proliferation, Survival, Migration and Invasion by Inhibition of Cyclin-D1 and UPAR/Integrin B1/ Src Signaling in Triple Negative Breast Cancer Cells. *J. Cancer Res. Clin. Oncol.* **2018**, *144*, 415–430, doi:10.1007/s00432-017-2557-5.
112. Capparelli, C.; Chiavarina, B.; Whitaker-Menezes, D.; Pestell, T.G.; Pestell, R.G.; Hulit, J.; Andò, S.; Howell, A.; Martinez-Outschoorn, U.E.; Sotgia, F.; et al. CDK Inhibitors (P16/P19/P21) Induce Senescence and Autophagy in Cancer-Associated Fibroblasts, "Fueling" Tumor Growth via Paracrine Interactions, without an Increase in Neo-Angiogenesis. *Cell Cycle Georget. Tex* **2012**, *11*, 3599–3610, doi:10.4161/cc.21884.
113. Li, X.; Dong, Y.; Wang, W.; Wang, H.; Chen, Y.; Shi, G.; Yi, J.; Wang, J. Emodin as an Effective Agent in Targeting Cancer Stem-like Side Population Cells of Gallbladder Carcinoma. *Stem Cells Dev.* **2013**, *22*, 554–566, doi:10.1089/scd.2011.0709.
114. Hsu, S.-C.; Chung, J.-G. Anticancer Potential of Emodin. *BioMedicine* **2012**, *2*, 108–116, doi:10.1016/j.biomed.2012.03.003.
115. Conklin, K.A. Chemotherapy-Associated Oxidative Stress: Impact on Chemotherapeutic Effectiveness. *Integr. Cancer Ther.* **2004**, *3*, 294–300, doi:10.1177/1534735404270335.
116. Francies, F.Z.; Hull, R.; Khanyile, R.; Dlamini, Z. Breast Cancer in Low-Middle Income Countries: Abnormality in Splicing and Lack of Targeted Treatment Options. *Am. J. Cancer Res.* **2020**, *10*, 1568–1591.
117. Al-Thoubaity, F.K. Molecular Classification of Breast Cancer: A Retrospective Cohort Study. *Ann. Med. Surg. 2012* **2020**, *49*, 44–48, doi:10.1016/j.amsu.2019.11.021.
118. Guo, Y.; Pei, X. Tetrandrine-Induced Autophagy in MDA-MB-231 Triple-Negative Breast Cancer Cell through the Inhibition of PI3K/AKT/MTOR Signaling. *Evid.-Based Complement. Altern. Med. ECAM* **2019**, *2019*, 7517431, doi:10.1155/2019/7517431.
119. DeSantis, C.E.; Ma, J.; Gaudet, M.M.; Newman, L.A.; Miller, K.D.; Goding Sauer, A.; Jemal, A.; Siegel, R.L. Breast Cancer Statistics, 2019. *CA. Cancer J. Clin.* **2019**, *69*, 438–451, doi:10.3322/caac.21583.
120. Uscanga-Perales, G.I.; Santuario-Facio, S.K.; Sanchez-Dominguez, C.N.; Cardona-Huerta, S.; Muñoz-Maldonado, G.E.; Ruiz-Flores, P.; Barcenas-Walls, J.R.; Osuna-Rosales, L.E.; Rojas-Martinez, A.; Gonzalez-Guerrero, J.F.; et al. Genetic Alterations of Triple Negative Breast Cancer (TNBC) in Women from Northeastern Mexico. *Oncol. Lett.* **2019**, *17*, 3581–3588, doi:10.3892/ol.2019.9984.
121. Liu, Y.; Zhong, Y.; Tian, W.; Lan, F.; Kang, J.; Pang, H.; Hou, H.; Li, D. An Autophagy-Dependent Cell Death of MDA-MB-231 Cells Triggered by a Novel Rhein Derivative 4F. *Anticancer. Drugs* **2019**, *30*, 1038–1047, doi:10.1097/CAD.0000000000000820.

122. Kwapisz, D. Pembrolizumab and Atezolizumab in Triple-Negative Breast Cancer. *Cancer Immunol. Immunother. CII* **2021**, *70*, 607–617, doi:10.1007/s00262-020-02736-z.
123. Aryasomayajula, B.; Torchilin, V.P. Nanoformulations. In *Nanobiomaterials in Cancer Therapy*; Elsevier, 2016; pp. 307–330 ISBN 978-0-323-42863-7.
124. Fu, A.; Tang, R.; Hardie, J.; Farkas, M.E.; Rotello, V.M. Promises and Pitfalls of Intracellular Delivery of Proteins. *Bioconjug. Chem.* **2014**, *25*, 1602–1608, doi:10.1021/bc500320j.
125. Liu, X.; Wu, F.; Ji, Y.; Yin, L. Recent Advances in Anti-Cancer Protein/Peptide Delivery. *Bioconjug. Chem.* **2019**, *30*, 305–324, doi:10.1021/acs.bioconjchem.8b00750.
126. Lichtenthaler, H.K.; Buschmann, C. Chlorophylls and Carotenoids: Measurement and Characterization by UV-VIS Spectroscopy. *Curr. Protoc. Food Anal. Chem.* **2001**, *1*, F4.3.1-F4.3.8, doi:10.1002/0471142913.faf0403s01.
127. Meeks, J.C.; Castenholz, R.W. Growth and Photosynthesis in an Extreme Thermophile, Synechococcus Lividus (Cyanophyta). *Arch. F□r Mikrobiol.* **1971**, *78*, 25–41, doi:10.1007/BF00409086.
128. Lamb, J.J.; Røkke, G.; Hohmann-Marriott, M.F. Chlorophyll Fluorescence Emission Spectroscopy of Oxygenic Organisms at 77 K. *Photosynthetica* **2018**, *56*, 105–124, doi:10.1007/s11099-018-0791-y.
129. Yamaguchi, K.; Nakano, H.; Murakami, M.; Konosu, S.; Nakayama, O.; Kanda, M.; Nakamura, A.; Iwamoto, H. Lipid Composition of a Green Alga, Botryococcus Braunii. *Agric. Biol. Chem.* **1987**, *51*, 493–498, doi:10.1080/00021369.1987.10868040.
130. Molina, A.M.; Morales-Cruz, M.; Benítez, M.; Berríos, K.; Figueroa, C.M.; Griebenow, K. Redox-Sensitive Cross-Linking Enhances Albumin Nanoparticle Function as Delivery System for Photodynamic Cancer Therapy. *J. Nanomedicine Nanotechnol.* **2016**, *6*, 294, doi:10.4172/2157-7439.1000294.
131. Nelson, N.; Junge, W. Structure and Energy Transfer in Photosystems of Oxygenic Photosynthesis. *Annu. Rev. Biochem.* **2015**, *84*, 659–683, doi:10.1146/annurev-biochem-092914-041942.
132. Owens, T.G.; Webb, S.P.; Mets, L.; Alberte, R.S.; Fleming, G.R. Antenna Structure and Excitation Dynamics in Photosystem I. II. Studies with Mutants of Chlamydomonas Reinhardtii Lacking Photosystem II. *Biophys. J.* **1989**, *56*, 95–106, doi:10.1016/S0006-3495(89)82654-2.
133. Smith, B.M.; Morrissey, P.J.; Guenther, J.E.; Nemson, J.A.; Harrison, M.A.; Allen, J.F.; Melis, A. Response of the Photosynthetic Apparatus in Dunaliella Salina (Green Algae) to Irradiance Stress. *Plant Physiol.* **1990**, *93*, 1433–1440, doi:10.1104/pp.93.4.1433.
134. Jensen, P.E.; Bassi, R.; Boekema, E.J.; Dekker, J.P.; Jansson, S.; Leister, D.; Robinson, C.; Scheller, H.V. Structure, Function and Regulation of Plant Photosystem I. *Biochim. Biophys. Acta BBA - Bioenerg.* **2007**, *1767*, 335–352, doi:10.1016/j.bbabio.2007.03.004.
135. Kruip, J.; Bald, D.; Boekema, E.; Rögner, M. Evidence for the Existence of Trimeric and Monomeric Photosystem I Complexes in Thylakoid Membranes

from Cyanobacteria. *Photosynth. Res.* **1994**, *40*, 279–286, doi:10.1007/BF00034777.
136. Watanabe, M.; Kubota, H.; Wada, H.; Narikawa, R.; Ikeuchi, M. Novel Supercomplex Organization of Photosystem I in Anabaena and Cyanophora Paradoxa. *Plant Cell Physiol.* **2011**, *52*, 162–168, doi:10.1093/pcp/pcq183.
137. Scheller, H.V.; Jensen, P.E.; Haldrup, A.; Lunde, C.; Knoetzel, J. Role of Subunits in Eukaryotic Photosystem I. *Biochim. Biophys. Acta* **2001**, *1507*, 41–60, doi:10.1016/s0005-2728(01)00196-7.
138. Ben-Shem, A.; Nelson, N.; Frolow, F. Crystallization and Initial X-Ray Diffraction Studies of Higher Plant Photosystem I. *Acta Crystallogr. D Biol. Crystallogr.* **2003**, *59*, 1824–1827, doi:10.1107/s0907444903016056.
139. Largeau, C.; Casadevall, E.; Berkaloff, C.; Dhamelincourt, P. Sites of Accumulation and Composition of Hydrocarbons in Botryococcus Braunii. *Phytochemistry* **1980**, *19*, 1043–1051, doi:10.1016/0031-9422(80)83054-8.
140. Pagliano, C.; Barera, S.; Chimirri, F.; Saracco, G.; Barber, J. Comparison of the α and β Isomeric Forms of the Detergent N-Dodecyl-D-Maltoside for Solubilizing Photosynthetic Complexes from Pea Thylakoid Membranes. *Biochim. Biophys. Acta BBA - Bioenerg.* **2012**, *1817*, 1506–1515, doi:10.1016/j.bbabio.2011.11.001.
141. Danielsson, R.; Albertsson, P.-Å.; Mamedov, F.; Styring, S. Quantification of Photosystem I and II in Different Parts of the Thylakoid Membrane from Spinach. *Biochim. Biophys. Acta BBA - Bioenerg.* **2004**, *1608*, 53–61, doi:10.1016/j.bbabio.2003.10.005.
142. Kim, E.; Ahn, T.K.; Kumazaki, S. Changes in Antenna Sizes of Photosystems during State Transitions in Granal and Stroma-Exposed Thylakoid Membrane of Intact Chloroplasts in Arabidopsis Mesophyll Protoplasts. *Plant Cell Physiol.* **2015**, *56*, 759–768, doi:10.1093/pcp/pcv004.
143. Terai, H.; Watada, A.E.; Murphy, C.A.; Wergin, W.P. Scanning Electron Microscopic Study of Modified Chloroplasts in Senescing Broccoli Florets. *HortScience* **2000**, *35*, 99–103, doi:10.21273/HORTSCI.35.1.99.
144. Bassi, R.; Soen, S.Y.; Frank, G.; Zuber, H.; Rochaix, J.D. Characterization of Chlorophyll a/b Proteins of Photosystem I from Chlamydomonas Reinhardtii. *J. Biol. Chem.* **1992**, *267*, 25714–25721.
145. Itagaki, T.; Nakayama, K.; Okada, M. Chlorophyll-Protein Complexes Associated with Photosystem I Isolated from the Green Alga, Bryopsis Maxima. *Plant Cell Physiol.* **1986**, *27*, 1241–1247, doi:10.1093/oxfordjournals.pcp.a077221.
146. Lundell, D.J.; Glazer, A.N.; Melis, A.; Malkin, R. Characterization of a Cyanobacterial Photosystem I Complex. *J. Biol. Chem.* **1985**, *260*, 646–654.
147. Rajagopal, S.; Bukhov, N.; Carpentier, R. Changes in the Structure of Chlorophyll-Protein Complexes and Excitation Energy Transfer during Photoinhibitory Treatment of Isolated Photosystem I Submembrane Particles. *J. Photochem. Photobiol. B* **2002**, *67*, 194–200, doi:10.1016/s1011-1344(02)00326-3.
148. Krupnik, T.; Kotabová, E.; van Bezouwen, L.S.; Mazur, R.; Garstka, M.; Nixon, P.J.; Barber, J.; Kaňa, R.; Boekema, E.J.; Kargul, J. A Reaction Center-

Dependent Photoprotection Mechanism in a Highly Robust Photosystem II from an Extremophilic Red Alga, Cyanidioschyzon Merolae. *J. Biol. Chem.* **2013**, *288*, 23529–23542, doi:10.1074/jbc.M113.484659.

149. Yehezkeli, O.; Tel-Vered, R.; Wasserman, J.; Trifonov, A.; Michaeli, D.; Nechushtai, R.; Willner, I. Integrated Photosystem II-Based Photo-Bioelectrochemical Cells. *Nat. Commun.* **2012**, *3*, 742, doi:10.1038/ncomms1741.
150. Galka, P.; Santabarbara, S.; Khuong, T.T.H.; Degand, H.; Morsomme, P.; Jennings, R.C.; Boekema, E.J.; Caffarri, S. Functional Analyses of the Plant Photosystem I-Light-Harvesting Complex II Supercomplex Reveal That Light-Harvesting Complex II Loosely Bound to Photosystem II Is a Very Efficient Antenna for Photosystem I in State II. *Plant Cell* **2012**, *24*, 2963–2978, doi:10.1105/tpc.112.100339.
151. Wlodarczyk, L.M.; Snellenburg, J.J.; Ihalainen, J.A.; van Grondelle, R.; van Stokkum, I.H.M.; Dekker, J.P. Functional Rearrangement of the Light-Harvesting Antenna upon State Transitions in a Green Alga. *Biophys. J.* **2015**, *108*, 261–271, doi:10.1016/j.bpj.2014.11.3470.
152. Lamb, J.; Forfang, K.; Hohmann-Marriott, M. A Practical Solution for 77 K Fluorescence Measurements Based on LED Excitation and CCD Array Detector. *PloS One* **2015**, *10*, e0132258, doi:10.1371/journal.pone.0132258.
153. Croce, R.; Canino, G.; Ros, F.; Bassi, R. Chromophore Organization in the Higher-Plant Photosystem II Antenna Protein CP26. *Biochemistry* **2002**, *41*, 7334–7343, doi:10.1021/bi0257437.
154. Schlodder, E.; Shubin, V.V.; El-Mohsnawy, E.; Roegner, M.; Karapetyan, N.V. Steady-State and Transient Polarized Absorption Spectroscopy of Photosytem I Complexes from the Cyanobacteria Arthrospira Platensis and Thermosynechococcus Elongatus. *Biochim. Biophys. Acta BBA - Bioenerg.* **2007**, *1767*, 732–741, doi:10.1016/j.bbabio.2007.01.013.
155. Subramanyam, R.; Jolley, C.; Brune, D.C.; Fromme, P.; Webber, A.N. Characterization of a Novel Photosystem I-LHCI Supercomplex Isolated from Chlamydomonas Reinhardtii under Anaerobic (State II) Conditions. *FEBS Lett.* **2006**, *580*, 233–238, doi:10.1016/j.febslet.2005.12.003.
156. Bassi, R.; Simpson, D. Chlorophyll-Protein Complexes of Barley Photosystem I. *Eur. J. Biochem.* **1987**, *163*, 221–230, doi:10.1111/j.1432-1033.1987.tb10791.x.
157. Standfuss, J.; Kühlbrandt, W. The Three Isoforms of the Light-Harvesting Complex II: Spectroscopic Features, Trimer Formation, and Functional Roles. *J. Biol. Chem.* **2004**, *279*, 36884–36891, doi:10.1074/jbc.M402348200.
158. Le Quiniou, C.; van Oort, B.; Drop, B.; van Stokkum, I.H.M.; Croce, R. The High Efficiency of Photosystem I in the Green Alga Chlamydomonas Reinhardtii Is Maintained after the Antenna Size Is Substantially Increased by the Association of Light-Harvesting Complexes II. *J. Biol. Chem.* **2015**, *290*, 30587–30595, doi:10.1074/jbc.M115.687970.
159. Le Quiniou, C.; Tian, L.; Drop, B.; Wientjes, E.; van Stokkum, I.H.M.; van Oort, B.; Croce, R. PSI–LHCI of Chlamydomonas Reinhardtii : Increasing the

Absorption Cross Section without Losing Efficiency. *Biochim. Biophys. Acta BBA - Bioenerg.* **2015**, *1847*, 458–467, doi:10.1016/j.bbabio.2015.02.001.
160. Kirst, H.; Garcia-Cerdan, J.G.; Zurbriggen, A.; Ruehle, T.; Melis, A. Truncated Photosystem Chlorophyll Antenna Size in the Green Microalga Chlamydomonas Reinhardtii upon Deletion of the TLA3-CpSRP43 Gene. *Plant Physiol.* **2012**, *160*, 2251–2260, doi:10.1104/pp.112.206672.
161. Ozawa, S.-I.; Onishi, T.; Takahashi, Y. Identification and Characterization of an Assembly Intermediate Subcomplex of Photosystem I in the Green Alga Chlamydomonas Reinhardtii. *J. Biol. Chem.* **2010**, *285*, 20072–20079, doi:10.1074/jbc.M109.098954.
162. Rath, A.; Cunningham, F.; Deber, C.M. Acrylamide Concentration Determines the Direction and Magnitude of Helical Membrane Protein Gel Shifts. *Proc. Natl. Acad. Sci. U. S. A.* **2013**, *110*, 15668–15673, doi:10.1073/pnas.1311305110.
163. Croce, R.; Zucchelli, G.; Garlaschi, F.M.; Bassi, R.; Jennings, R.C. Excited State Equilibration in the Photosystem I−light-Harvesting I Complex: P700 Is Almost Isoenergetic with Its Antenna. *Biochemistry* **1996**, *35*, 8572–8579, doi:10.1021/bi960214m.
164. Kalaji, H.M.; Schansker, G.; Ladle, R.J.; Goltsev, V.; Bosa, K.; Allakhverdiev, S.I.; Brestic, M.; Bussotti, F.; Calatayud, A.; Dąbrowski, P.; et al. Frequently Asked Questions about in Vivo Chlorophyll Fluorescence: Practical Issues. *Photosynth. Res.* **2014**, *122*, 121–158, doi:10.1007/s11120-014-0024-6.
165. Wahba, H.A.; El-Hadaad, H.A. Current Approaches in Treatment of Triple-Negative Breast Cancer. *Cancer Biol. Med.* **2015**, *12*, 106–116, doi:10.7497/j.issn.2095-3941.2015.0030.
166. Cleator, S.; Heller, W.; Coombes, R.C. Triple-Negative Breast Cancer: Therapeutic Options. *Lancet Oncol.* **2007**, *8*, 235–244, doi:10.1016/S1470-2045(07)70074-8.
167. Chavez, K.J.; Garimella, S.V.; Lipkowitz, S. Triple Negative Breast Cancer Cell Lines: One Tool in the Search for Better Treatment of Triple Negative Breast Cancer. *Breast Dis.* **2010**, *32*, 35–48, doi:10.3233/BD-2010-0307.
168. Tjus, S.E.; Scheller, H.V.; Andersson, B.; Møller, B.L. Active Oxygen Produced during Selective Excitation of Photosystem I Is Damaging Not Only to Photosystem I, but Also to Photosystem II. *Plant Physiol.* **2001**, *125*, 2007–2015, doi:10.1104/pp.125.4.2007.
169. Lőrincz, P.; Juhász, G. Autophagosome-Lysosome Fusion. *J. Mol. Biol.* **2020**, *432*, 2462–2482, doi:10.1016/j.jmb.2019.10.028.
170. Pérez-Pérez, M.E.; Couso, I.; Crespo, J.L. Carotenoid Deficiency Triggers Autophagy in the Model Green Alga Chlamydomonas Reinhardtii. *Autophagy* **2012**, *8*, 376–388, doi:10.4161/auto.18864.
171. He, C.; Klionsky, D.J. Regulation Mechanisms and Signaling Pathways of Autophagy. *Annu. Rev. Genet.* **2009**, *43*, 67–93, doi:10.1146/annurev-genet-102808-114910.
172. Dielschneider, R.F.; Henson, E.S.; Gibson, S.B. Lysosomes as Oxidative Targets for Cancer Therapy. *Oxid. Med. Cell. Longev.* **2017**, *2017*, 3749157, doi:10.1155/2017/3749157.

173. Allakhverdiev, S.I.; Nishiyama, Y.; Takahashi, S.; Miyairi, S.; Suzuki, I.; Murata, N. Systematic Analysis of the Relation of Electron Transport and ATP Synthesis to the Photodamage and Repair of Photosystem II in Synechocystis. *Plant Physiol.* **2005**, *137*, 263–273, doi:10.1104/pp.104.054478.
174. Dragone, R.; Cheng, R.; Grasso, G.; Frazzoli, C. Diuron in Water: Functional Toxicity and Intracellular Detoxification Patterns of Active Concentrations Assayed in Tandem by a Yeast-Based Probe. *Int. J. Environ. Res. Public. Health* **2015**, *12*, 3731–3740, doi:10.3390/ijerph120403731.
175. Pansook, S.; Incharoensakdi, A.; Phunpruch, S. Effects of the Photosystem II Inhibitors CCCP and DCMU on Hydrogen Production by the Unicellular Halotolerant Cyanobacterium Aphanothece Halophytica. *ScientificWorldJournal* **2019**, *2019*, 1030236, doi:10.1155/2019/1030236.
176. Kodru, S.; Malavath, T.; Devadasu, E.; Nellaepalli, S.; Stirbet, A.; Subramanyam, R.; Govindjee, null The Slow S to M Rise of Chlorophyll a Fluorescence Reflects Transition from State 2 to State 1 in the Green Alga Chlamydomonas Reinhardtii. *Photosynth. Res.* **2015**, *125*, 219–231, doi:10.1007/s11120-015-0084-2.
177. Ridley, S.M. Interaction of Chloroplasts with Inhibitors: Induction of Chlorosis by Diuron during Prolonged Illumination in Vitro. *Plant Physiol.* **1977**, *59*, 724–732, doi:10.1104/pp.59.4.724.
178. Gall, A.; Berera, R.; Alexandre, M.T.A.; Pascal, A.A.; Bordes, L.; Mendes-Pinto, M.M.; Andrianambinintsoa, S.; Stoitchkova, K.V.; Marin, A.; Valkunas, L.; et al. Molecular Adaptation of Photoprotection: Triplet States in Light-Harvesting Proteins. *Biophys. J.* **2011**, *101*, 934–942, doi:10.1016/j.bpj.2011.05.057.
179. Herritt, M.T.; Pauli, D.; Mockler, T.C.; Thompson, A.L. Chlorophyll Fluorescence Imaging Captures Photochemical Efficiency of Grain Sorghum (Sorghum Bicolor) in a Field Setting. *Plant Methods* **2020**, *16*, 109, doi:10.1186/s13007-020-00650-0.
180. Tóth, S.Z.; Schansker, G.; Strasser, R.J. In Intact Leaves, the Maximum Fluorescence Level (F(M)) Is Independent of the Redox State of the Plastoquinone Pool: A DCMU-Inhibition Study. *Biochim. Biophys. Acta* **2005**, *1708*, 275–282, doi:10.1016/j.bbabio.2005.03.012.
181. Nishiyama, Y.; Allakhverdiev, S.I.; Murata, N. A New Paradigm for the Action of Reactive Oxygen Species in the Photoinhibition of Photosystem II. *Biochim. Biophys. Acta* **2006**, *1757*, 742–749, doi:10.1016/j.bbabio.2006.05.013.
182. Stamatakis, K.; Papageorgiou, G.C.; Govindjee, null Effects of Exogenous β-Carotene, a Chemical Scavenger of Singlet Oxygen, on the Millisecond Rise of Chlorophyll a Fluorescence of Cyanobacterium Synechococcus Sp. PCC 7942. *Photosynth. Res.* **2016**, *130*, 317–324, doi:10.1007/s11120-016-0255-9.
183. Kraljić, I.; Mohsni, S.E. A New Method for the Detection of Singlet Oxygen in Aqueous Solutions. *Photochem. Photobiol.* **1978**, *28*, 577–581, doi:10.1111/j.1751-1097.1978.tb06972.x.
184. Santra, S.; Kaittanis, C.; Perez, J.M. Cytochrome C Encapsulating Theranostic Nanoparticles: A Novel Bifunctional System for Targeted Delivery

of Therapeutic Membrane-Impermeable Proteins to Tumors and Imaging of Cancer Therapy. *Mol. Pharm.* **2010**, *7*, 1209–1222, doi:10.1021/mp100043h.
185. Zhang, Q.; Pi, J.; Woods, C.G.; Jarabek, A.M.; Clewell, H.J.; Andersen, M.E. Hormesis and Adaptive Cellular Control Systems. *Dose-Response Publ. Int. Hormesis Soc.* **2008**, *6*, 196–208, doi:10.2203/dose-response.07-028.Zhang.
186. Mattson, M.P. Hormesis Defined. *Ageing Res. Rev.* **2008**, *7*, 1–7, doi:10.1016/j.arr.2007.08.007.
187. Garbar, C.; Mascaux, C.; Giustiniani, J.; Merrouche, Y.; Bensussan, A. Chemotherapy Treatment Induces an Increase of Autophagy in the Luminal Breast Cancer Cell MCF7, but Not in the Triple-Negative MDA-MB231. *Sci. Rep.* **2017**, *7*, 7201, doi:10.1038/s41598-017-07489-x.
188. Yang, J.; Lee, S.J.; Kwon, Y.; Ma, L.; Kim, J. Tumor Suppressive Function of Matrin 3 in the Basal-like Breast Cancer. *Biol. Res.* **2020**, *53*, 42, doi:10.1186/s40659-020-00310-6.
189. Lugagne, J.-B.; Jain, S.; Ivanovitch, P.; Ben Meriem, Z.; Vulin, C.; Fracassi, C.; Batt, G.; Hersen, P. Identification of Individual Cells from Z-Stacks of Bright-Field Microscopy Images. *Sci. Rep.* **2018**, *8*, 11455, doi:10.1038/s41598-018-29647-5.
190. Kintzing, J.R.; Filsinger Interrante, M.V.; Cochran, J.R. Emerging Strategies for Developing Next-Generation Protein Therapeutics for Cancer Treatment. *Trends Pharmacol. Sci.* **2016**, *37*, 993–1008, doi:10.1016/j.tips.2016.10.005.
191. Cen, H.; Mao, F.; Aronchik, I.; Fuentes, R.J.; Firestone, G.L. DEVD-NucView488: A Novel Class of Enzyme Substrates for Real-Time Detection of Caspase-3 Activity in Live Cells. *FASEB J. Off. Publ. Fed. Am. Soc. Exp. Biol.* **2008**, *22*, 2243–2252, doi:10.1096/fj.07-099234.
192. Fink, S.L.; Cookson, B.T. Apoptosis, Pyroptosis, and Necrosis: Mechanistic Description of Dead and Dying Eukaryotic Cells. *Infect. Immun.* **2005**, *73*, 1907–1916, doi:10.1128/IAI.73.4.1907-1916.2005.
193. Caster, A.H.; Kahn, R.A. Computational Method for Calculating Fluorescence Intensities within Three-Dimensional Structures in Cells. *Cell. Logist.* **2012**, *2*, 176–188, doi:10.4161/cl.23150.
194. Wehbe, K.; Filik, J.; Frogley, M.D.; Cinque, G. The Effect of Optical Substrates on Micro-FTIR Analysis of Single Mammalian Cells. *Anal. Bioanal. Chem.* **2013**, *405*, 1311–1324, doi:10.1007/s00216-012-6521-6.
195. Escobar, Ma.L.; Echeverría, O.M.; Vázquez-Nin, G.H. Necrosis as Programmed Cell Death. In *Cell Death - Autophagy, Apoptosis and Necrosis*; Ntuli, T.M., Ed.; InTech, 2015 ISBN 978-953-51-2236-4.
196. Česen, M.H.; Repnik, U.; Turk, V.; Turk, B. Siramesine Triggers Cell Death through Destabilisation of Mitochondria, but Not Lysosomes. *Cell Death Dis.* **2013**, *4*, e818, doi:10.1038/cddis.2013.361.
197. Sivandzade, F.; Bhalerao, A.; Cucullo, L. Analysis of the Mitochondrial Membrane Potential Using the Cationic JC-1 Dye as a Sensitive Fluorescent Probe. *Bio-Protoc.* **2019**, *9*, e3128, doi:10.21769/BioProtoc.3128.
198. Azad, M.B.; Chen, Y.; Gibson, S.B. Regulation of Autophagy by Reactive Oxygen Species (ROS): Implications for Cancer Progression and Treatment. *Antioxid. Redox Signal.* **2009**, *11*, 777–790, doi:10.1089/ars.2008.2270.

199. Yoshii, S.R.; Mizushima, N. Monitoring and Measuring Autophagy. *Int. J. Mol. Sci.* **2017**, *18*, E1865, doi:10.3390/ijms18091865.